THE EFFECTS OF NITROGEN ION IMPLANTATION ON FATIGUE PROPERTIES OF PLAIN CARBON STEELS

A Thesis Submitted to the

College of Graduate and Postdoctoral Studies

In Partial Fulfillment of the Requirements

For the Degree of Master of Science

In the Department of Mechanical Engineering

University of Saskatchewan

Saskatoon

Canada

By

Emmanuel O. Awoyele

PERMISSION TO USE

In presenting this thesis in partial fulfillment of the requirements for a postgraduate degree from the University of Saskatchewan, I agree that the Libraries of this University may make it freely available for inspection. I further agree that permission for copying of this thesis in any manner, in whole or in part, for scholarly purposes may be granted by the professors who supervised my thesis work or, in their absence, by the College of Graduate and Postdoctoral Studies (CGPS), Head of the Department or the Dean of the College in which this thesis work was done. It is understood that any copying or publication or use of this thesis or parts thereof for financial gain shall not be allowed without my written permission. It is also understood that due recognition shall be given to me and to the University of Saskatchewan in any scholarly use which may be made of any material in my thesis.

Requests for permission to copy or to make other use of material in this thesis in whole or part should be addressed to:

Head of the Department of Mechanical Engineering
57 Campus Drive
University of Saskatchewan
Saskatoon, Saskatchewan
S7N 5A9 Canada

OR

Dean
College of Graduate and Postdoctoral Studies
University of Saskatchewan
116 Thorvaldson Building, 110 Science Place
Saskatoon, Saskatchewan
S7N 5C9 Canada

ABSTRACT

Plain carbon steels are widely used for simple structural applications and machinery parts because they are cheap and readily available, but they perform poorly under fatigue when compared with alloy steels. Plasma ion immersion implantation (PIII) is a surface modification technique which has shown to improve the hardness, corrosion, fatigue, and wear properties of steel. Most of the research works featuring this technique used nitrogen as the implantation species however, the materials used were mostly of alloy steels.

In the present study, AISI 1018 and AISI 1045 plain carbon steels were bombarded with nitrogen ions at a bias voltage of 5 kV and a working pressure of 15 mTorr for 1 h, 2 h, 3 h and 5 h. The effect of treatment conditions on implantation depth, hardness and phase evolution were analyzed using surface roughness measurements, microhardness and nanohardness tests, X-ray photoelectron spectroscopy and X-ray diffraction. The fatigue properties of nitrogen implanted steels were evaluated using a rotating bending fatigue test at 50 Hz, while fractured surfaces of failed samples were examined using scanning electron microscopy.

The surface roughness of AISI 1018 and AISI 1045 specimens remained practically unchanged after PIII treatment. It was also found that AISI 1045 steel had higher concentration of implanted nitrogen than AISI 1018 at the near surface. However, the implanted nitrogen atoms were distributed over a smaller depth from the surface in AISI 1045 compared with AISI 1018 steel. Both grades of steel showed an increase in microhardness after nitrogen implantation for all treatment times compare to their untreated counterparts. However, after 2 h of PIII treatment the hardness values measured remained virtually the same. Two distinct regions characterized the fatigue behavior of both grades of steel after nitrogen ion implantation, namely: the high cycle fracture domain (HCFD) and low cycle fracture domain (LCFD). The fatigue life of both steels was increased in the HCFD, while it decreased in the LCFD. This effect was more pronounced in AISI 1045 steel than AISI 1018 steel.

AKNOWLEDGMENTS

I would like to express my deepest gratitude to my supervisors, Professor Ike Oguocha and Professor Odeshi Akindele, for accepting me as their student and motivating me during my graduate program at the University of Saskatchewan. Special thanks to Professor Michael Bradley who spent his time, resources and gave useful feedback during the execution of this work. I will always be thankful for their support, patience, and advice.

I would like to appreciate my supervisory committee members, Professor Chris Zhang and Professor Duncan Cree, for their valuable advice. I would like to thank Mr. Zhao Nan Fang for his assistance and training during my studies.

I wish to thank Danielle Covelli and Dr. Ramaswami Sammynaiken for the XPS training at the Saskatchewan Structural Science Center (SSSC) and I am grateful to my colleagues Opeoluwa Fadele, Ahmed Tiamiyu, Masoud Mohammadtaheri and Chao Peng for their support and advice. Finally, I would like to thank my beloved wife, son, parents, and siblings for all their love and support.

May God bless them all.

TABLE OF CONTENTS

LIST OF TABLES

LIST OF FIGURES

LIST OF NOMENCLATURE

ABBREVIATIONS

AES	Atomic emission spectroscopy
AISI	American iron and steel institute
ASM	American society for metals
ASTM	American society for testing and materials
CII	Conventional ion implantation
EDS	Energy dispersive x-ray spectroscopy
GDS	Glow discharge spectroscopy
PIII	Plasma immersion ion implantation
PSII	Plasma source ion implantation
PVD	Physical vapor deposition
RBS	Rutherford backscattering spectroscopy
XPS	X-ray photoelectron spectroscopy
XRD	X-ray diffraction

SYMBOLS

λ_i	Ion free mean path (nm)
η_i	Ion density (mA/cm^2)
η_e	Electron density (cm^{-3})
T_e	Electron temperature (eV/kB)
$\emptyset$	Diameter (cm)
N	Number of cycles to failure
σ_a	Stress amplitude (MPa)
σ_e	Fatigue limit (MPa)
σ_{ts}	Tensile strength (MPa)

LIST OF COPYRIGHT PERMISSION

Copyright permissions obtained for figures used in this thesis are provided in Appendix A.

CHAPTER 1

INTRODUCTION

1.1 Overview

Most engineering design projects involve machine parts and structural components subjected to cyclic or fluctuating loads. This type of loading induces cyclic or fluctuating stresses leading to fatigue failure [1]–[4]. Fatigue is a dangerous form of failure because it occurs over time and at stress levels lower than the tensile strength of the material. The magnitude of the stress applied, and the quality of the component's surface are two main factors affecting its fatigue performance [5]. Due to economic, environmental and safety reasons, efforts have been made to extend the service life of engineered components. Solutions applied includes polishing to remove machining flaws; introducing compressive stresses into thin surface layer to compensate for some of the applied tensile stresses on loading; hardening the outer layer; and optimizing geometry (avoiding internal corners, notches etc.).

In recent times, research into surface treatments that can modify the surface properties of different ferrous materials without tampering with the functional properties of the bulk has been on the rise. Examples include nitriding, carburizing, surface hardening with arc lamps, laser and electron beam hardening, and ion implantation. Among the existing processes, ion implantation has attracted special attention due to its ability to operate at room temperatures [6]. There are no dimensional changes due to thermal distortions and no degradation of surface finish. Ion implantation is a process in which ions with very high energy are driven into a substrate. Ions of almost any atom species can be implanted, but nitrogen is widely used to improve corrosion resistance and tribological properties of steels and other alloys. Ion implantation can be carried out using the conventional ion implantation (CII) and plasma immersion ion implantation (PIII). In the conventional ion implantation process, ions are accelerated to high energy and are injected into a solid, whereas in plasma immersion ion implantation, specimens to be implanted are placed directly in a plasma source and then pulse biased to a high negative potential. A plasma sheath forms around the target and ions bombard the entire target. The advantages of PIII over CII

includes the ability to treat specimens with irregular shapes, process several samples at a time, and its low hardware cost.

Several studies using various surface treatment techniques have shown increased surface hardness and the introduction of compressive residual stress after treatment [7]–[10] Specifically, nitrogen ion implantation has been used to improve fatigue and wear properties of steel [7]–[9]. The improvement fatigue life of steel by nitrogen implantation depends on the characteristics of the implanted layer, in particular the hardness and residual stress distribution [10].

1.2 Motivation

Carbon steels, composed simply of iron and carbon, accounts for 90% of steel production [11], because of their attractive cost, wide availability, ease of fabrication and weldability. They possess material properties that are suitable for many structural and engineering applications; however, when it comes to exotic and highly demanding applications, alloy steels are preferred because of their improved mechanical properties. The ability to increase the surface hardness and introduce compressive residual stresses by nitrogen ion implantation could improve the fatigue life and other mechanical properties of carbon steels, making them more attractive for such engineering applications in place of alloy steels. Most of the research works involving steel surface treatments concentrated on alloy steels while only a few studies featured carbon steels. Also, amongst those conducted using carbon steels, the treatment process adopted involved high temperature processes. The effect of nitrogen implantation using PIII technique on the fatigue life of everyday steel such as AISI 1018 and AISI 1045, as well as the effect of carbon content on the penetration of implanted nitrogen ion would be a good addition to literature.

1.3 Objectives

The main goal of this study was to improve the fatigue properties of AISI 1018 and AISI 1045 steels by implanting nitrogen into the near surface using the PIII technique. To realize this goal, the following specific objectives were pursued:

1. Determine the effect of carbon content on implanted nitrogen ions distribution in plain carbon steels.

2. Evaluate the effect of nitrogen ion implantation on the hardness and fatigue properties of AISI 1018 and AISI 1045 steel.

1.4 Research Contributions

First, it was demonstrated that after a certain time of nitrogen implantation (two hours at -5 kV in this research), no significant change in hardness is observed with increasing implantation time. Secondly, it was shown that nitrogen ions of same average energy travel to different depths in plain carbon steels depending on their carbon content. The higher carbon content of AISI 1045 steel impeded the mean free path of implanted nitrogen ions. Finally, fatigue life improvement is dependent on the concentration of implanted nitrogen at the surface. No increase in fatigue limit was observed in AISI 1018 steel, whereas a 7% increase in fatigue limit was observed for AISI 1045 steel.

1.5 Thesis Outline

This thesis is organized as follows: Chapter 1 contains an overview of the research, its motivation, and objectives. A literature review of the properties of AISI 1018 and AISI 1045 steel, PIII treatment and its effect on fatigue are presented in Chapter 2. Chapter 3 discusses the materials used and experimental methods applied. In Chapter 4, experimental results were reported and discussed. Chapter 5 contains the conclusions deduced from the study and recommendations for future work.

CHAPTER 2

LITERATURE REVIEW

The properties of AISI 1018 steel, AISI 1045 steel and their applications are reviewed in this chapter. The fatigue behavior of metallic materials, plasma immersion ion implantation (PIII) for surface modification and the effect of nitrogen ion implantation on the fatigue behavior of steels are also reviewed.

2.1 AISI 1018 and AISI 1045 properties

Plain carbon steels are iron-carbon alloys in which the properties are primarily derived from the presence of carbon. Some elements such as manganese, silicon, sulfur, and phosphorus are present in small amounts due to the steel production method used. They are commercially categorized as low carbon, medium carbon and high carbon steel based on their carbon content. Low carbon steels have a carbon content ranging from 0.02 wt.% to 0.25 wt.%, medium carbon steel 0.25 wt.% – 0.55 wt.% and high carbon steel 0.55 wt.% – 1.5 wt.% [12].

AISI 1018 steel falls into the low carbon class having a carbon content of 0.18 wt.%. It is the most common grade of steel as it possesses material properties that are suitable for many structural applications. Its low carbon content gives it have sufficient plasticity for mechanical forming [13]. It has a lower tensile strength but a better ductility (i.e. ability to be drawn without fracture) than medium carbon steels. As more carbon is added to an iron-carbon alloy, it becomes harder and stronger, but less ductile [14]. AISI 1018 has a tensile strength of 440 MPa and an elastic modulus of about 190 GPa [15]. It has a hardness value of 140 HV (1000 gf) and a fatigue strength of 270 MPa [16] The common areas of its application include pressure vessels, heat exchangers, boilers, and other applications where a good balance of toughness, strength and ductility is required.

AISI 1045 is a medium carbon steel, mostly supplied in the black hot rolled condition and occasionally in the normalized condition. This steel has a higher strength but lower ductility than low carbon steel. Its ultimate tensile strength ranges between 570 and 700 MPa [17] with a yield strength of 330 MPa and an elastic (Young's) modulus of 190 GPa [18]. AISI 1045 steel has a

hardness value of 177 HV (1000 gf) and a fatigue strength of 320 MPa [18]. AISI 1045 is extensively used in applications requiring more strength and wear resistance than the AISI 1018 can provide. Typical applications include shafts, connecting rods, bolts, axles, hydraulic clamps etc.

2.2 Fatigue failure

Fatigue, in the context of material science, is the weakening of a material, precipitated by applying loads repeatedly. It is the continuous structural damage that happens, leading untimely to failure, when a material is subjected to cyclic loading. The presence of defects, residual stresses, fabrication joints in materials coupled with design flaws or unanticipated service loading/environments conditions can aggravate fatigue damage and makes it challenging to predict the fatigue life of a material. The mechanism of fatigue failure, fatigue testing method and various ways of improving fatigue life are discussed in this subsection.

2.2.1 Nature of fatigue

Fatigue failures initiate as microcracks, which propagate as fluctuating stress is applied until a critical size is attained by one of the cracks. A rapid failure of the part subsequently follows once the crack length exceeds the critical crack size for failure. Usually, the stress needed to start fatigue cracks in a material is less than that of its yield strength. In 1903, Ewing and Humphrey first described the sequence of deformation process when a specimen is subjected to cyclic stress as follows; (1) slip lines appear, (2) these slip lines broaden into more persistent slip bands as cyclic loading continues, and (3) cracks finally initiate in the persistent slip bands and propagate to failure. The number of slip bands was found to be higher at higher stress levels [19]. Stress-raisers such as holes, joints, bends etc., are also the locations for crack formation in addition to defects created by persistent slip bands [20], [21].

Fatigue data are generally presented as *S*-*N* curves, where the applied stress (*S*) is plotted against number of cycles to failure (*N*) on a log-log plot. As the applied stress decreases, the number of cycles to failure increases. Figure 2.1 shows the S-N curves of most metals [22].The actual *S*-*N*

line represents the mean of the data from several tests. Some materials, notably carbon steels, exhibit a flattening off at a particular stress level as seen in curve A of Figure 2.1 which is referred to as the fatigue limit. This flattening out is a characteristic of ferrous metals also called the endurance limit, below which an infinite number of loading cycles can be applied to a material without causing fatigue failure. The infinite-life region is the area below the lowest portion of the *S-N* curve. Specimens tested at stresses below the curve should run indefinitely. Nonferrous metals such as aluminum, magnesium, and copper alloys continue a downward trend and do not flatten out as seen in curve B of Figure 2.1. In such cases, a fatigue strength for a given number of cycles must be specified. An effective endurance limit for these materials is sometimes defined as the stress that causes failure at $1x10^8$ or $5x10^8$ loading cycles.

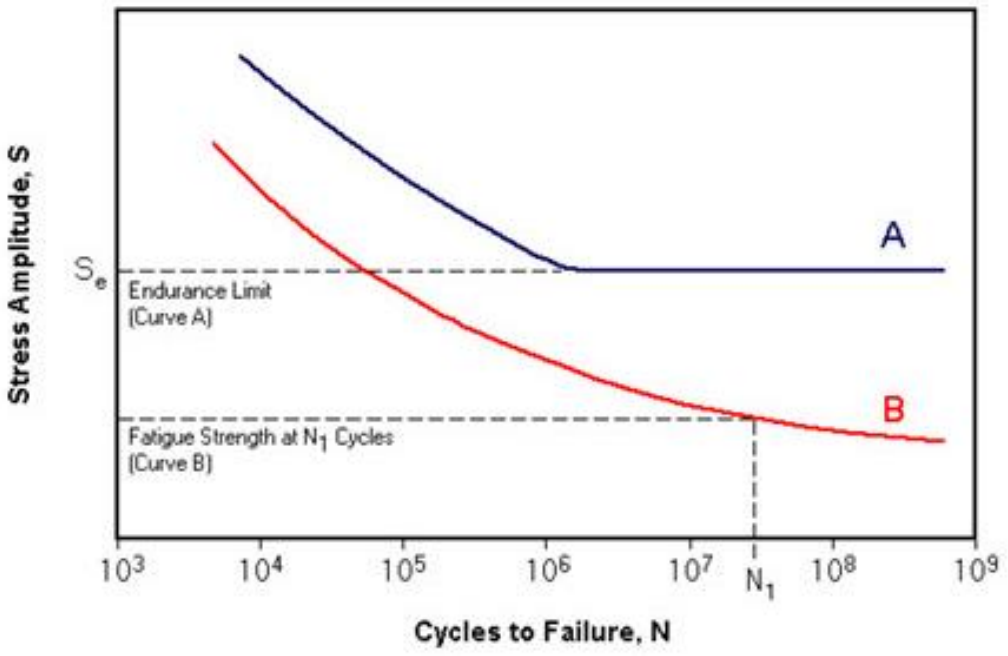

Figure 2.1. Typical S-N curves of metals [22].

Several factors affect the fatigue behavior of materials. These include material properties (tensile strength, hardness, ductility etc.); discontinuities i.e. planar flaws perpendicular to the direction of the stress such as undercut, cracks, and mismatch; microstructure; joint configuration; loading/service/environmental conditions; and the presence of residual stresses in the material.

The environment and service conditions affect the fatigue behavior of a component because corrosion and creep contribute to acceleration of fatigue failure. It has been reported that the damage due to corrosion fatigue can be greater than the sum of the damage by corrosion and fatigue acting separately [23]. Gough *et al.* [24] showed that the environment plays an active role in fatigue crack growth rate. In air, fatigue life is associated to a faster rate of crack growth resulting from oxygen adsorption at the tip of a crack compared to that in vacuum. Bradshaw *et al*. [25] found that crack rate in air was up to 60 times faster than that in vacuum. A large increase in the fatigue life of metals tested in vacuum than in air was also reported by Irving *et.al* [26].

Curthbertson [27] investigated the effect of temperature changes on the fatigue limit of medium carbon steel. He observed that the fatigue limit increased as the temperature was raised to about 90º C and thereafter began to decline rapidly such that at 120º C, the fatigue limit was less than that at room temperature.

Surface layer stress has a large influence on the fatigue behavior of metals. Kanchanomai *et al*. [28] found that with the introduction of compressive residual stress, the fatigue resistance of carbonitrided AISI 1015 steel was higher than that of AISI 1015 steel without carbonitriding. The fatigue limits of AISI 1015 steels with and without carbonitriding were 340 and 300 MPa, respectively. Cruz *et al.* [29] showed that subsurface crack initiation and the reduction of stress intensity factor were a direct consequence of the residual stresses at the surface of the specimen.

2.2.2 Fatigue testing

Fatigue investigations are usually conducted to develop a basic understanding of the fatigue behavior of materials; to extend empirical knowledge about the fatigue behavior of materials; and/or to obtain information on the fatigue response or behavior of a component or structure under service loadings. The specimens tested can range from small samples to complete assemblies, such as submarines and aircrafts weighing many tons [5]. Machines used for fatigue testing can be categorized based on the purpose of the test, the type of applied stress, operation characteristics and loading type [30]. Depending on the objective for which a fatigue test is conducted, various fatigue testing machines can be employed. A rotating cantilever bending machine applies non-

uniform bending moment along the length of the specimen. The bending moment applied to the test specimen varies linearly with the distance from the load application point. This arrangement is well suited for environmental type tests such as corrosion fatigue testing. A rotating bending machine, on the other hand, produces a uniform bending moment along the specimen length. This depicts what is involved in the railway axle fatigue problem. For a constant deflection amplitude cantilever bending machine, the load amplitude changes with specimen cyclic hardening or softening and decreases as cracks nucleate and grow [31]. An axial load test machine can apply both mean and alternating axial loads. It subjects test specimens to a uniform stress distribution over its cross section. This system is best for evaluating fatigue life in the plastic range. The influence of stress concentration is studied by machining holes, grooves, or notches in the specimen. Various standand practices related to fatigue testing are listed in Table 2.1.

Table 2.1. Standards related to metal fatigue testing.

Code	**Description**
ASTM E466	Conducting Force Controlled Constant Amplitude Axial Fatigue Tests of Metallic Materials.
ASTM E467	Verification of constant Amplitude Dynamic Forces in an Axial Fatigue Testing System.
ASTM E468	Presentation of Constant Amplitude Fatigue Test Results for Metallic Materials
ASTM E606	Strain-Controlled Fatigue Testing
ASTM E647	Measurement of Fatigue Crack Growth Rates
ASTM E739	Statistical Analysis of Linear or Linearized Stress-Life ($S-N$) and Strain-Life ($\varepsilon-N$) Fatigue Data
ASTM E1012	Verification of Specimen Alignment Under Tensile Loading
ASTM E1049	Cycle Counting in Fatigue Analysis
ASTM E1823	Standard Terminology Relating to Fatigue and Fracture Testing
ISO/DIS 12106	Metallic Materials-Fatigue Testing- Statistical Planning and Analysis of Data
ISO/DIS 12107	Metallic Materials-Fatigue Testing- Statistical Planning and Analysis of Data.
ISO/DIS 12108	Metallic Materials-Fatigue Testing- Fatigue Crack Growth Method

The accuracy of fatigue testing machines depends on individual care of calibration, and on the proper maintenance of the machine. Ikechukwu *et al.* [32] designed and tested a rotating beam fatigue testing machine. Their findings showed that fatigue failure cannot be predicted accurately since the it is affected by various factors such as the loading type, cycle per minute, temperature, atmospheric condition, and material defects. According to a survey of various conventional machines, Fink *et al.* [30] found that the accuracy of a test depends on three different factors, namely: (i) the design of the machine, (ii) the use of the machine (wear in bearings) and (iii) operation of the machine.

2.2.3 Estimating fatigue limit

The fatigue limit of a material can be estimated from its tensile strength and hardness values. Endurance ratio, which is the ratio of fatigue limit to tensile strength is used to predict the fatigue behavior of materials. This ratio is given in equations (2.1) and (2.2) for AISI 1018 and AISI 1045 respectively [33].

$$\sigma_w = 0.41\,\sigma_u \tag{2.1}$$

$$\sigma_w = 0.43\,\sigma_u \tag{2.2}$$

where 0.41 and 0.43 are the endurance ratios of AISI 1018 and AISI 1045, respectively, σ_w = fatigue limit and σ_u = ultimate tensile strength.

A correlation between fatigue limit and hardness in plain carbon steel is given in equation (2.3).

$$\sigma_w = 1.6HV \pm 0.1HV \tag{2.3}$$

where *HV* is the Vickers hardness in kgf/mm^2 and σ_w is in MPa.

Equation (2.3) is considered to be reliable when hardness is less than 400 HV, and no definite correlation could be found for hardness greater than 400 HV [34].

Murakami *et al.* [35] proposed a more detailed relationship between HV, fatigue strength and the square root of inclusion size or defect projection area $\sqrt{area}$ according to

$$\sigma_w = \frac{1.43\ (HV + 120)}{(\sqrt{(area)})^{1/6}} \tag{2.4}$$

Equation (2.4) is limited to fatigue fractures of small defect or non-metallic inclusion. In many real cases, however, there exist a fatigue limit for components not containing visible defects or cracks.

2.2.4 Improving fatigue life

Fatigue and wear resistance of steels can be improved using several techniques that involve the hardening of a component's surface without affecting the softer, tough interior. Parts such as a cam, shafts, bearings, and other components used in automobile and turbine applications require a very hard surface to resist mechanical damages, and a tough interior to resist the impact made during operation. Compressive residual stress is usually developed at the surface of a part after surface treatment. It reduces the probability of crack initiation and helps stop crack propagation at the case-core interface [36].

The main advantage of surface hardening over through hardening is that the distortion and crack problems usually associated with through hardening are minimized. According to Lampman [36], there are two broad approaches to classifying surface hardening methods:

1. Methods involving an intentional addition of a new layer as in the case of the use of thin films, coatings, and weld overlays. They generally become less cost-effective as production quantities increase. Fatigue performance here primarily depends on the bond strength between the substrate and the added layer.
2. Methods where surface and subsurface layers are modified without layer build-ups or an increase in dimension which is sub-divided into diffusion and selective hardening methods. For diffusion methods, hardening species such as carbon, nitrogen etc., are used to alter the chemical composition of the entire surface of a part. The basic process used is thermochemical because some heat is needed to enhance the diffusion of hardening elements into the surface and subsurface regions of the part. Nitriding and carburizing

techniques fall under this group and are best used when many parts are to be surface hardened. On the other hand, selective hardening methods pick localized areas to effect a transformational change (from heating and quenching) or compositional modification. Some techniques included in this groups are flame hardening, induction hardening, laser hardening, ion implantation and selective nitriding.

2.3 Plasma immersion ion implantation

Plasma immersion ion implantation (PIII) process has a vast application in materials engineering and semiconductor device fabrication. A brief history, the basic mechanism of a PIII technique and main components of a PIII system are presented in this section.

2.3.1 History of PIII

The first ion implanter was a helium-based implanter, constructed and operated in 1911 at Cavendish Laboratory in Cambridge by Ernest Rutherford and his students [3]. Initially, ion implantation technology was developed to dope semiconductor materials [37]. Later in the mid-seventies, this technology was used to modify the surface properties of metals [38]. Wear and corrosion resistance were reported to be enhanced after implantation of nitrogen or carbon ion into steel. The conventional ion implantation (CII) technique is a line-of-sight technique where ions are accelerated to high energy and are injected into a target. To achieve uniform implantation, the target must be manipulated which adds lots of complexity to the system. In a bid to solve this problem, a new technique was developed in the early 1980s, at Mission Research Corporation by Adler *et.al*. [39]. They successfully implanted carbon and titanium ions uniformly based on short-pulse vacuum arcs with negative high voltage pulses. Not long after, Conrad and Castagna [40] came up with a 3-D ion implantation equipment which they named plasma source ion implantation (PSII) otherwise known as plasma immersion ion implantation (PIII). Consequently, numerous research work has been conducted to help in understanding the physics and the optimization of process parameters pertaining to the PIII technique. As of today, research interest has been generated in many laboratories around the world on PIII because of its various tribological applications. This technique has been useful in modifying the chemical and physical characteristics

of various material surfaces, yielding high strength, lightweight, and corrosion resistant components, at a low cost.

2.3.2 Basic mechanism of PIII

Plasma is a state of matter in which ionized gaseous substances move randomly so that there is average charge neutrality. It is highly conductive, and its behavior is dominated by electrical and magnetic fields. A schematic diagram of the PIII system is shown in Figure 2.2. Its main components consist of a vacuum chamber, a transformer, gas supply, voltage pulse modulator and a target holder.

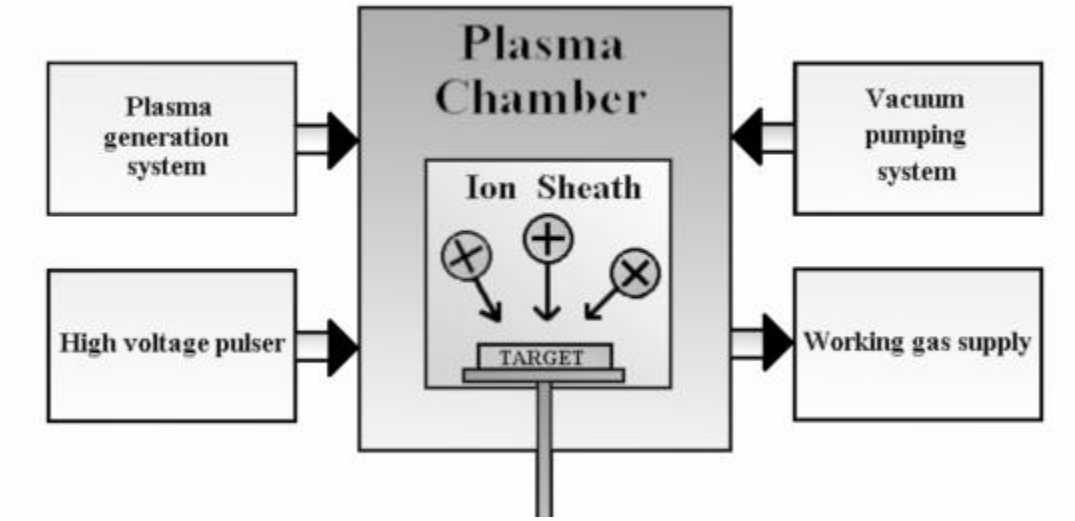

Figure 2.2. Plasma immersion ion implantation [41].

The pulse generator delivers a negative bias to the target. The vacuum pump generates the vacuum needed to generate plasma in the chamber. Other accessories like a Langmuir probe used to measure plasma density and electron temperature, an ionization gauge to measure neutral density during implantation, and a pyrometer to monitor target temperature during implantation can be added to the system.

To implant ions in this system, the target, which is to be treated, is firmly attached to the target holder. The target holder is isolated and properly insulated from the vacuum chamber. Plasma is then generated in the chamber and the generated pulsed negative bias is applied to the target. To describe how the ions from the plasma are implanted under steady state conditions, it is assumed

that a plasma consists of electrons, ions, neutral atoms and molecules, confined between two grounded absorbing walls as shown in Figure 2.3 (a). Since the densities of positive ions and negative ions (electrons) are equal ($\eta_i = \eta_e$), the net charge density will be zero. The electric potential and field will also be zero. Now, because the electron temperature is larger than that of ion temperature, and electrons are lighter than ions, the electron thermal velocity becomes so much more than the ion thermal velocity (approximately 100 times more) [42]–[44]. As a result, the highly mobile electrons are lost to the grounded chamber walls, leaving positively charged ions at the edge of the chamber (Figure 2.3.b). Therefore, there is a varying potential profile – positive within the plasma and zero at the wall. This non-neutral region between the chamber wall and plasma is called a sheath [45], [46]. At the boundary of plasma and sheath dynamics, it is required that the mean ion velocity at the plasma-sheath edge be equal to Bohm (ion-sound) velocity, $u_B = (eT_e/M)^{1/2}$ where e and M are the charge and mass of ion, respectively and T_e is the electron temperature in volts [47].

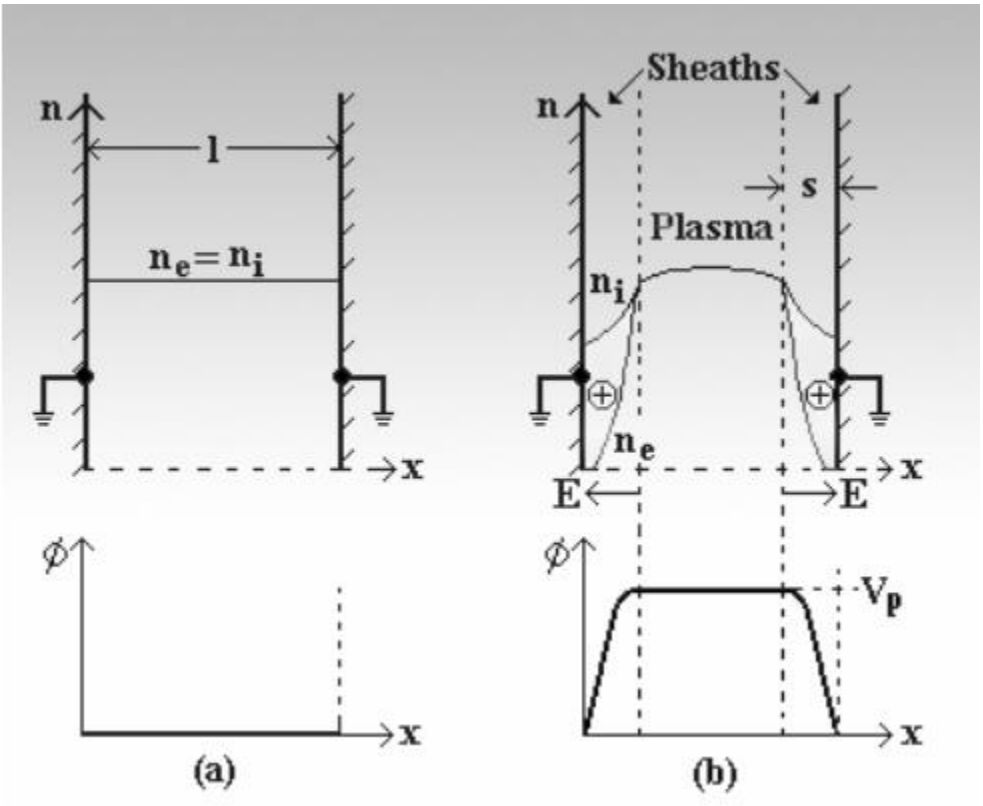

Figure 2.3. Plasma sheath formation under steady state: (a) initial charge densities and potential (b) charge densities, electric field, and potential variation after sheath formation [41].

Since the PIII process is pulsed, the transient characteristics of sheaths are given due consideration. (Figure 2.4 a) illustrates a planar target to be implanted immersed in a uniform plasma, it is assumed that a high-voltage negative pulse with an instantaneous rise-time of pulse voltage at time = 0 is applied to the target. In a few nanoseconds, the electrons with lighter mass are driven away at a time scale of inverse electron frequency $\omega_{pe}{}^{-1} = (\varepsilon_0 m_e / n_e e^2)^{1/2}$. This results in a sheath of uniform ion density developed around the substrate (Figure 2.4b). Thereafter, the heavier ions within the sheath, on a time scale of a few microseconds of the order of inverse ion plasma frequency, $\omega_{pe}{}^{-1} = (\varepsilon_0 m_e / n_e e^2)^{1/2}$, are accelerated by the electric field developed and are driven into the surface of the substrate.

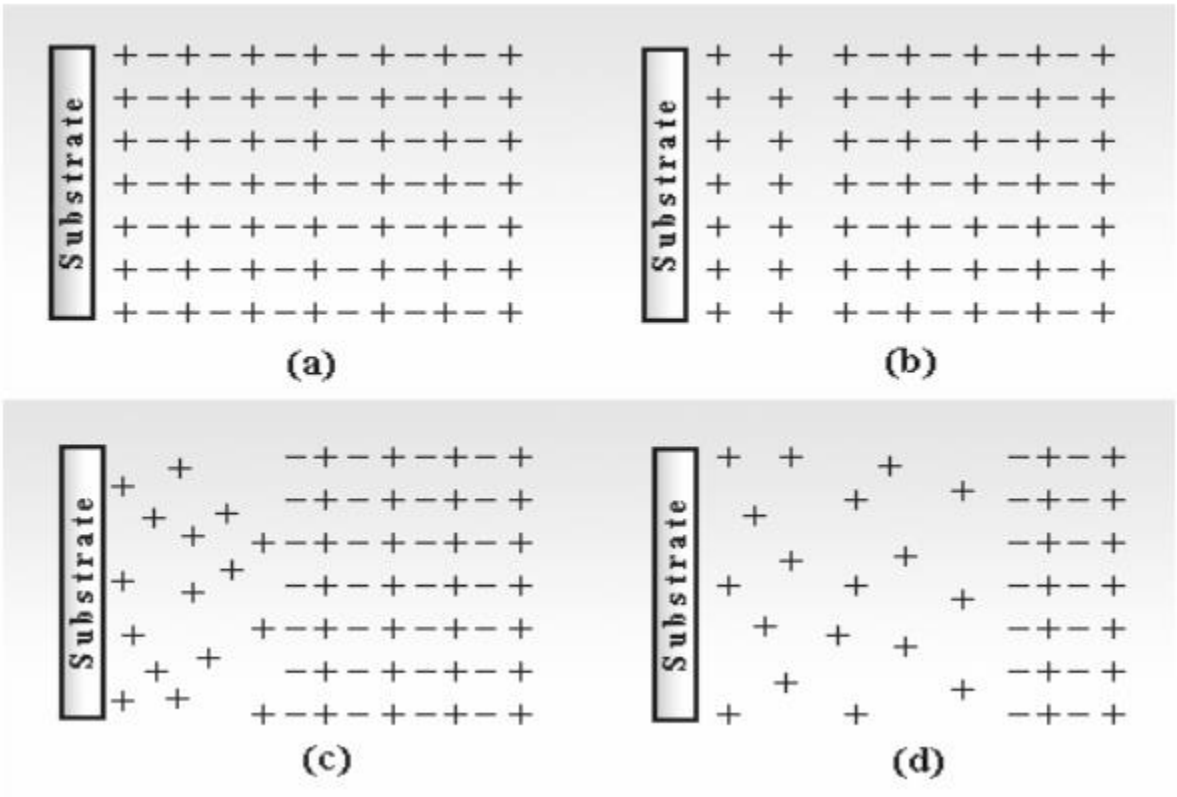

Figure 2.4. Time evolution of plasma sheath during PIII pulse: (a) uniform plasma (b) ion-matrix sheath (c) expanding sheath (d) expanded sheath [41]. Ions and electrons are represented by + and –, respectively.

As the ions are implanted, charge imbalance drifts more electrons away from the substrate, thereby uncovering more ions from the plasma, resulting in an expansion in sheath thickness (Figure 2.4c) After several microseconds, a steady-state ion current flow governed by Child-Langmuir equation [40] is established across the sheath as shown in Figure 2.4d. To successfully implant an ion species into a substrate, some specifications must be met:

1. The size of plasma must be by far larger than the sheath thickness to avoid total depletion of plasma ions between target and the plasma wall.
2. The mean ion penetration depth is determined by the energy distribution function of the ions being implanted. To control this, it is important to control the ion charge state, sheath voltage and pulse shape. It is best approximated when the ion mean free path (λ_i) is greater than sheath thickness [48].
3. For multi-species plasma, different ions get implanted to distinct projected depths, because of their different velocities. Therefore, it as desirable to control the velocity distribution function at the target's surface. Low pressure plasma would be helpful in utilizing the total capacity of the voltage pulse supplier [41].
4. Finally, the denser the plasma, the shorter the sheath thickness and hence, larger ion density. This may result in arching and cause increased substrate heating [49], [50].

When ions enter a solid, they lose energy through elastic collisions and through electron excitations. In the beginning of the slowing-down process at high energies, the ion is slowed down mainly by electronic stopping, and it moves almost in a straight path. When the ion has slowed down sufficiently, the collisions with nuclei (the nuclear stopping) become more and more probable, finally dominating the slowing down. When atoms of the target receive significant recoil energies when struck by the ion, they will be removed from their lattice positions, and produce a cascade of further collisions in the material. These collision cascades are the main cause of damage production during ion implantation in metals and semiconductors. When the energies of all atoms in the system have fallen below the threshold displacement energy, the production of new damage ceases, and the concept of nuclear stopping is no longer meaningful.

During the implantation process, a quasi-steady state redistribution of nitrogen into four main locations occur. They include: (i) edge dislocations traps, (ii) vacancy traps, (iii) octahedral

interstices and (iv) heterophases. Nitrogen atoms will be trapped in the positive dilatation region of an edge dislocation, where the lattice parameter is slightly larger than ideal. A damage cascade will form vacant lattice sites and iron interstitials which are mobile at the implantation temperature [51]. These vacancies trap many nitrogen interstitials. Nitrogen will also populate the octahedral sites of the bcc lattice randomly during implantation.

The plasma immersion ion implantation (PIII) technique has several advantages over conventional ion implantation (CII) and other forms of surface modification processes. Ions get implanted onto the target surface on all sides (Figure 2.5), thus eliminating the complicated and sophisticated mechanisms of CII; proving to be a comparatively simple and cost competitive technique. Its advantages are:

i. The system is relatively easy to operate and maintain
ii. It is economical; running cost is substantially less
iii. Process time does not depend on the size or surface area of the sample – it consumes less time for larger targets.
iv. Any geometry, size and weight of target can be processed.
v. The system can easily be set up for other processes such as deposition, etching etc., and different materials (semiconductors, metals, insulating materials) can be treated.
vi. Batch processing is possible with this system, yielding high throughput.
vii. It is a low temperature process, so the dimensional accuracy is maintained after treatment.
viii. A variety of species with multiple charges can be implanted at same time.

Despite its numerous advantages, PIII technique has some drawbacks:

i. It is not possible to separate species in the chamber, the chances of implanting undesired ions (impurities) is almost inevitable
ii. Secondary electrons generated limit the efficiency and generates x-rays
iii. The energy distribution of implanted ions is inhomogeneous
iv. It is also quite challenging to monitor in situ dose.

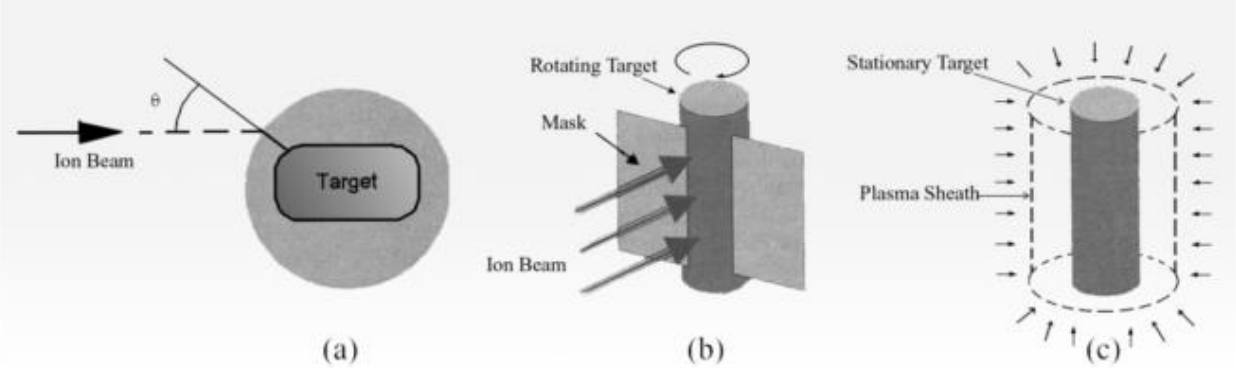

Figure 2.5. Retained dose issues for conventional ion implantation vs. PIII [41].

2.4 Nitriding, plasma nitriding and nitrogen ion implantation.

Nitriding is a heat treatment process of enriching the surface of a steel with diffused nitrogen at a temperature, normally in the range of 500-575 °C to create a case-hardened surface. Diffusion of nitrogen species into metallic surface is based on the mechanism of thermal diffusion or plasma-activated thermal diffusion. There are two main effects of the nitrogen diffusion process. One the one hand, it induces the formation of a superficial layer containing hard metal nitrides which gives a high hardness and toughness at the surface. Plain carbon steels do not contain any strong nitride forming elements, therefore, when nitrided, form a shallow overlayer of iron nitrides (ε-$Fe_{2,3}N$, γ-Fe_4N, typically), denoted as white layer. The iron nitride case thus formed is generally brittle which can induce catastrophic crack propagation into the bulk component under normal or shear overloading. It is usually recommended to remove such films by mechanical means (sand blasting, polishing). Alloy steels contain strong nitride forming elements such as Al, Mo, Cr, Ti, V etc which interact with nitrogen during nitriding to form nitrides precipitates such as AlN, TiN, VN, CrN Mo_2N etc. This results to a higher surface hardness. On the other hand, it produces a diffusion layer in which nitrogen atoms occupy interstitial sites in the crystalline lattice of the host material, producing an induced lattice expansion effect. This lattice expansion causes compressive stresses, which improve the toughness, wear, and fatigue resistance.

Thermal diffusion processes include gas nitriding and salt bath nitriding. They typically require a temperature above 500 °C and the use of reactive nitriding precursors such as pure N_2 or NH_3. Additionally, processing times could be of the order of 1-2 days to achieve a diffusion layer

thickness of some hundreds of microns. Nitriding in molten salts at high temperatures (700-800 °C) is still widely utilized in various industrial sectors.

Plasma-activated thermal diffusion processes include plasma nitriding, cathodic arc-activated nitriding, and triode plasma nitriding. Here, the reactivity of the nitriding media is not due to the temperature but to the gas ionized state. Plasma nitriding is carried out in a low-pressure nitrogen containing atmosphere (1 -10 mbar). Intense electric fields are used to generate ionized molecules of the gas at elevated temperature (450-550 °C). Components to be nitrided are connected to a cathode and the chamber itself serves as anode. Upon applying a potential difference above a critical value between the cathode and the anode, N_2 dissociates to ions and radicals. The ions move to the surface of the cathode, react with the free electron cloud at the surface and are converted into nascent nitrogen atom, they then get adsorbed and then diffuse inside. The temperature of the specimen is maintained by ion bombardment and sometimes by external heating. The diffusivity of nitrogen, which is an interstitial solid solution forming element, is orders of magnitude faster than that of the alloying elements, which are substitutional solid solution forming elements. Thus, the extent of alloy nitride precipitation is controlled by the diffusion of nitrogen and the precipitate size is controlled essentially by the diffusion of the alloying elements. Plasma nitriding is often coupled with physical vapor deposition (PVD) process and labeled duplex treatment, with enhanced benefits.

Plasma immersion ion implantation is different from plasma nitriding in several ways. First, in PIII, plasma is generated with the help of various plasma sources (e.g. electron cyclotron resonance plasma source, inductively coupled radio frequency plasma generator etc.) prior to the application of negatively biased pulses while in plasma nitriding, plasma is generated when there is an electric field between the anode and the cathode. When opposing electrical charge is applied to the wall of the chamber and the component to be implanted, the gas within the chamber dissociates and forms plasma. Furthermore, in PIII, nitrogen ions are accelerated as a projectile to the surface and implanted into the specimens due to the application of a high voltage pulse while in plasma nitriding, nitrogen ions in the plasma formed move to the surface of the specimen, gets adsorbed and diffuses into the specimen. PIII is considered a room temperature process. It is usually performed at temperatures < 400 °C [52] with little or no diffusion of nitrogen after implantation.

2.5 The effect of various surface treatments involving nitrogen atoms on hardness and fatigue properties of metals

Hutchings *et al.* [53] have shown that under suitable conditions, nitrogen ion implantation reduces the wear rate of Ti-6Al-4V by over two orders of magnitude. With increasing doses of implanted nitrogen ions, there was an increase in hardness up to a dose of 1 x 10^{21} ions m^{-2}, after which there was no significant change in hardness.

Celik *et al*. [54] investigated the influence of plasma nitriding on the fatigue strength of AISI 1040 low-alloy steel under varying process conditions of temperature (500- 600 ^{o}C), time (1-12 h), and heat treatment (quenched and tempered, normalized). A rotating beam bending machine was used to determine fatigue strength. They found a significant improvement (up to 35%) in fatigue strength. The fatigue limit was dependent on the surface hardness of the case layer. He also observed that the surface hardness of the treated layer decreased as the treatment temperature increased and that the depth of the treated layer increased with increasing temperature and time.
Yoshihiro *et al*. examined the depth profile of nitrogen implanted in cold-rolled plain steel sheet (steel, plate, cold, commercial -SPCC). It was found that the peak concentration of implanted nitrogen was 25 at. % and the peak concentration of implanted nitrogen did not depend on ion dose. Depth profile results obtained from glow discharge spectroscopy (GDS), Auger electron microscopy (AES), Rutherford backscattering spectroscopy (RBD), X-ray photoelectron spectroscopy (XPS) and X-ray diffraction (XRD) were all similar [55].

The effects of high-temperature plasma immersion ion implantation (PIII) of nitrogen in AISI H13 steel was studied by Da Silva *et al*. [56]. PIII treatments were performed at varying temperatures ranging from 300 ˚C to 720 ˚C. Implantation voltage of 5 kV was applied for 3 h. As the process temperature increased, the penetration depth of implanted nitrogen also increased. However, the concentration of nitrogen at the surface decreased as the PIII treatment temperature increased; this was a result of higher sputtering in the sample surface at higher treatment temperatures. A maximum hardness of about 592 HV was obtained for the specimen treated at 470 °C. This was 17% higher than the untreated specimen. Although an enriched nitrogen layer was obtained, no

evidence of nitride compounds was detected by XRD analyses. There was a decrease of the hardness values for temperatures above 470 °C. There was a significant change in the surface morphology between the sample PIII treated at 300 ˚C and that treated at 720 ˚C After treatment at 720 ˚C, a ball-like structure forming small agglomerates was observed by SEM examination. Samples treated at lower temperatures did not show this feature. The agglomerates formed was due to the coalescence of precipitates in H13 steel when subjected to high-temperature PIII treatment, which is associated with the formation of iron carbide (Fe_3C). This coalescence of precipitates produced a reduction in hardness as observed from micro and nanoindentation results. There was no evidence of white layer (iron nitride precipitation). On the surface, a slight decrease of elastic modulus was observed with increasing process temperature.

Obrtlik *et al*. [57] investigated the effect of carbonitriding by PIII on the fatigue behavior of 316L austenitic stainless steel. It was observed that at low stress amplitudes, most cracks originated below the surface resulting in prolonged life. At high stress amplitudes, main cracks originated at the surface and the fatigue life of the treated steel was reduced when compared to the untreated steel. Liu *et al.* [58] studied the fatigue life and mechanical behavior of AISI52100 bearing steel after nitrogen implantation. From their results, it was evident that the higher the substrate bias voltage, the larger the depth of nitrogen implantation and as the implantation depth increased so did the microhardness. Improvement in mechanical properties and fatigue was attributed to the solid solution of nitrogen atoms and the compressive residual stress created.

It was of interest to investigate the effect of nitrogen implantation on the fatigue life of common everyday steel such as AISI 1018 and AISI 1045 as well as the effect of carbon content on the penetration of implanted nitrogen ion. Furthermore, the relationship between PIII treatment time (concentration of implanted nitrogen) and hardness of AISI 1018 and AISI 1045 would be a good addition to literature.

CHAPTER 3

MATERIALS AND EXPERIMENTAL METHODS

This chapter presents and discusses the experimental materials used and procedures followed to achieve the research objectives stated in Chapter 1.

3.1 Materials

AISI 1018 and AISI 1045 rods were obtained from Gambit Corporation Precision Metal Forming as cold drawn rods. Their chemical compositions are shown in Table 3.1.

Table 3.1. Elemental composition of AISI 1018 and AISI 1045 carbon steels [15].

	Element (wt.%)				
Material	C	Mn	S	P	Fe
AISI 1018	0.14 – 0.20	0.60 – 0.90	0.050	0.040	Balance
AISI 1045	0.42 – 0.50	0.60 – 0.90	0.050	0.040	Balance

3.2 Test specimens

Two types of specimens were used in this research: short rods and fatigue test specimens. Ten short cylindrical rods of both AISI 1018 and AISI 1045 steels (see Figure 3.1) were prepared by the Faculty of Engineering Machine Shop. They were subsequently cut into 3 mm thick disc coupons using a Buehler Isomet precision cutter. These samples were used for surface roughness, microhardness, nanohardness, XPS and XRD tests. Samples were cold mounted for polishing using acrylic resin. The cold-mounted samples were pre-ground using 320 (46 µm), 500 (30 µm) and 1200 (15 µm) SiC grit emery papers and finally, fine ground using 2000 (10 µm) and 4000 (5 µm) SiC grit emery papers. Forty-five fatigue specimens each of AISI 1018 and AISI 1045 grade steels were produced in accordance with ASTM Standard E466. Figure 3.2 shows a part drawing of a typical fatigue specimen.

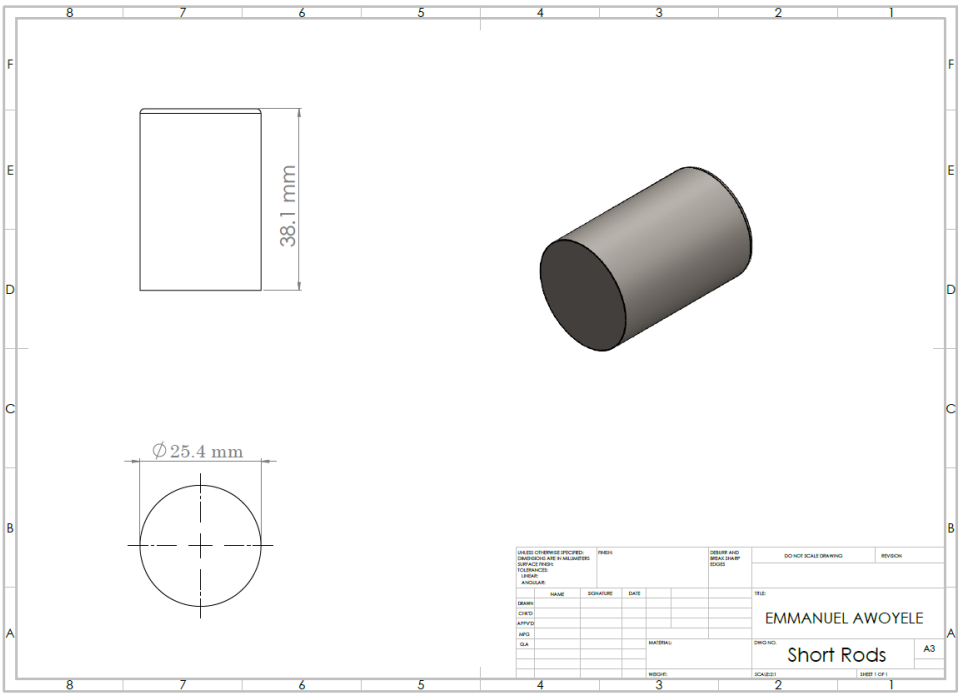

Figure 3.1. Drawing of a typical short rod produced by the Engineering Machine Shop.

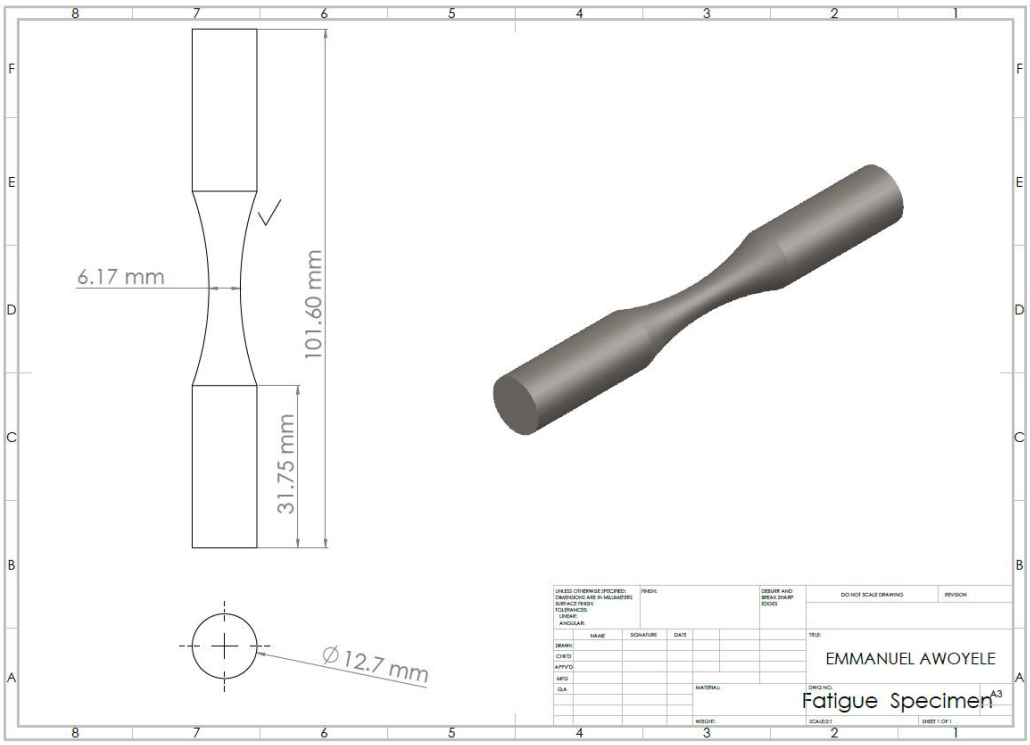

Figure 3.2. Drawing of a typical fatigue specimen used in the present study.

3.3 ICPII machine

The inductively coupled plasma ion implantation (ICPII) machine used for ion implantation experiment during this research can be found at the Plasma Physics Laboratory (PPL) of the Department of Physics and Engineering Physics. It had not been used for some years, so it had to be reactivated and calibrated before being used for my experiment. The key aspects of the reactivation process are described in subsections below.

3.3.1 **Westinghouse pulse transformer**

The Westinghouse pulse transformer is a step-up pulse transformer which is used between the pulse generator and the plasma chamber to transform the voltage produced by the pulse generator to a higher output (see Figure 3.4). This transformer increases the input by a factor of 10. The pulses produced by the pulse generator are of short duration, ~15 microseconds, and is roughly rectangular in shape. The purpose of using this transformer over others was to get the pulse wave shape supplied to the chamber as close as possible to that supplied by the pulse generator. There were distortions in the pulse wave generated by this transformer. A filter system (see Figure 3.3) of a diode D_{series} and resistor R_{shunt} between the transformer and the chamber was introduced to dampen voltage overshoots resulting from impedance mismatching and to stop the large back-flush of plasma electrons.

The steps taken to restore the transformer are as follow:

i. Removed the cover of the transformer container
ii. Syphoned the oil.
iii. Took off 8 bolts holding the transformer in place. To achieve this, the transformer was stood on one side and a pry bar was used to support it on the other end.
iv. Removed all debris and cleaned the transformer.
v. Performed various circuit tests, and repaired faults as instructed by the manual.
vi. Reinstalled the transformer into its container.
vii. Replaced the old transformer oil (Shell Diala Oil AX) with a fresh one.
viii. Tested the transformer
ix. Installed the tank cover and tested the transformer again.

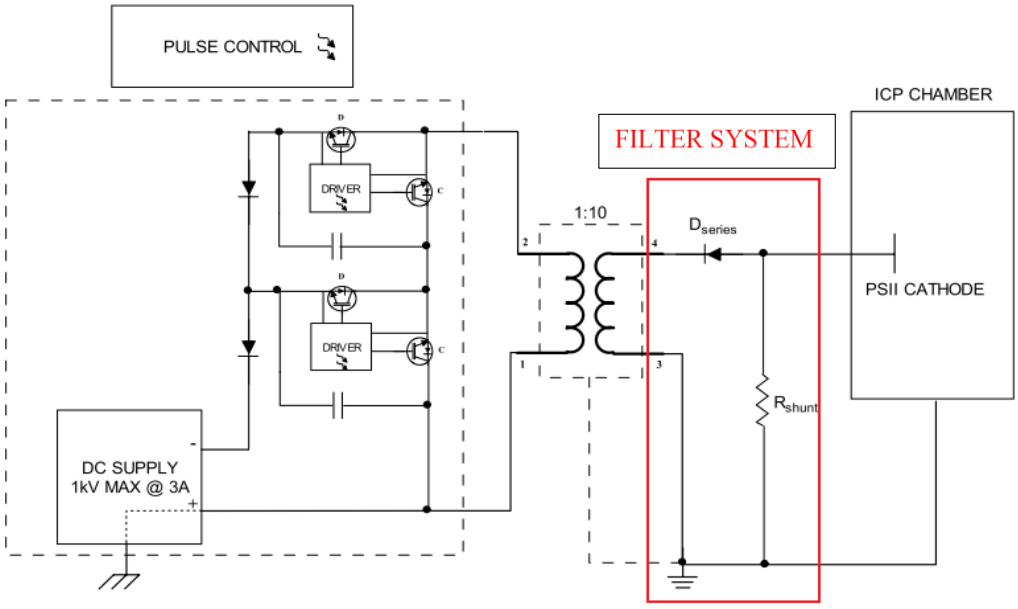

Figure 3.3. PIII modulator schematic highlighting the filter system.

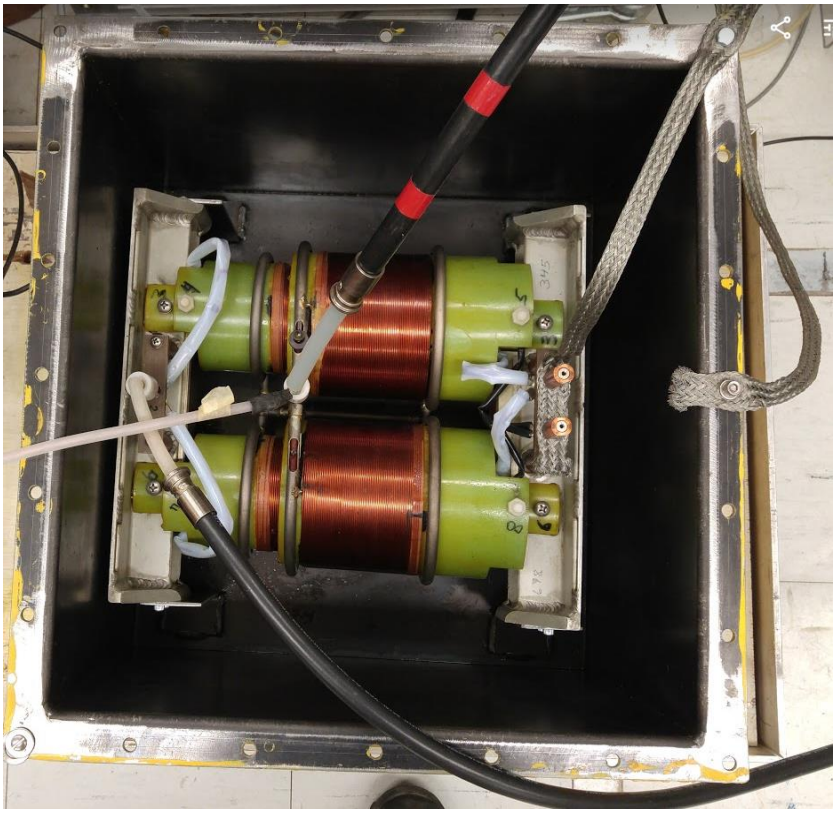

Figure 3.4. A Westinghouse pulse transformer.

3.3.2 **Pulse generator**

The next phase of work done was to reactivate the pulse modulator. Its function is to generate a fast, tightly regulated pulsed power to the plasma ion implantation chamber. To achieve this, a high voltage switch that can operate at short pulse width, fast rise and fall times, and high pulse repetition rates was required. The switch used in this work was a solid-state modulator. It is more effective and reliable than older switches such as the gridded vacuum tubes, thyrathrons, and pulse forming networks (PFNs).

An ideal pulse power circuit for plasma immersion ion implantation (PIII) application is shown in Figure 3.5. It is powered by an ideal voltage source giving a constant voltage and an unlimited current. It also carries an ideal switch with the following characteristics: (i) it has an infinitesimal switching time, (ii) it operates as both an opening and closing switch and (iii) it has approximately zero series impedance when closed and infinite impedance when open.

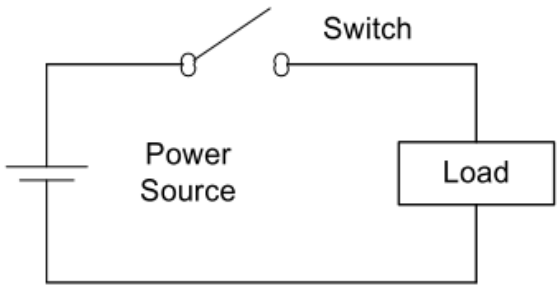

Figure 3.5. Power circuit supplying an ideal pulse for PIII applications.

The plasma accelerating voltage of the circuit in Figure 3.5 will be a perfect square pulse. The voltage pulse will have a minimal rise and fall time and a flat top, independent of load, current and repetition rate. Figure 3.6 illustrates an ideal pulse. Practically, there are factors that prevent having this perfect PIII pulse shape. Factors such as a variable DC power supply with finite current capability, series impedance inherent in any circuit and the cable capacitance between the power source and the plasma add distortions to the pulse wave. The objective here is to minimize the effects of these factors on the pulse. Solid state modulators feature configurations of insulated gate

bipolar transistor (IGBT) switches in series and parallel allowing high voltages and currents. They operate as opening and closing switches, providing extensive flexibility in pulse-width and very fast fault protection. A stack of solid-state modulators is shown in Figure 3.7. After several tests, it was found that only one of these Marx stages was serviceable. The pulse height is given by

$$V = V_{DC} \times (number\ of\ stages) \times (ratio) \tag{3.1}$$

where V_{DC} is the voltage output of the custom-built DC supply (having a maximum of 1.2 kV), and ratio is the step-up ratio of the transformer.

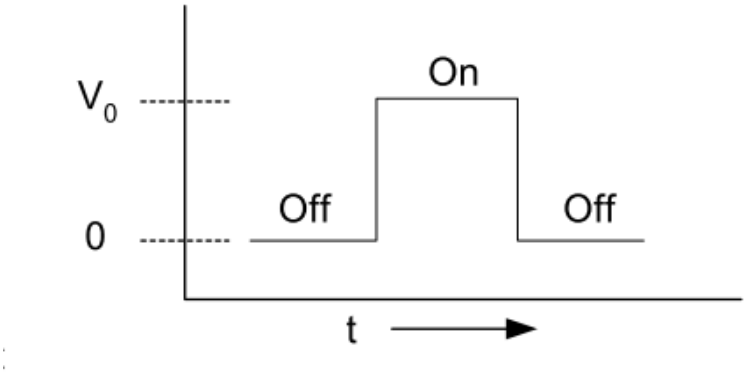

Figure 3.6. An ideal pulse for PIII application.

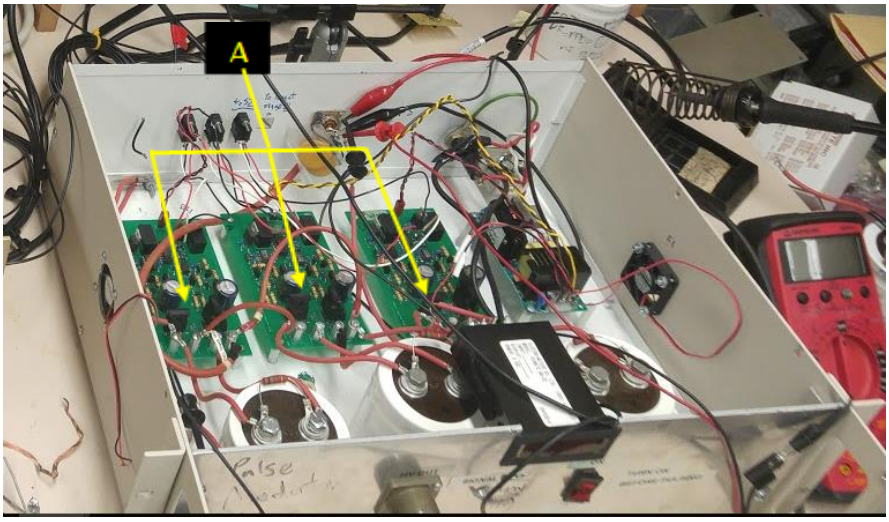

Figure 3.7. The solid-state modulator configuration used for the pulser control. Parts labeled A are insulated gate bipolar transistor (IGBT) switches.

This modulator also contains pull down resistors, storage capacitors, controls and protection circuitry required to provide 12 kV, 90 A pulses, at arbitrary pulse-widths from 1 μs to 1 ms. For high voltage implantation, one could utilize either a directly-coupled power supply and modulator or a lower voltage modulator with a pulse transformer. The later set-up was used in the present research. The major advantage of this approach is reduced cost.

3.3.3 **Turbo and roughing pumps**

The plasma chamber is evacuated by a Leybold-Hereaus Trivac D8A roughing pump which brings the pressure down to about 20 mTorr in few minutes. The lubrication fluid of the pump was changed, and the dirt trap was cleaned following the instructions in its manual. As part of the setup procedure for a PIII process, it is very important to evacuate the chamber to roughing vacuum before turning on the turbo pump to remove bulk gas that could damage the fins of the turbo pump. A Leybold turbo-molecular pump model He-500 was used to further reduce the pressure in the chamber to ~10^{-7} Torr which takes about 12 h. High vacuum prevents contamination due to implantation of unwanted ions.

3.3.4 **Specimen holder**

The ICPII machine in the Department of Physics and Engineering Physics was originally set up for semiconductor applications. As such, a new specimen holder suitable for batch processing of many metallic specimens was designed and produced.

When a high pulse voltage is applied to a specimen immersed in plasma, a plasma sheath forms around the specimen and expands. A minimum space between specimens must be kept such that this plasma sheath does not expand sufficiently during the time of applied pulse voltage to contact either the chamber walls or the sheath around adjacent specimens. This provides spatial and implantation depth uniformity.

The final ion-matrix sheath thickness is determined by the plasma density, specimen radius of curvature, applied implantation potential, plasma electron temperature and the ion mass [40]. For implantation of nitrogen ions into a cylindrical specimen of Ø1.27 cm (fatigue samples) at a

potential of 5 kV, the initial ion-matrix sheath formed at a radius of 3.18 cm from the central axis of the target cylinder, and the sheath expanded to a final radius of 5.70 cm using an ion acoustic velocity of 0.25 cmms^{-1} and pulse width of 10 µs. The part drawing used to produce the specimen holder is shown in Figure 3.8. The calculations made to get the final sheath radius are shown in Appendix C.

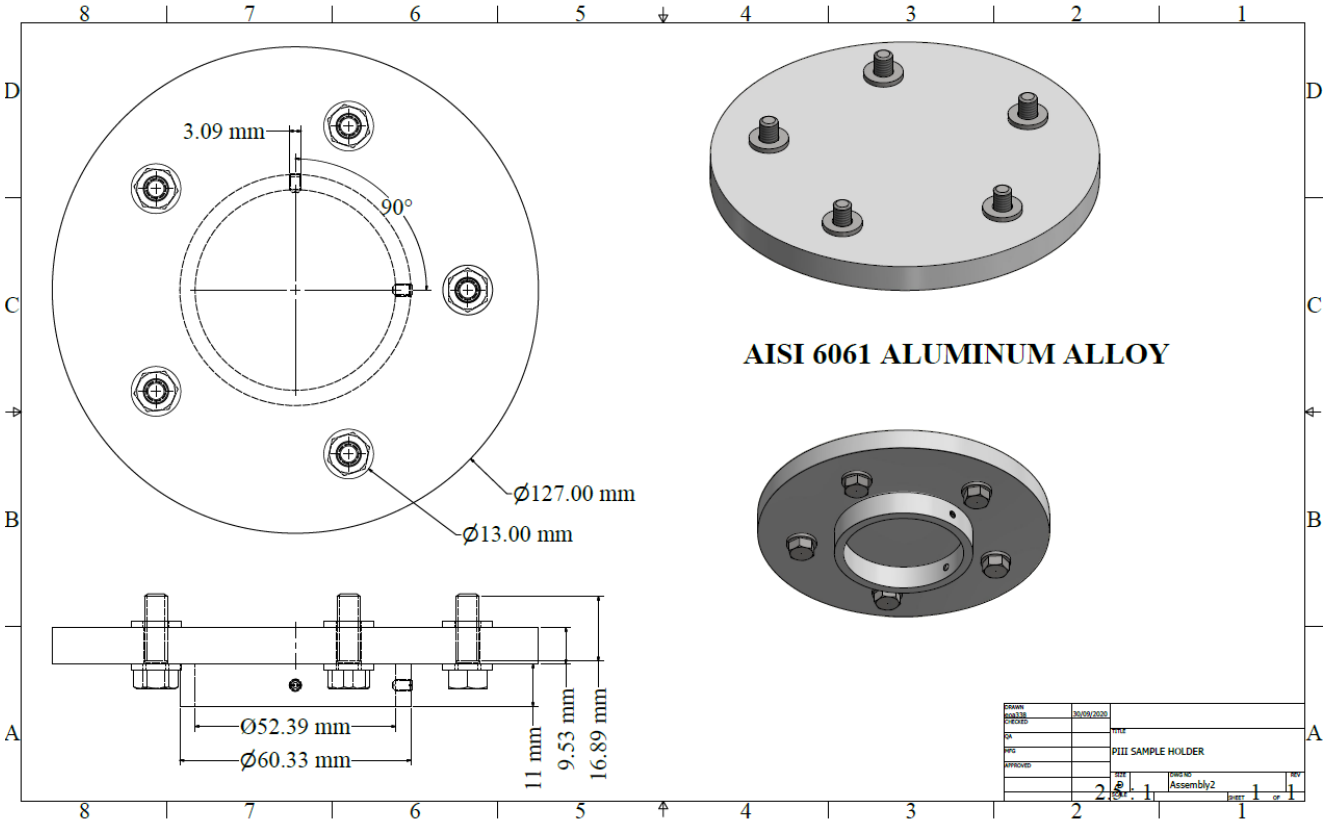

Figure 3.8. Part drawing of the specimen holder.

Aluminum was chosen for the construction of this base because it was readily available at the engineering shop. Screws and washers were used to hold the samples steadfastly to the base. Figure 3.9 shows the base and fatigue samples loaded in the Plasmonique chamber.

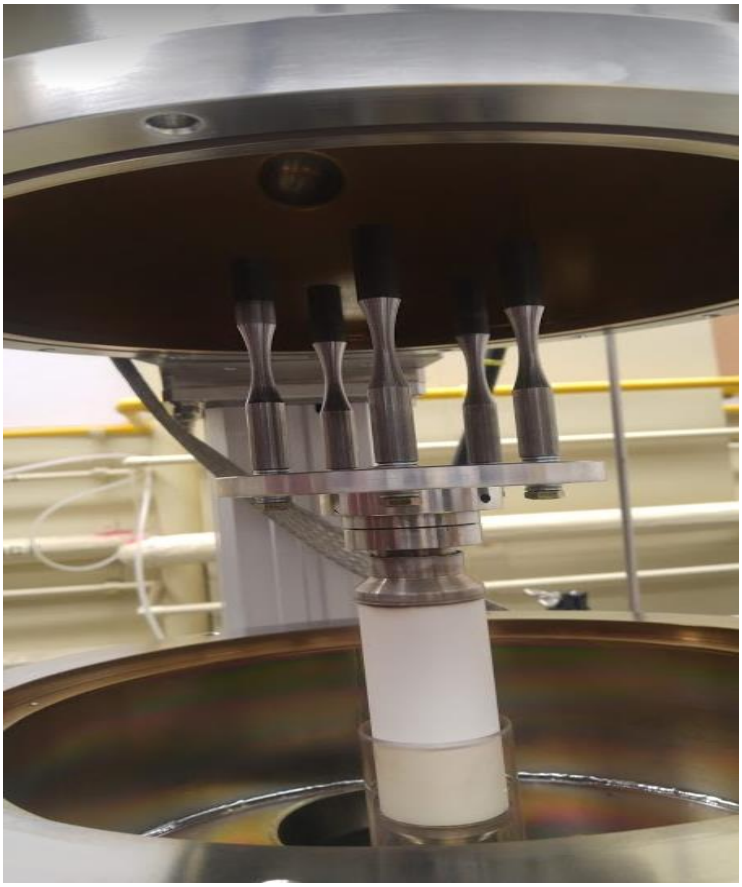

Figure 3.9. Fatigue samples installed on a specimen holder and loaded into the Plasmonique vacuum chamber.

3.4 Preliminary tests

After repairs of some of the major components, the Plasmonique machine was tested and more modifications were performed.

3.4.1 Calibration of the voltage feeder

The supply voltage feeder gauge was recalibrated to ensure that the voltage supplied to the chamber was accurate. A multimeter was used to measure the voltage supplied at the source and a digital oscilloscope measured the voltage supplied to the chamber. New marks were inscribed on the voltage input wheel as shown in Figure 3.10. The maximum voltage for safe running of the

machine was determined to be 1000 V. Figure 3.11 shows the voltage imputed to the system and the final voltage measured at the specimen undergoing PIII treatment.

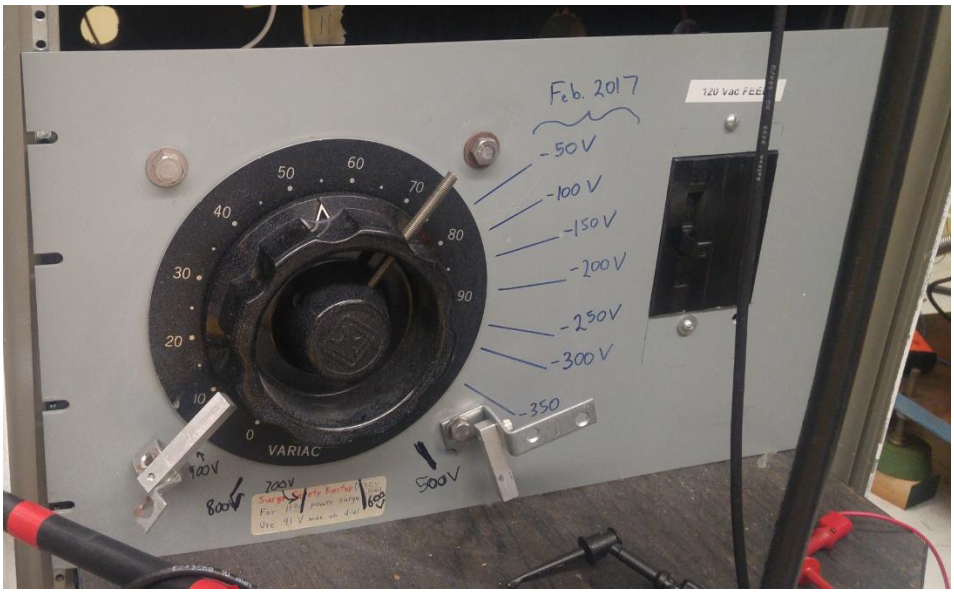

Figure 3.10. Voltage feeder calibrated.

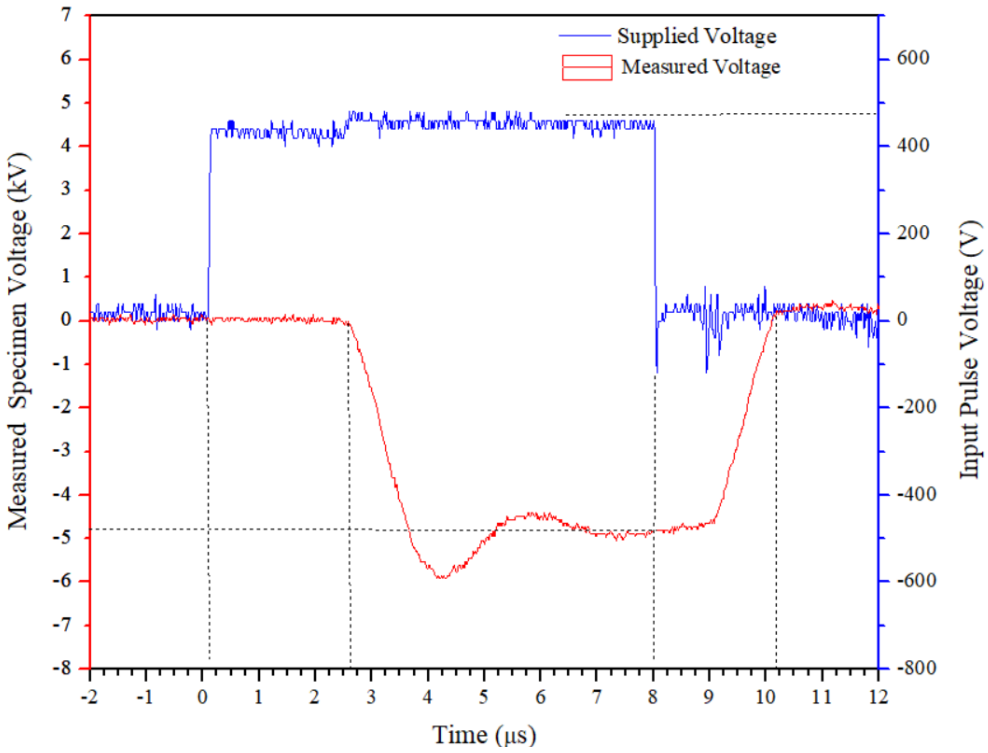

Figure 3.11. Applied and measured pulsed voltages supplied to specimen during PIII.

The voltage measured at the specimen had an overshoot initially, but later plateaued at -5 kV. The transformer and system setup were responsible for this. Two major obstacles to the efficient application of constant voltage-accelerating pulses include: the peripheral passive circuitry which plays a significant role in pulse shaping and power loss and non-ideal switching elements which can significantly degrade pulse shape, efficiency, and cost of a PIII system [59].

A co-plot of the voltage and current flowing through a specimen during a PIII treatment is shown in Figure 3.12. A Tektronix probe model P6015A was used to acquire high voltage supplied, while the current was measured using a Pearson current probe model 150 which has a sensitivity of 0.5 V/A. The voltage and current measured were recorded on a Tektronix TDS 210 oscilloscope.

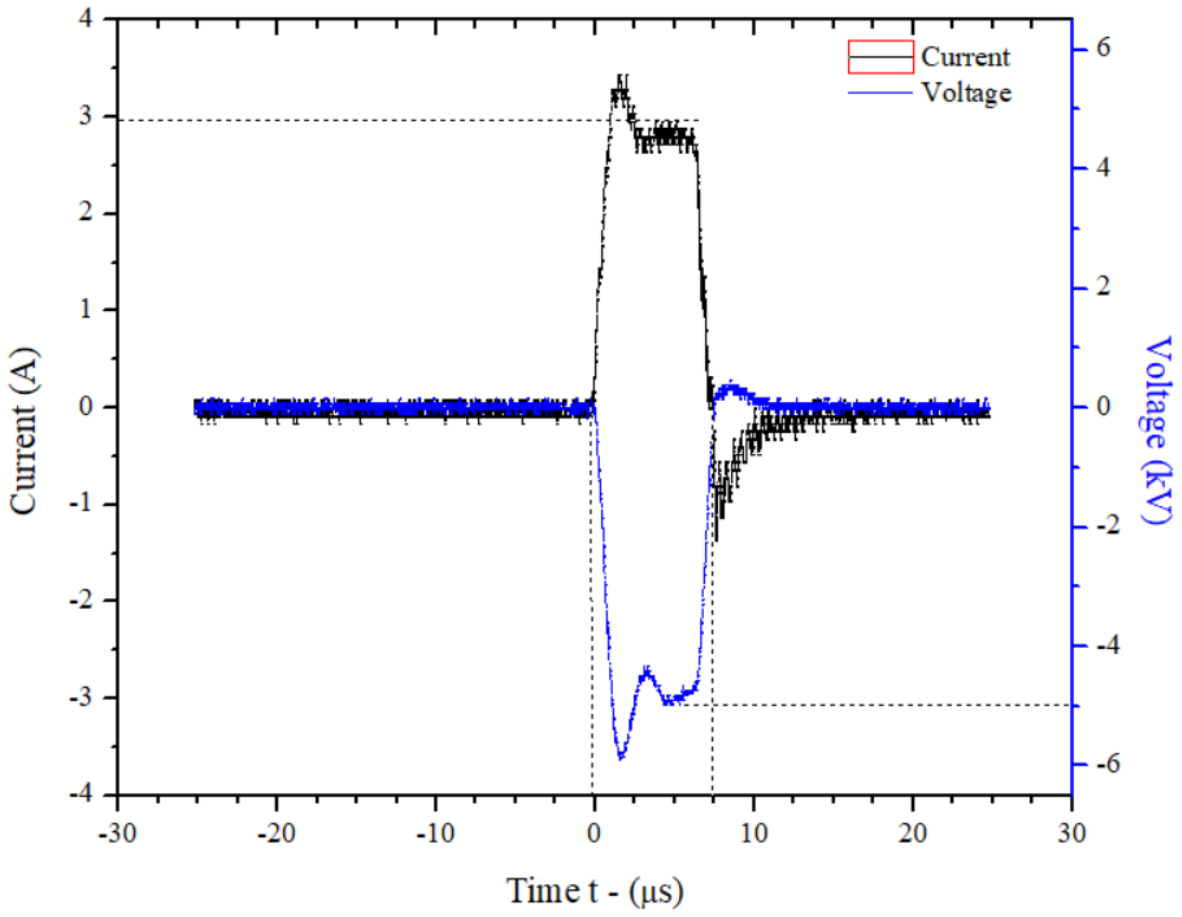

Figure 3.12. Pulsed voltage and current flowing through specimen during PIII.

3.4.2 **Langmuir probe measurements**

A Langmuir probe (Figure 3.13) was used to determine the electron density, electron temperature and electric potential of the plasma. The wattage supplied to the plasma generator and the vacuum pressure within the chamber are parameters that can be controlled externally. However, the density of ions, the electron temperature and electric potential of the plasma generated were needed to regulate the fluence of ions per dose and concentration of ions implanted into the specimen. The chamber was pumped down with a roughing pump first, and then a turbo pump to a pressure of ~10^{-7} Torr. Gas flow was kept constant at 12 sccm using a mass flow controller bringing the pressure up to 15 mTorr. A radio frequency watt meter was used to supply the power needed to generate the plasma. The reflected power was kept below 10 % of input power.

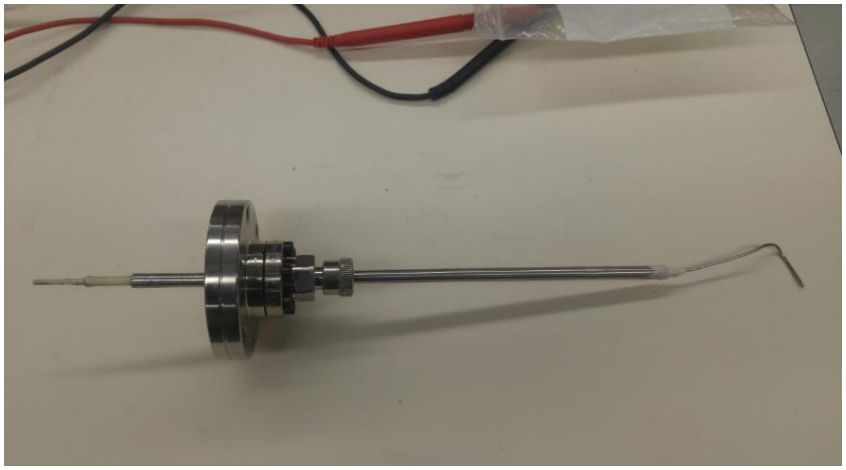

Figure 3.13. A Langmuir probe used to determine various plasma characteristics.

A single Langmuir probe made of tungsten was used for the measurements. Its inner diameter is 0.31 mm and 5 mm of its tip was exposed to plasma. Three sweeps were taken for each test at a frequency of approximately 25 Hz. The voltage was supplied by a Kepco BOP-1M 4888 power supply which was modulated by an HP function generator model 3311A. While the algorithm used to obtain the temperature and plasma densities from a Langmuir probe measurement was relatively simple, several factors such as the probe surface contamination, electronic circuit design and the position of probe installation were considered for accurate measurements. The measured current response as a function of the applied voltage for a nitrogen plasma generated by 200 W RF power at 15 mTorr working pressure with a base pressure of the order of 1microTorr is shown in Figure

3.14 (a) and (b). The intersection of the pre-electron saturation line and electron current saturation line yielded a plasma potential of 22.5 $\pm$ 1 V. The probe drew equal electron and ion current at 17 $\pm$ 1.2 V, which was the floating potential.

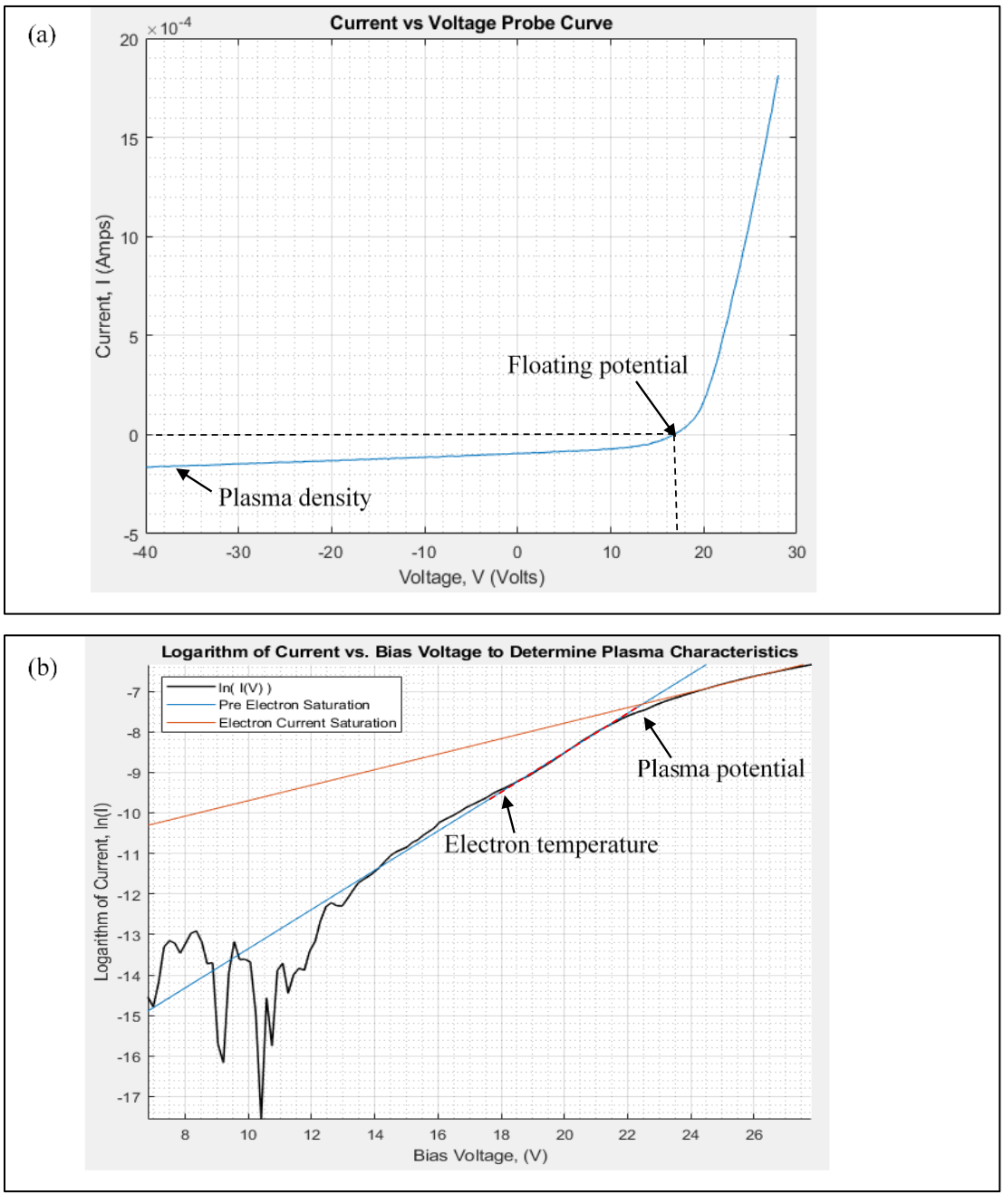

Figure 3.14. (a) A current-voltage curve obtained from Langmuir probe data for a nitrogen plasma generated using 200 W power at 15 mTorr pressure. (b) Log of current vs voltage plot used to determine plasma characteristics.

3.4.2.1 Electron temperature

The electron temperature T_e was estimated from the exponential regime of the I-V curve (Figure 3.14 a). It is the inverse slope in the log current-voltage plot between the plasma potential and floating potential. T_e was estimated using equation (3.2).

$$T_e = \frac{\Delta V}{\Delta \ln (I)} \tag{3.2}$$

An appropriate number of data points was used to calculate an electron temperature of 2.47 ± 0.09 eV by applying least square fitting to the pre-electron saturation slope of Figure 3.14 b. The electron temperature measured by Risch [60] and that obtained in this measurement tally. Li [61] found that electrons do not strictly follow the Maxwellian distribution, which adds to the error for the electron temperature.

3.4.2.2 Plasma potential

According to Lieberman [46], the sheath potential at a floating wall V_0 can be derived from the condition of equal ion and electron fluxes at the sheath boundary. Neglecting the effects of grounded walls, the plasma potential is approximately the floating wall potential.

$$V_0 \approx V_p = \tfrac{1}{2} T_e \ln \left(\frac{m_i}{2\pi m_e} \right) \tag{3.3}$$

where $T_e = 2.47$ eV is the electron temperature, m_i is the effective mass of the ions, and m_e is the electron mass. The value of $V_p = 22.23$ V from equation (3.3) with the assumption that the electron temperature was correctly measured. This value compares well with the measured value of 22.5 eV within the 10% error due to setup.

3.4.2.3 Plasma density

The ion density and electron density obtained by the Lagmuir probe analysis (using p2i code) were 3.78 x 10^9 cm^{-3} and 1.73 x 10^9 cm^{-3}, respectively. The ion density was higher than the electron density by a factor of 2 during implantation process, which was also observed by Risch [60] and Tusyewski and Tobin [62]. RF interference causes the over-estimation of ion densities and electron

temperature. The ICPII machine setup poorly shields the Lagmuir probe against RF which explains the higher ratio in my study. This can be corrected by using an RF-compensated Langmuir probe.

3.5 Depth distribution

The mean ion penetration depth is determined by the energy distribution function of implanted ions. The depth distribution of nitrogen ions implanted into carbon steel was calculated using a software called Stopping and Range of Ions in Matter (SRIM). SRIM utilizes statistical algorithms in a quantum mechanical treatment of ion-atom collision [63]. The underlying principle of the simulation is to follow many ion histories with dimensions of energy, position, and direction. The particle only changes direction due to binary nuclear collisions and moves in a straight free flight path between collisions. Once the energy of the particles drops below a defined threshold or goes outside the defined boundary, it is no longer followed.

The present research was concerned with the depth distribution of nitrogen ions in AISI 1018 and AISI 1045 carbon steels for an incident energy of 5 keV. SRIM was used to simulate the depth distributions in AISI 1018 and AISI 1045 for 50,000 mono-energetic nitrogen ions. The distribution of implanted nitrogen ions, also referred to as depth profile, has a Gaussian shape and can be characterized by the mean and standard deviation. These are called range and straggle, respectively. The stopping range of nitrogen ions in AISI 1018 and AISI 10145 steels for various ion energy ranges (2 keV to 6 keV) generated from SRIM simulations are presented in Table 3.2.

From Table 3.2, it is apparent that the effective depth where most nitrogen ions stop within the implanted specimen when different implantation energies are applied is the same for both AISI 1018 and AISI 1045 steels. The depth of implanted nitrogen ion increases with increase in voltage supplied to the specimen.

Two species of nitrogen - N^+ and N_2^+ - are implanted during the PIII process. The dominance of N_2^+ ions in the plasma decreases the maximum attainable layer depth. The range of N^+ ions implanted in both grades of steel with the full potential of –5 kV is 66 A, whereas the projected range of N_2^+ is only 38 A for -5 kV. SRIM is used to determine the depth-dependent dose level

under the assumption that the target specimen does not undergo any significant changes in volume during the process. It ignores the effect of sputtering, injected ions, and void swelling on the redistribution of the dose and implanted nitrogen. The depth profiles of nitrogen implanted into AISI 1018 and 1045 steel with -5 kV voltage pulse are shown in Figures 3.15 and 3.16, respectively.

Table 3.2. Projected range of nitrogen ion in AISI 1018 and AISI 1045 steels.

Ion Energy (keV)	AISI 1018 Projected Range (Å)	AISI 1045 Projected Range (Å)
2.00	32	32
2.25	35	35
2.50	38	38
2.75	41	41
3.00	44	44
3.25	47	47
3.50	50	50
3.75	52	52
4.00	55	55
4.50	61	61
5.00	66	66
5.50	72	72
6.00	77	77

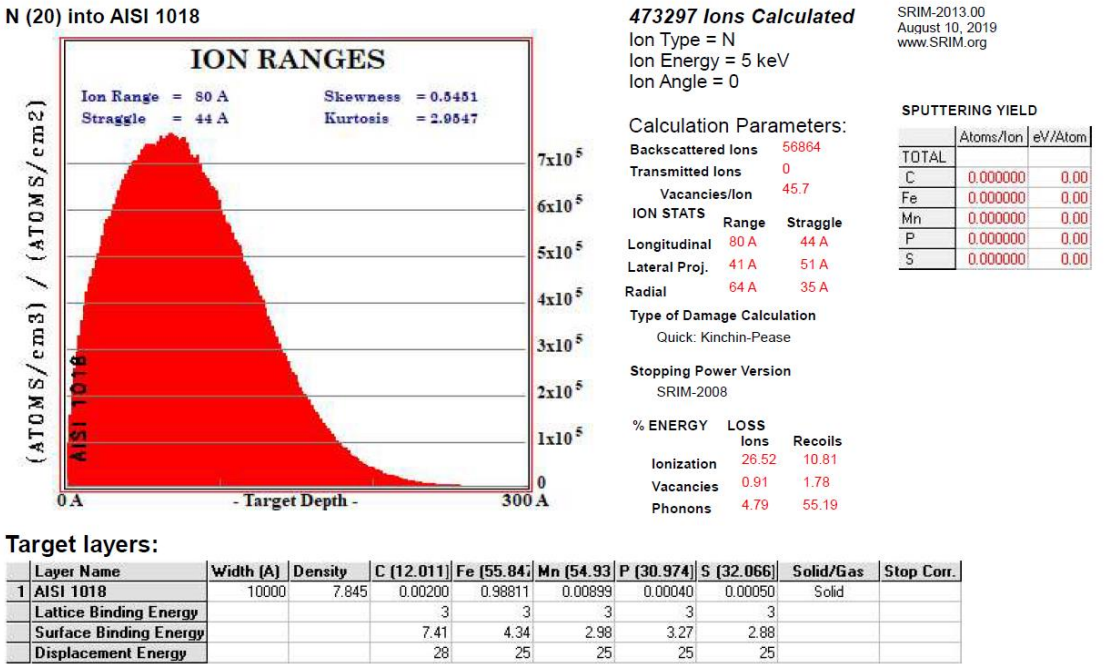

Target layers:

	Layer Name	Width (A)	Density	C (12.011)	Fe (55.847)	Mn (54.93)	P (30.974)	S (32.066)	Solid/Gas	Stop Corr.
1	AISI 1018	10000	7.845	0.00200	0.98811	0.00899	0.00040	0.00050	Solid	
	Lattice Binding Energy			3	3	3	3	3		
	Surface Binding Energy			7.41	4.34	2.98	3.27	2.88		
	Displacement Energy			28	25	25	25	25		

Figure 3.15. Projected range of nitrogen in AISI 1018 simulated using SRIM.

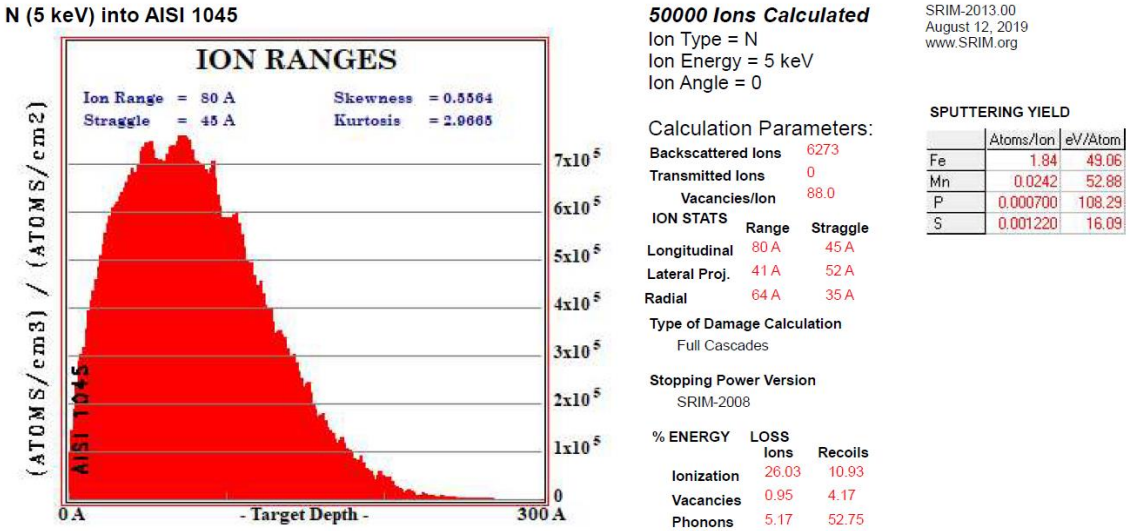

Target layers:

		Moving atom colors ->								
		Stopped atom colors ->								
	Layer Name	Width (A)	Density	C (12.011)	Fe (55.847)	Mn (54.93)	P (30.974)	S (32.066)	Solid/Gas	Stop Corr.
1	AISI 1045	10000	7.831	0.00449	0.98564	0.00897	0.00040	0.00050	Solid	1
	Lattice Binding Energy			3	3	3	3	3		
	Surface Binding Energy			7.41	4.34	2.98	3.27	2.88		
	Displacement Energy			28	25	25	25	25		

Figure 3.16. Projected range of nitrogen in AISI 1045 simulated using SRIM.

This simulation results are based on 50,000 ions. The following assumptions were made: (a) the implanted particles are mono-energetic, (b) the nitrogen molecules break into single atoms, (c) the molecules energy is distributed equally amongst daughter atoms, and (d) the temperature during implantation is low enough to neglect diffusion.

3.5.1 **Fluence**

Fluence is the total number of ions in the sheath that are accelerated toward a unit area of the specimen. If their energy and trajectory permit, they are stopped within the target; such ions will contribute to the dose (units of ions per unit volume) of the specimen. Previous experiments suggest that the target fluence can be accounted for by multiplying the plasma density (η_0) by the volume of plasma between the target and the expanded sheath, divided by the area of the target ($r0$) [6].

$$F = \eta_0 \times \frac{(rS^2 - r0^2)}{r0} \tag{3.4}$$

The goal for a total fluence of 5 x 10^{17} cm^{-2} was obtained from literature[40].

3.5.2 **PIII treatment**

Specimens to be implanted were loaded into the vacuum chamber and the pressure was brought down to 13 mTorr. Nitrogen gas was then supplied to the chamber at 12 sccm. The RF power used was 250 W and a bias voltage of -5 kV was supplied to the specimen. The implantation time was set for 2 h. All settings were kept constant for every run, to maintain the same ion energy distribution. Settings used for all PIII treatments are summarized in Table 3. The steps taken to generate vacuum, start and end the PIII treatment are outlined in Appendix B.

Table 3.3. Independent parameters and their values used for PIII experiment.

Parameter	Value
Base pressure	< 3 x 10^{-7} Torr
Working pressure	15 ± 1 mTorr
Gauge position	70 %
Sccm	12
RF power	250 W
Series matching (Tune)	35%
Shunt matching (Load)	90%

3.6 Surface roughness measurements

To determine the effect of PIII treatment on the surface roughness of steel specimens, three specimens of AISI 1018 and AISI 1045 steel were cold mounted for polishing using acrylic resin. The cold-mounted samples were pre-ground using 320 (46 µm), 500 (30 µm) and 1200 (15 µm) SiC grit emery papers and finally, fine ground using 2000 (10 µm) and 4000 (5 µm) SiC grit emery papers. Surface roughness measurements were then taken using the NewView 8000 Optical Profiler found in room 0C19, Engineering building, University of Saskatchewan (see Figure 3.17). Roughness measurements were taken before PIII treatment, after two hours of PIII treatment and after five hours of PIII treatment for each specimen.

Figure 3.17. Zygo NewView optical profilometer.

3.7 Microhardness test

To investigate the effect on treatment time on the harness of AISI 1018 and AISI 1045 steels, specimens were PIII treated for 2, 3 and 5 hours and their microhardness was measured using a Mitutoyo MVK-H1 Vickers microhardness tester, which is located in Room 2C26, Engineering Building, University of Saskatchewan. A load of 500 gf was used with a resident time of 15 seconds. The test was performed according to ASTM E384-17 standard [64]. At least 5 readings were taken for each specimen, so the hardness data reported are averages.

3.8 Nanohardness test

A CETR Universal Material Tester (UMT) nano indentation machine located in Room 1B22, Engineering Building, was used to measure the nanohardness of PIII treated AISI 1018 and AISI 1045 steel specimens in accordance with ASTM E2546-07 standard [65]. Loads were applied in increments of 3 mN from 3 mN to 21 mN. For each load, 5 locations on the specimen were tested and their responses recorded. Test data was processed and analyzed using a software based on Oliver and Pharr method [66]. Figure 3.18 displays the picture of a nanoindentation system.

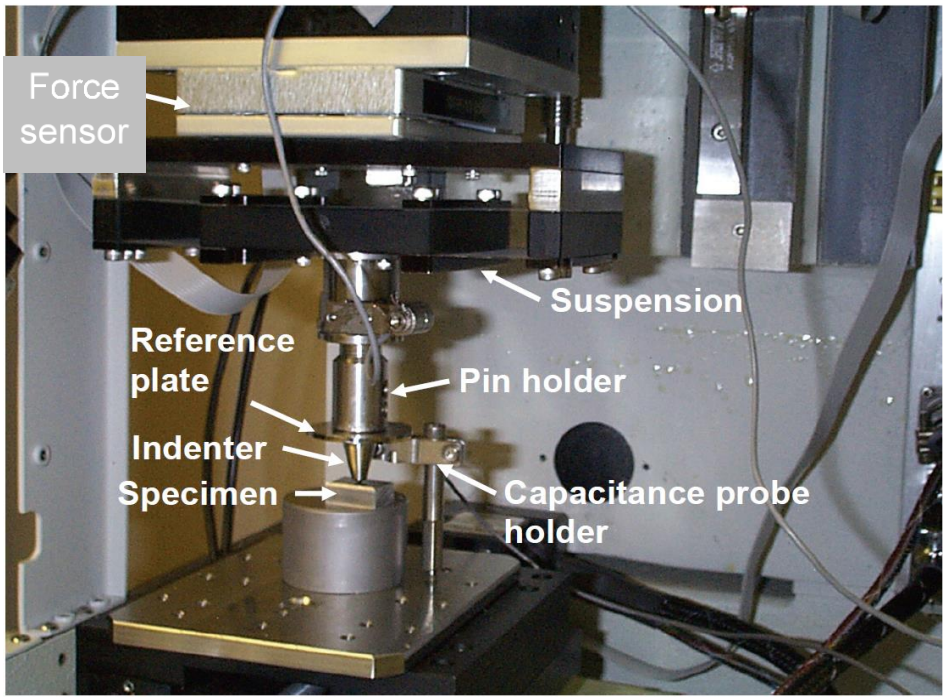

Figure 3.18. Picture of the UMT nanoindentation test set-up.

Figures 3.19 (a) and (b) show respectively the typical load-displacement responses obtained for untreated specimens of AISI 1018 and AISI 1045 steels at peak loads of 1 mN, 9 mN, and 21 mN. The response is a plasticity dominated, parabolic loading curve with little elastic recovery of the depth displacement on unloading typical of ductile materials [67]. Similar plots obtained for AISI 1018 and AISI 1045 specimens plasma treated for 2 h are shown in Figures 3.20 (a) and (b), respectively. The following changes are observed: (i) Compared to the untreated specimens, the displacement at each peak load is reduced, the effect being more pronounced in treated AISI 1045 steel. There is more resistance to displacement in the treated samples compared to the untreated ones. (ii) Compared to the untreated specimens, the load–displacement curves reveal increased elastic recovery on unloading, meaning that a higher proportion of the deformation occurred elastically. Again, the effect is more evident in treated AISI 1045 steel. (iii) As the unloading curves become less steep – due to a larger proportion of elastic recovery of the indenter displacement, very significant levels of elastic recovery occurred during the final staged of unloading which is thought to be driven by the drum-skin effect of membrane and residual stresses of the treated layer [67]. This is very evident for AISI 1045 steel. The resistance to the indenter displacement indicates that the nitrogen atoms within the surface caused the hardness of the surface layer to increase.

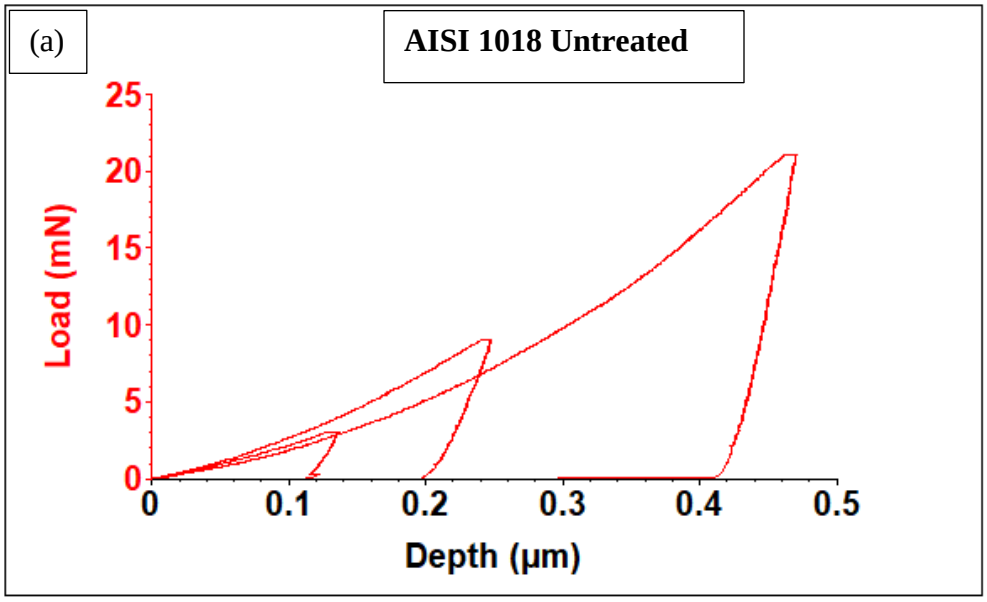

Figure 3.19. Load-displacement curves obtained for (a) untreated AISI 1018 steel. (b) untreated AISI 1045 steel.

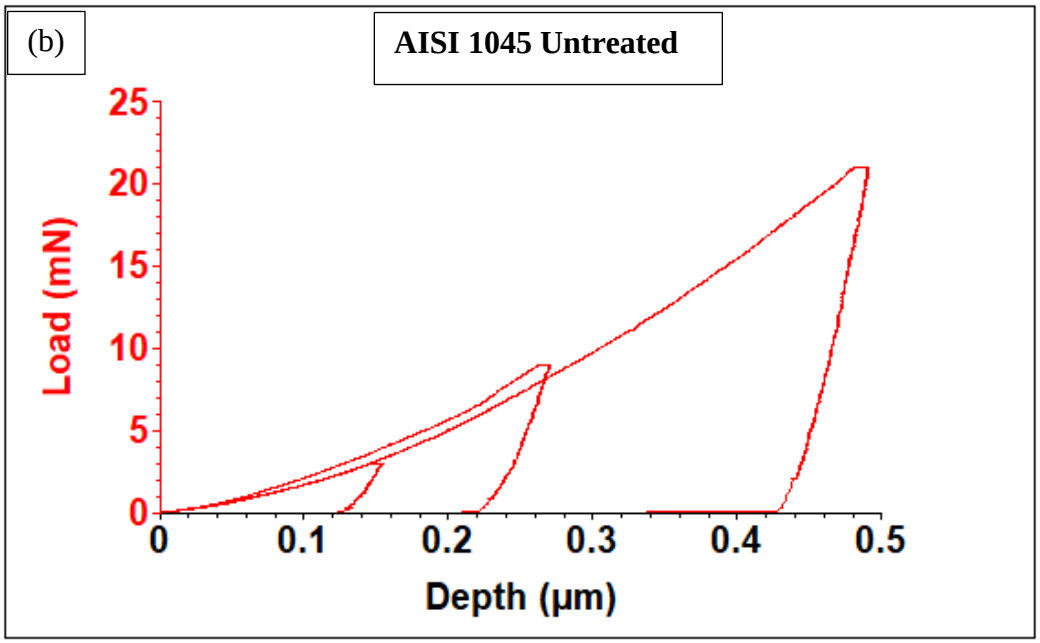

Figure 3.19. Continued.

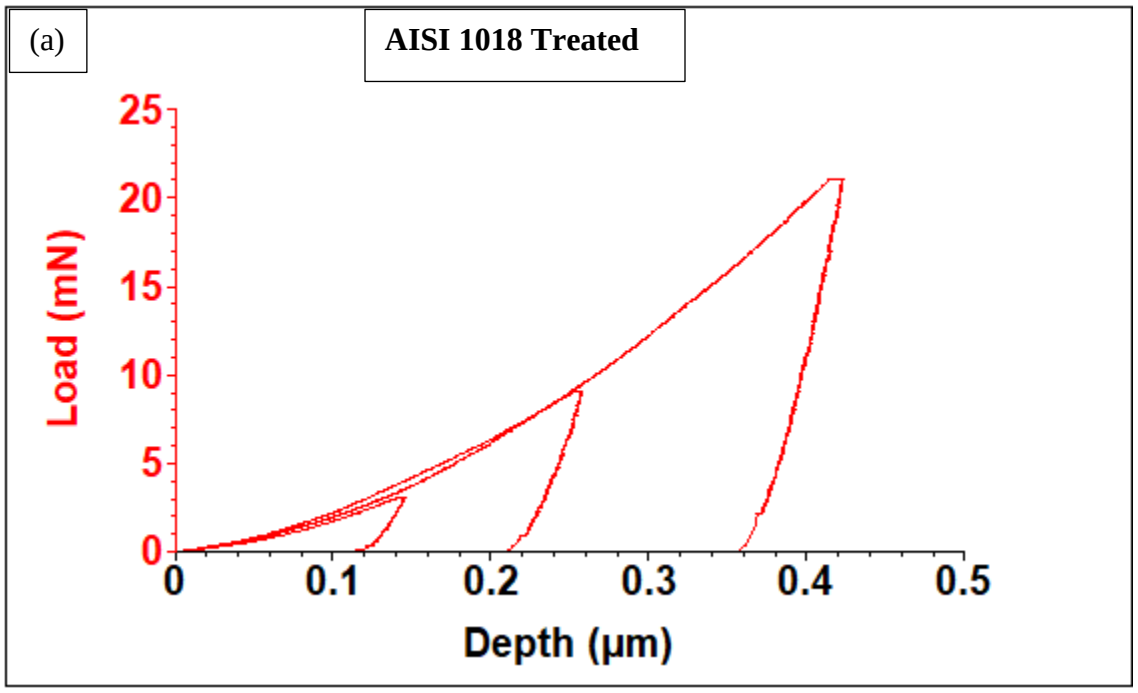

Figure 3.20. Load-displacement curves obtained for (a) treated AISI 1018 steel. (b) treated AISI 1045 steel.

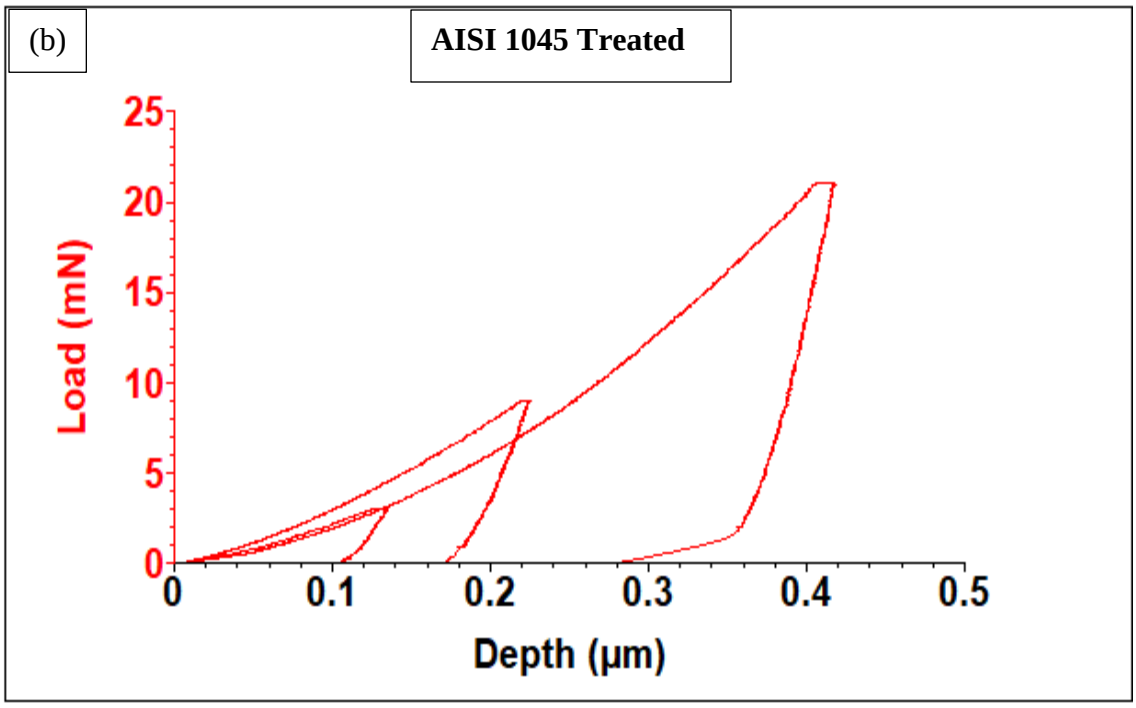

Figure 3.20. Continued.

Elastic and plastic deformations are included in the measured displacements. Therefore, it is necessary to eliminate the elastic contribution to calculate just the plastic depth from which the area can be determined using the geometry of the indenter. Figure 3.21 shows a characteristic hardness plot. A tangent line is marked to the unloading curve from the maximum load point to the zero.

The Young's modulus is related to the slope of this tangent line and could be deduced using

$$E = 0.149\left(\frac{S}{h_p + h_0}\right) \tag{3.5}$$

where S is the contant stiffness (N/m), h_p the plastic depth under loading (m) and h_0 the tip indenter defect (10^{-9} m).

The hardness H can be calculated as

$$H = 0.0378\left[\frac{L_{max}}{(h_p + h_0)^2}\right] \tag{3.6}$$

where L_{max} corresponds to the maximum load (N), thus the elastic deformation is the difference between the maximum indent h_{max} and h_p .

The accuracy of hardness values measured strongly depends on the indentation depth and the thickness of the implanted layer. Another important consideration is that nanohardness testers can be very sensible to vibration and sample roughness.

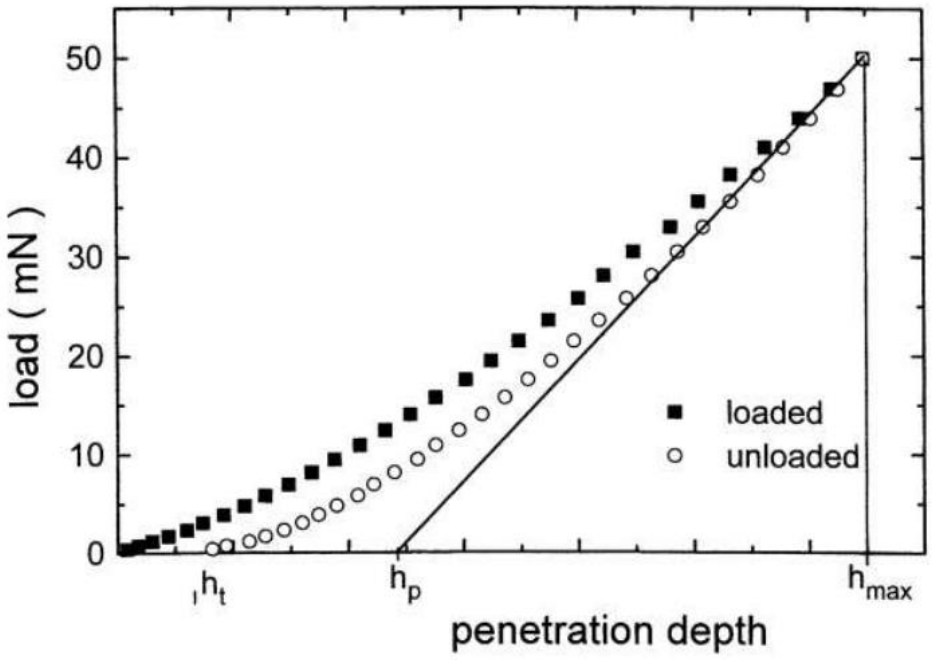

Figure 3.21. A typical loading and unloading curve of a nanohardness test.

3.9 XPS analysis

X-ray photoelectron spectroscopy (XPS) measurement was done primarily to ascertain the amount of nitrogen ions implanted into the PIII treated steel specimens. All XPS measurements were collected using a Kratos (Manchester, UK) AXIS Supra system at the Saskatchewan Structural Sciences Centre (SSSC) (Figure 3.22). This system was equipped with a 500 mm Rowland circle monochromated Al K-α (1486.6 eV) source, a combined hemi-spherical analyzer (HSA) and spherical mirror analyzer (SMA). A spot size of hybrid slot (300 μm x 700 μm) was used. All survey scan spectra were collected in the -5-1200-binding energy range in 1 eV steps with a pass energy of 160 eV. High resolution scans of 2 regions were also conducted using 0.1 eV steps with a pass energy of 20 eV. An accelerating voltage of 15 keV and an emission current of 15 mA were used for the analysis. An Ar^+ ion gun was used for sputtering the surface of the samples. Sputtering

was done using a 4 keV ion beam, and a 3 mm raster. Sputtering was done in 2 sec intervals from 2-10 seconds and then for 50 seconds (for a total of 60 seconds sputtering). Survey scans were collected between all sputtering cycles. High resolution N1s and C1s (for energy calibration) were collected after 2 seconds of sputtering and 4 seconds of sputtering for comparison on sample M1T2B for both AISI 1018 and AISI 1045 steel specimens. Quantification of XPS spectra in terms of atomic concentration was performed using the CasaXPS version 2.3.19PR1.0.

Figure 3.22. AXIS Supra system used for XPS test.

3.10 X-ray diffraction

X-ray diffraction (XRD) measurement of PIII-treated specimens was carried out using a PANalytical Empyrean X-ray diffractometer with a Co target, rotating stage and goniometer in 2θ configuration (manufactured by PANalytical Inc. Westborough MA, United States). The wavelength of Co radiation is 0.179 nm. The generator was utilized at 40 kV and 45 mA. The intensities were measured from 5^o to 110^o at 2θ with step size of 0.0167^o and a scan speed of 0.015 degree/sec. The radiation used was full spectrum Co ($K_{\alpha 1}$, $K_{\alpha 2}$) with the K_β filtered out with a diffracted side Fe filter. The results were analyzed using PANalytical X' Pert HighScore software version 4.7.

3.11 Fatigue test

To investigate the fatigue properties of AISI 1018 and AISI 1045 PIII treated and untreated steel, specimens were subjected to cyclic loading conditions to induce fatigue failure. A Krouse rotating cantilever beam machine (see Figure 3.23), located in Room 2C24, Engineering Building, was used to perform the fatigue test following ASTM STP 566 standard [5]. Cylindrical fatigue specimens were clamped into the Krouse machine using a set of two freely rotating collets. One of these collets was connected to a DC motor, while the other was connected to a load arm. Using a sliding weight, a moment was applied to the specimen at the end of the load arm. The bending moment applied was calculated by equations (3.7) and (3.8).

$$\sigma = \left(\frac{32M}{\pi d^3}\right) \tag{3.7}$$

$$M = \frac{\sigma \pi d^3}{32} \tag{3.8}$$

where M is the bending moment and scale beam reading in inch pounds, d the diameter of the specimen, and σ the desired stress. To convert the unit to N·m, the value of M was divided by 8.85666. σ is the bending stress at the minimum section of the specimen in Pa. d is the diameter of the minimum section of the specimen in m. Therefore, the stress amplitude (σ_a) is given by Dowling [67],

$$\sigma_a = \left(\frac{\sigma_{max} - \sigma_{min}}{2}\right) = \left(\frac{32M}{8.8566\pi d^3}\right) \tag{3.9}$$

All tests were performed at a frequency of 50 Hz and a stress ratio of -1. For each applied stress, fives specimens were tested. In each test, the number of cycles to failure was recorded; the tests were terminated if no failure occurred after 10^7 cycles.

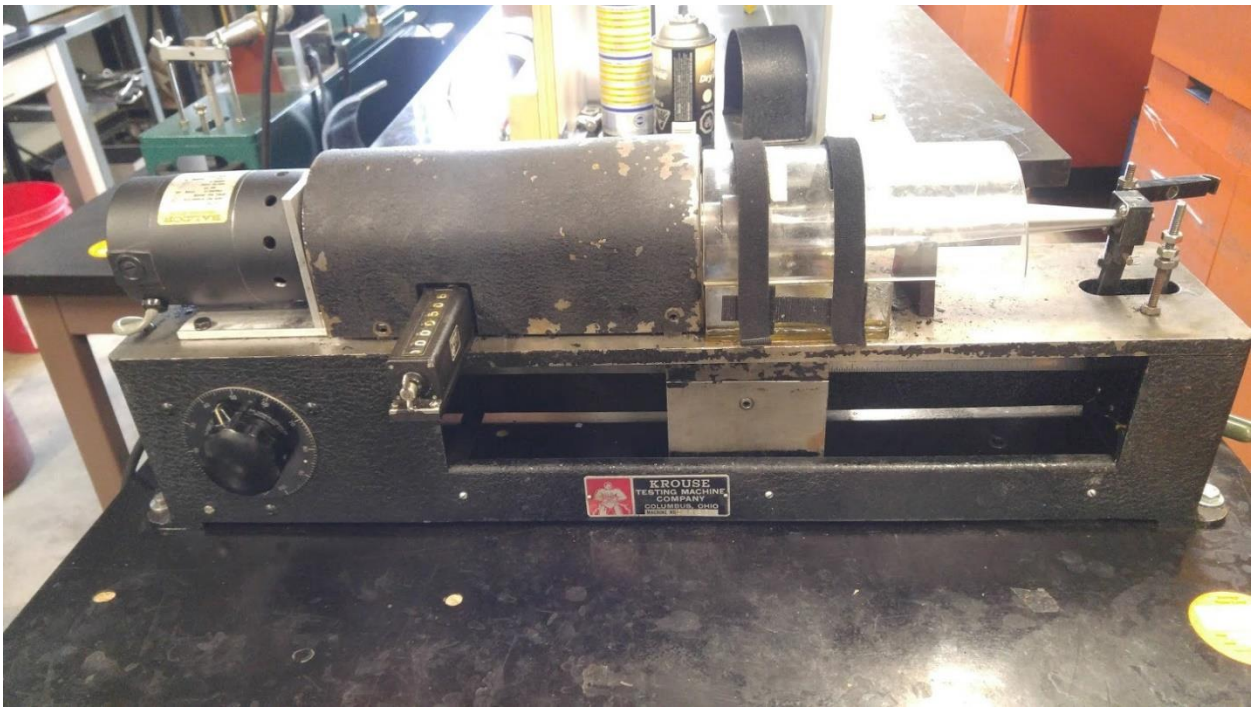

Figure 3.23. Krouse rotating cantilever beam machine.

3.12 Scanning electron microscopy

Evaluation of fracture surfaces of fatigue test specimens was conducted using a JEOL JSM-6010LV SEM and a Hitachi FE-SEM SU8010 scanning electron microscope (SEM) equipped with energy dispersive spectrometer (EDS). The fractured specimens were first cut 5 mm from the fractured surface and attached to the stage using conductive tape. An accelerating voltage of 18 kV was used.

CHAPTER 4

RESULTS AND DISCUSSION

The results obtained from the experimental investigations carried out in Chapter 3 are presented and discussed in this chapter.

4.1 Surface roughness measurement

The results of the surface roughness measurements obtained for AISI 1018 and AISI 1045 steel are shown in Figure 4.1. Here UT and T represent untreated and treated specimens, respectively. The data shown is the average of three scans. No appreciable changes in surface roughness were observed in this measurement. The surface roughness parameter, S_a, which represents the arithmetical mean height, remained practically the same for untreated, 2 h and 5 h PIII-treated specimens of AISI 1018 and AISI 1045 steels. This observation is consistent with the work of Tang [3] who reported that the barely noticeable change in surface roughness after plasma implantation treatment is typical for stiff materials such as steel because the plasma etching effect is very weak. Kim *et al.* [68] also reported that, for low roughness materials such as silicon wafer, the roughness is usually higher after plasma treatment, whereas for materials with higher surface roughness, the roughness becomes lower.

4.2 Microhardness test

Specimens of both AISI 1018 and AISI 1045 steels were loaded into the Plasmonique chamber and subjected to different lengths of time (1 h, 2 h, 3 h and 5 h) of nitrogen implantation treatment. The average values of microhardness obtained for specimens of both steels are presented in Tables 4.1 and 4.2, respectively. Figure 4.2 shows the variation of hardness with plasma treatment time for both steels. There was an increase in hardness after nitrogen ion implantation. However, the hardness values practically plateaued for treatment times above 2 h. For AISI 1018, the hardness value remained around the range of 515 -525 HV, while AISI 1045 hovered around 640 – 660 HV. At shorter treatment time (1 h), nitrogen uptake is low; therefore, the amount of hardening is also low.

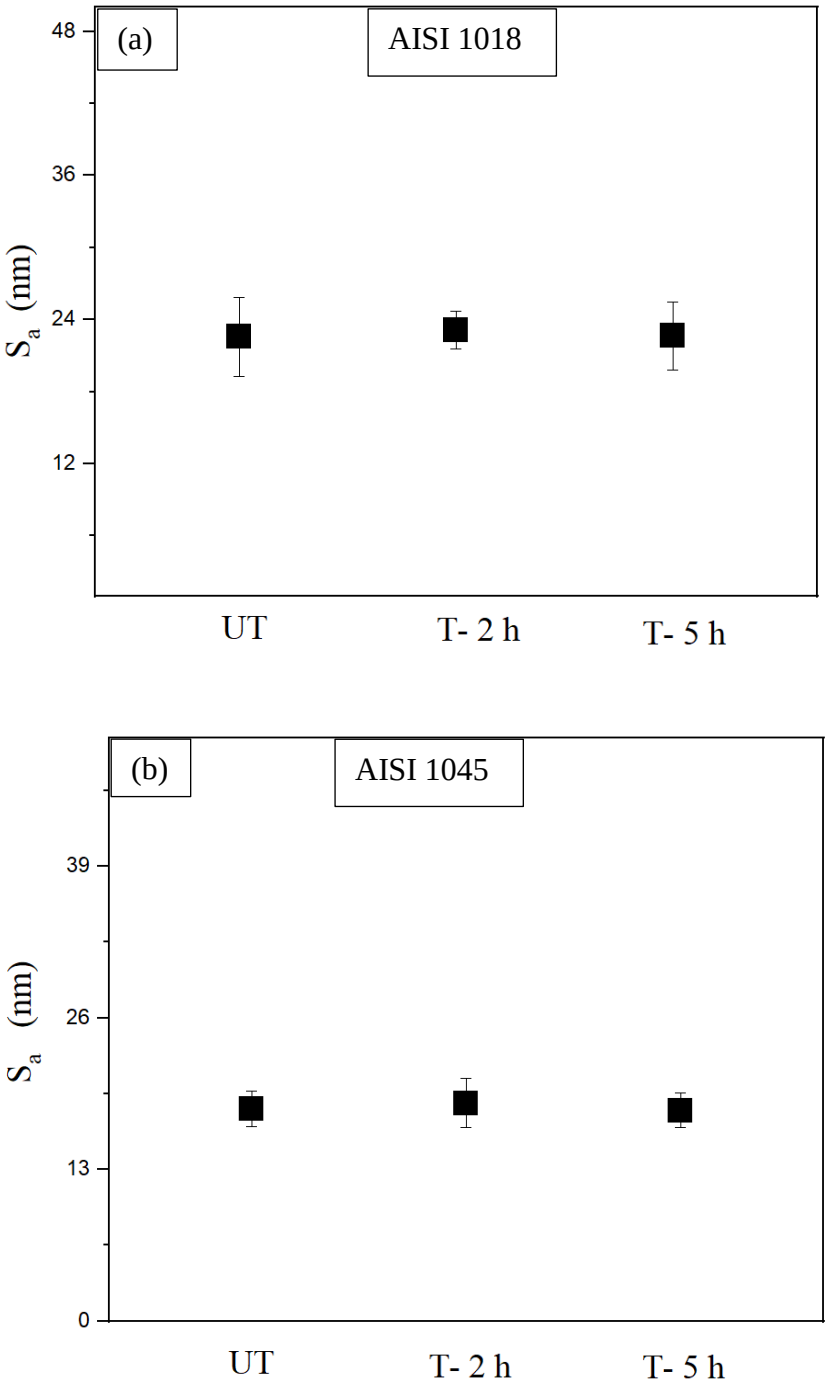

Figure 4.1. Roughness values obtained for untreated, 2-hour treated, and 5-hour treated specimens. (a) AISI 1018 and (b) AISI 1045. Error bars are based on standard deviations.

Table 4.1. Hardness data obtained for untreated and plasma treated specimens of AISI 1018 steel.

AISI 1018	**N_2^+ Conc (ions/cm^2)**	**Hardness HV**	**% increase in hardness**
UT	-	464.4±21	-
T-1 h	6.34E+16	492.8±8	6%
T-2 h	1.27E+17	522.3±13	13%
T-3 h	1.90E+17	515.2±9	11%
T-5 h	3.17 E+17	523.4±13	12%

Table 4.2. Hardness data obtained for untreated and plasma treated specimens of AISI 1045 steel.

AISI 1045	**N_2^+ Conc (ions/cm^2)**	**Hardness HV**	**% increase in hardness**
UT	-	563.7±19	-
T-1 h	6.34E+16	581.64±16	10%
T-2 h	1.27E+17	658,43±23	17%
T-3 h	1.90E+17	653.35±11	16%
T-5 h	3.17 E+17	642.46±27	14%

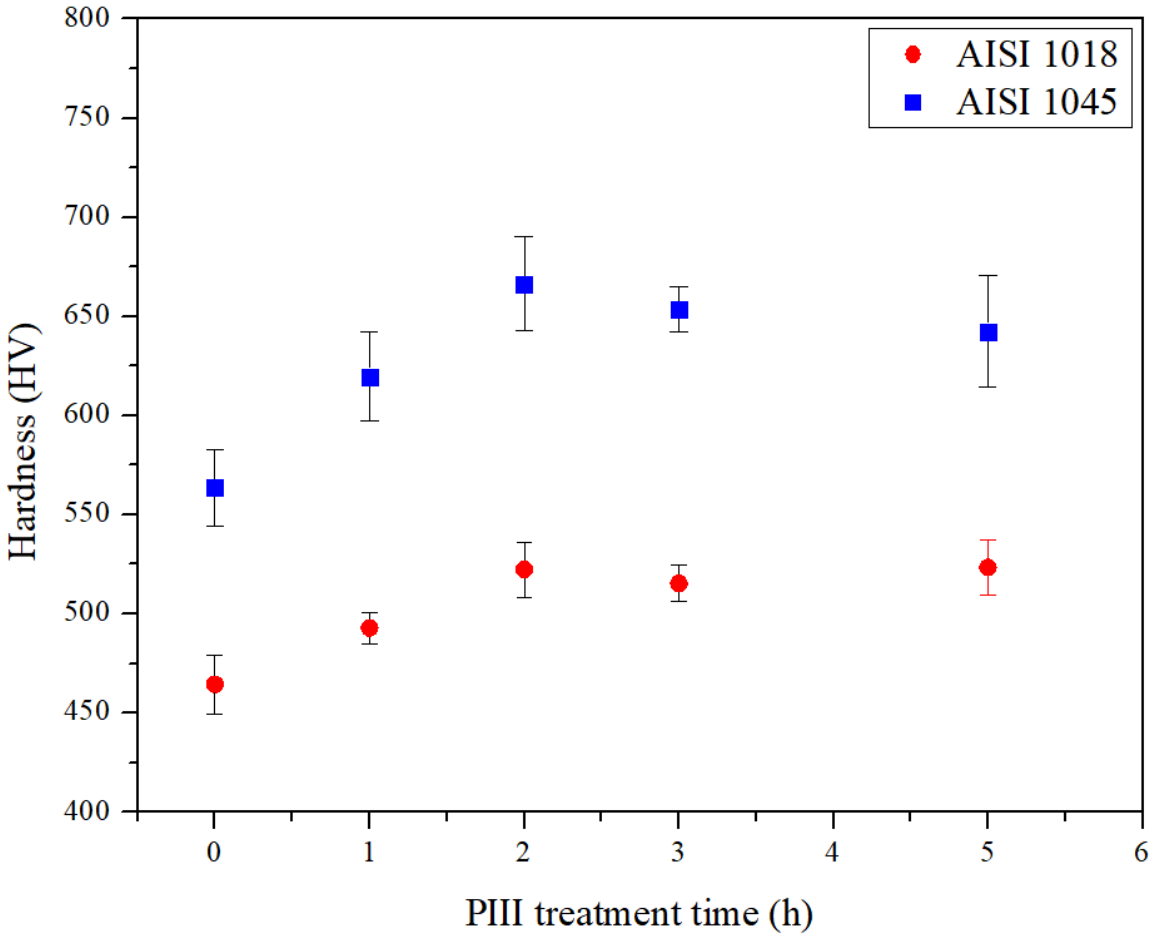

Figure 4.2. Hardness of AISI 1018 and 1045 as a function of treatment time.

Sirin *et al.* [69] reported on plasma ion nitriding of AISI 4340 at 500 °C and 540 °C. They observed a decrease in surface hardness after eight hours of treatment and attributed it to precipitate density and size. For longer treatment periods, larger nitride precipitates were formed, which were less effective in increasing hardness than smaller ones. Lui *et al.* [58] also had a similar trend after nitrogen implantation of AISI 52100 bearing steel using the PIII technique. The maximum microhardness value was reached after 4 hours of treatment after which there was a decline in hardness value. Tang *et al.*[70] observed a comparable movement in data for the free energy of the surface with processing time after an atmospheric pressure plasma treatment of AISI 304L steel. Changes in surface free energy were thought to be caused by the presence of oxides, nitrides, and radicals at the surface of the steel, which were generated by plasma treatment. When the plasma treatment time increased to a certain extent, the amount of oxides and nitrides on the surface did

not increase further because some of them transferred into non-active particles due to long-term exposure to the plasma. These non-active particles have a negative influence on the surface free energy [71].

4.3 Nanohardness

Figures 4.3 and 4.4 show plots of nanohardness vs contact depth obtained for untreated and plasma treated specimens of AISI 1018 and AISI 1045 steels, respectively. Both steels showed an increase in nanohardness after nitrogen ion implantation. The hardness gained after nitrogen implantation is higher for AISI 1045 steel than AISI 1018, which is consistent with the microhardness results presented previously. As the contact depth increased, the measured hardness value reduced following a hyperbolic trend. From the SRIM simulation (see Section 3.5), it is expected that the concentration of implanted nitrogen will peak at 40 nm after which it begins to drop and finally gets to the concentration of the bulk. This corelates fairly well with the nanohardness-depth trend of specimens that were plasma treated.

It should be noted that treated AISI 1018 specimens began to record bulk microhardness values at a depth of 120 nm from the surface whereas the bulk hardness value was reached at 90 nm from the surface for treated AISI 1045 specimens. Since AISI 1018 is a softer metal than AISI 1045, energetic N ions tend to travel to a deeper distance within the material before stopping. Also, since AISI 1045 steel has more carbon content, some of the C atoms have occupied interstitial sites which would have been available to implanted N ions, thereby reducing the number of sites available for implantation. So, a larger implantation depth for AISI 1018 resulted in less concentration of nitrogen within the implanted area and vice versa for AISI 1045 steel.

The untreated specimens of both AISI 1018 and AISI 1045 showed a slightly higher hardness value at the surface than within the bulk material. It is well known that the hardness of metal oxide is usually above that of the pure metal [72]. Therefore, it can be assumed that the harder oxide layer significantly contributes to the measurements at small contact depth.

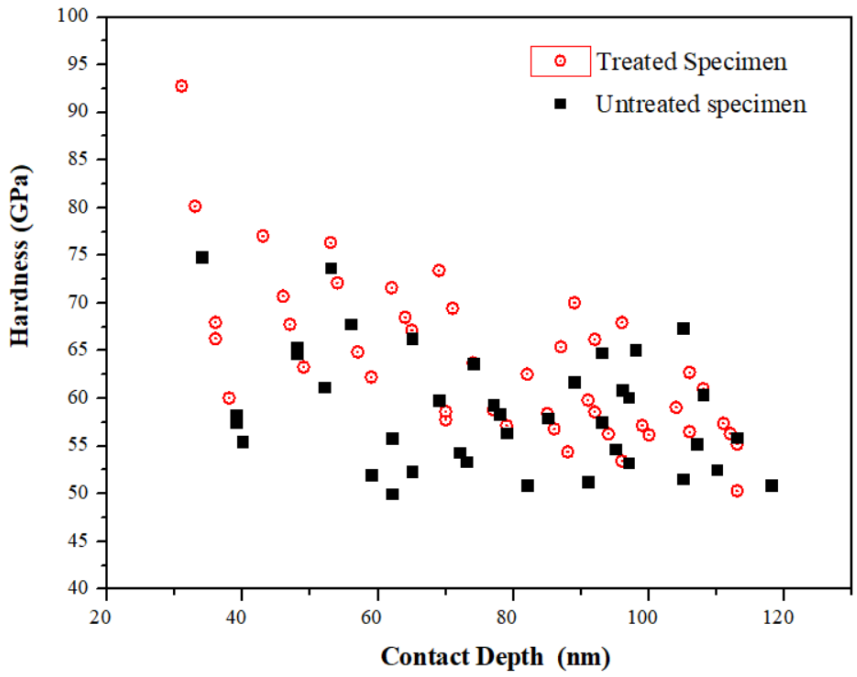

Figure 4.3. Nanohardness versus contact depth data obtained for untreated and plasma treated specimens of AISI 1018 steel.

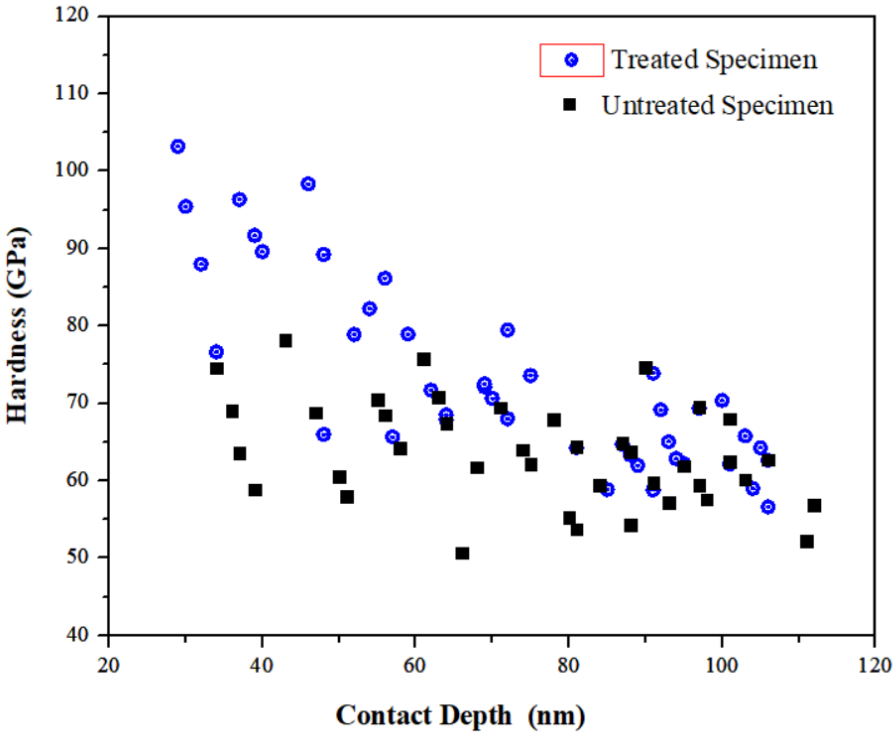

Figure 4.4. Nanohardness versus contact depth data obtained for untreated and plasma treated specimens of AISI 1045 steel.

Figures 4.5 and 4.6 show the variation of nanohardness with load applied during nanohardness measurement for treated and untreated specimens of AISI 1018 and AISI 1045 steels, respectively. As the load applied increased, the hardness of plasma treated specimens decreased while that of the untreated specimen remained virtually constant for both grades of steel. The difference in hardness between the plasma treated and untreated specimen is greater in AISI 1045 steel at low loads. However, above 13 mN, the hardness of plama treated and untreated specimens is practically the same. For AISI 1018 steel, the transition occurred at 21 mN.

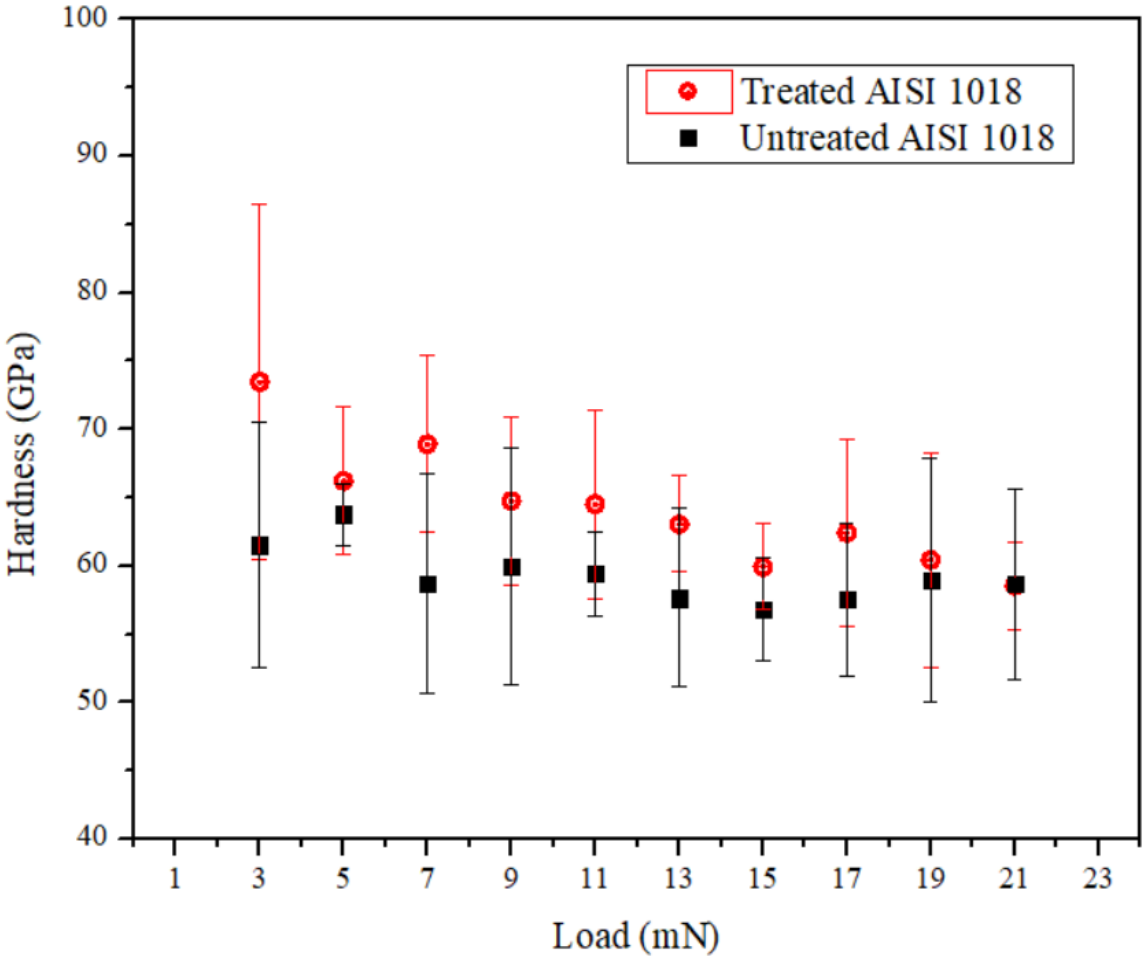

Figure 4.5. Variation of nanohardness of plasma treated and untreated AISI 1018 specimens withapplied load. Error bars are based on standard deviation.

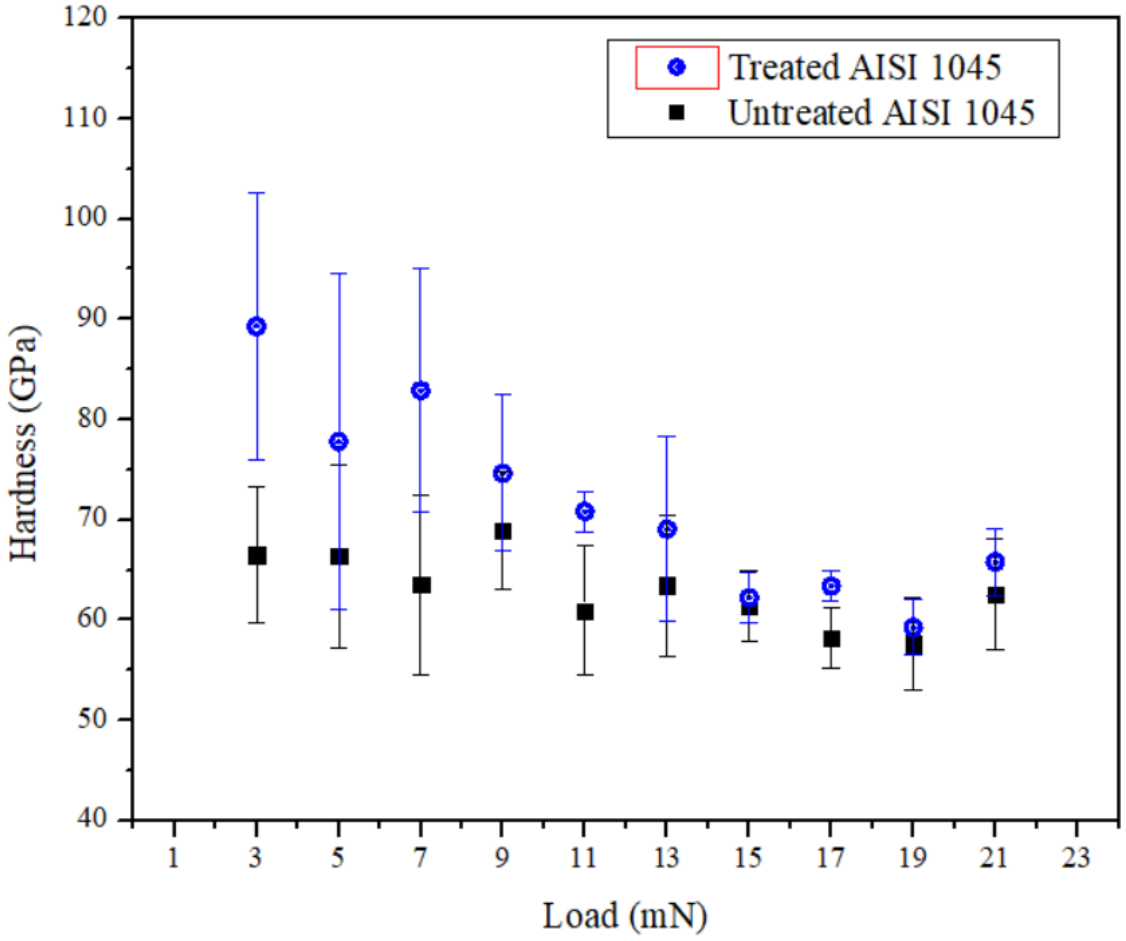

Figure 4.6. Variation of nanohardness of plasma treated and untreated AISI 1045 specimens with applied load. Error bars are based on standard deviation.

4.4 XPS analysis

Nitrogen concentration at various depths from the surface of AISI 1018 and AISI 1045 steel specimens before and after PIII treatment was acquired using XPS. The results obtained are summarized in Table 4. 3 and Figure 4.7. The peak monitored in the XPS spectra was N 1s. It is seen from the table that the untreated specimens of AISI 1018 and AISI 1045 steels contained traces of nitrogen at the near surface region, but at depths below 300 nm, nitrogen peaks were no longer visible. Tang *et al.* [69] attributed this to active radicals in steel reacting with nitrogen in air.

The nitrogen concentration profiles shown in Figure 4.7 have been plotted on a depth scale based on a sputtering rate of 0.050 nm/s obtained from a Fe reference under similar conditions [73]. The actual depth of each XPS analysis is dependent on the etch-rate of the ion gun which, in turn, depends on the material being etched at any given time. Plasma treated AISI 1045 steel had the highest atomic concentration of nitrogen near the surface but showed a steep decline after a depth of ~50 nm to concentrations lower than that of treated AISI 1018. The nitrogen concentration of plasma treated AISI 1018 steel remained higher than that of its untreated counterpart all through the depths measured in this study. The concentration declined steadily after a depth of ~50 nm, but not as steep as that seen in AISI 1045. Nitrogen ions were implanted to a greater depth in AISI 1018 than in AISI 1045 steel. Because the total dose of implanted nitrogen at the near surface of AISI 1045 steel is distributed over a smaller depth, we have a higher concentration.

Table 4.3. Amount of nitrogen (in at.%) present at various depths from the surface of tested steels before and after plasma treatment.

Depth	AISI 1018 (at.% N)		AISI 1045 (at.% N)	
(nm)	UT	T-2 h	UT	T-2 h
0	3.51	5.62	3.83	11.20
10	6.65	10.68	3.68	13.69
20	6.01	8.66	3.41	13.07
30	4.68	11.23	3.95	12.53
40	4.53	10.39	3.86	11.63
50	3.77	11.25	4.35	10.07
300	1.34	9.53	2.44	7.92
450	0.93	6.26	2.22	5.10
600	1.07	5.52	1.65	4.21
900	0.2	4.01	1.78	2.17
1200	0.2	2.72	0.87	0.54

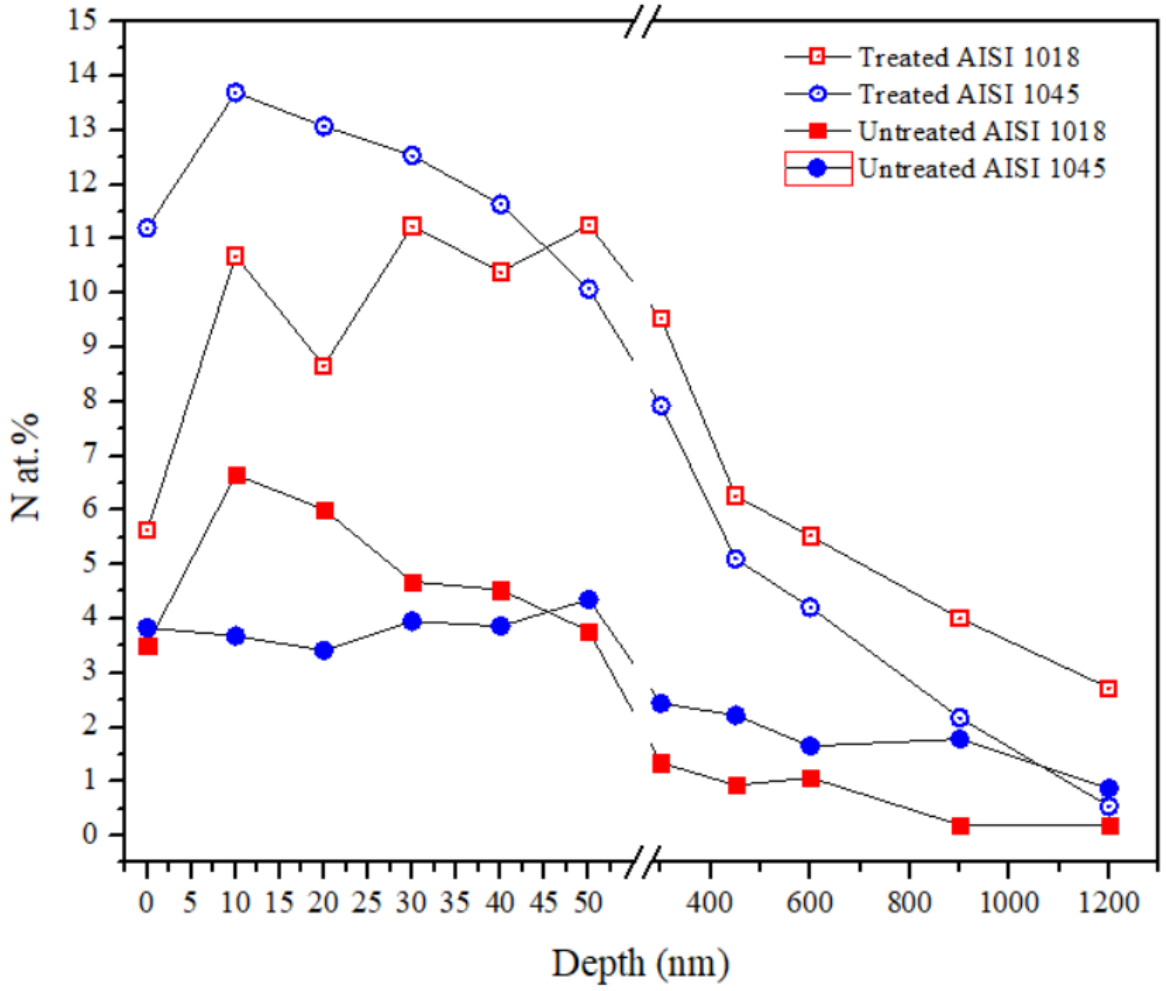

Figure 4.7. Concentration of nitrogen vs. depth for different specimens.

There appears to be fairly good correlation between the nanohardness profiles of Figures 4.5 and 4.6 to the nitrogen concentration profiles obtained by XPS (Figure 4.7). At the first few nanometers from the surface, AISI 1045 steel shows a higher concentration of nitrogen than AISI 1018 steel which corresponds to a higher increase in hardness. Deeper into the specimens, there is a steep drop in concentration of nitrogen for AISI 1045 steel below that of AISI 1018 steel. This translates to higher hardness deeper in the specimen for AISI 1018 steel. Results reported by Ochoa *et al.* [10] showed a linear proportionality between hardness and implanted nitrogen concentration.

The interaction between the implanted nitrogen atoms and the neighbouring atoms of the matrix is manifested as an energy shift of the binding energies associated with the core-levels electrons

of implanted atoms. The XPS spectra reflect the local influence of the neighbouring host atoms on the trapped nitrogen. As discussed in Chapter 2 (Section 2.3.2), after a few collisions, the projectile occupies an interstitial site in the α-iron (bcc) host crystal, causing local stress related to atom size misfiting [74], [75]. This stress causes the binding energy (BE) of nitrogen to change.

The sizes of tetrahedral and the octahedral interstitial sites in α-iron are 0.291R and 0.155R, respectively, where R (= 0.124 nm) is the atomic radius of α-Fe (bcc). The covalent radius of nitrogen is 0.071 nm. The ratios of covalent radius of nitrogen to those of tetrahedral and octahedral sites are 1.97 and 3.56, respectively. Therefore, lattice strains will be imposed on Fe atoms surrounding the implanted nitrogen. As such, the binding energy of N 1s electrons is lowered as shown in Figure 4.8. The effect is more pronounced in AISI 1045 than AISI 1018 because there is a higher concentration of implanted nitrogen ions in AISI 1045. Similar results have been reported for implanted noble gases in AISI 4140 steel by Ochao *et al*. [14]. The extent of chemical shift depends on the bombardment energy and the type of ion being implanted [76].

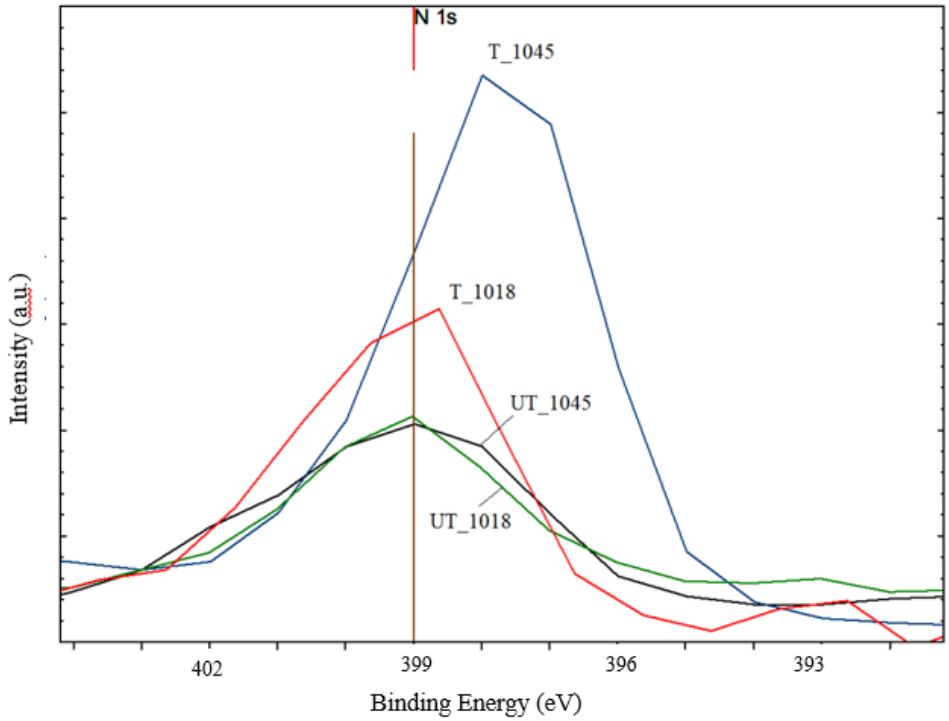

Figure 4.8. Chemical shift of nitrogen (N 1s) binding energy for treated and untreated AISI 1018 and AISI 1045 steel.

4.5 XRD

The effect of PIII treatment on the microstructure of AISI 1018 and AISI 1045 steels was investigated by XRD measurement. Figure 4.9 shows the X-ray diffraction patterns obtained for as-received (untreated) and PIII treated specimens of AISI 1018 and AISI 1045 steels. The two peaks at 2θ = 68.9° and 106.2° represent the ferrite phase in plain carbon steel [15]. After nitrogen implantation, no new peak was seen. This indicates that no compounds of Fe-N were formed due to the PIII process as expected. Also, there was no significant shift in peak in the treated specimen compared to the untreated for both AISI 1018 and AISI 1045 steels. The penetration depth of the X-ray beam is in the scale of μm, whereas the depth of implanted nitrogen is in the range of 50 nm. The X-ray technique called grazing-incidence small angle X-ray scattering is usually applied for investigating samples with nanoscale patterns on the surface. The PANalytical Empyrean X-ray diffractometer used in this study is not equipped with this capability.

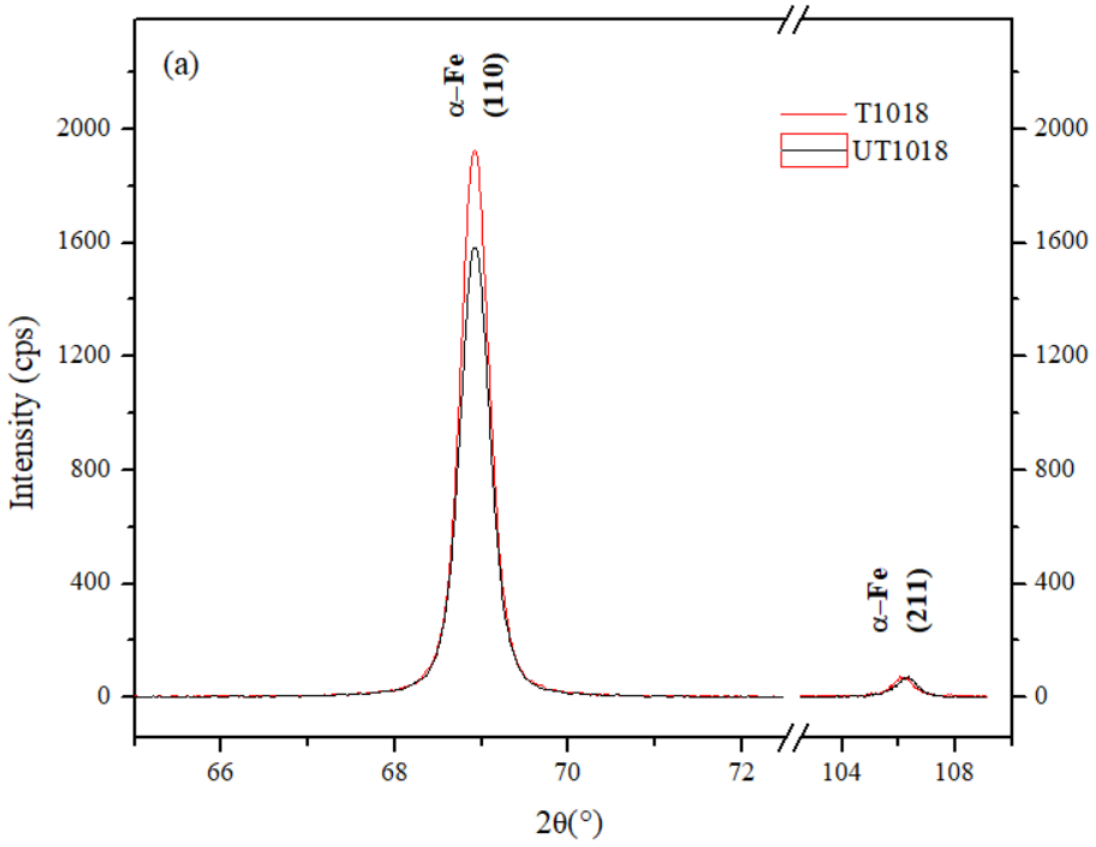

Figure 4.9. X-ray diffraction patterns obtained from untreated and treated specimens of: (a) AISI 1018 steel and (b) AISI 1045 steel.

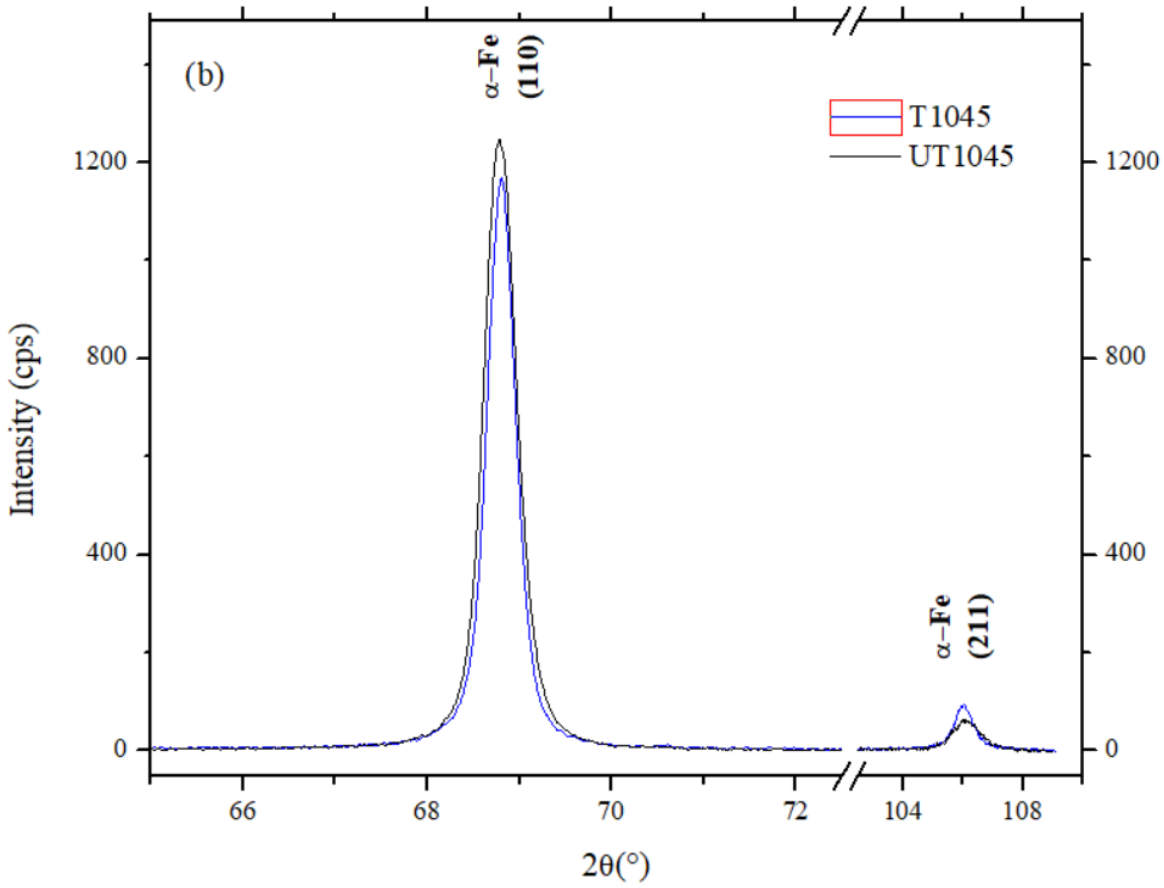

Figure 4.9. Continued.

A close look at the peaks associated with the (110) planes in AISI 1018 peaks shows that the implanted specimen has a higher intensity than that of the untreated specimen while the (211) peak intensities for the treated and untreated specimens remain practically the same. For the AISI 1045 specimen, the (110) peak intensity of the treated sample is lower than that of the untreated specimen. The intensity of a peak depends on the elemental composition of the sample and its preparation process. For polycrystalline solid specimens like the ones used in this study, different specimen grain orientation will give different intensities.

4.6 Fatigue test

A cantilever-type rotating bending fatigue machine operating at a frequency of 120 Hz at room temperature was used to evaluate the effect of PIII treatment on the fatigue resistance of AISI 1018 and AISI 1045 steels. Figures 4.10 and 4.11 show the plots of stress amplitude (σ_a) vs number of cycles to failure (N_f), i.e., *S-N* curves, obtained for untreated and treated AISI 1018 and AISI 1045 steels, respectively. The fatigue limit, determined by staircase method, remains the same at 344 ± 10 MPa before and after nitrogen implantation for AISI 1018 specimens. For AISI 1045 steel, there is an increase in fatigue strength from 402 ± 12 MPa for untreated specimens to 429 ± 9 MPa for the PIII treated specimens. The improvement in fatigue strength is due to the formation of the hardened surface layer and favorable compressive residual stress at the nitrogen rich surface layer [30,31]. The solid solution effect of implanted nitrogen induces coherent distortion and expansion of the matrix, causing hardening and compressive residual stress distribution in the implanted layer. The residual stresses on the surface become more significant as hardness increases [78]–[80].

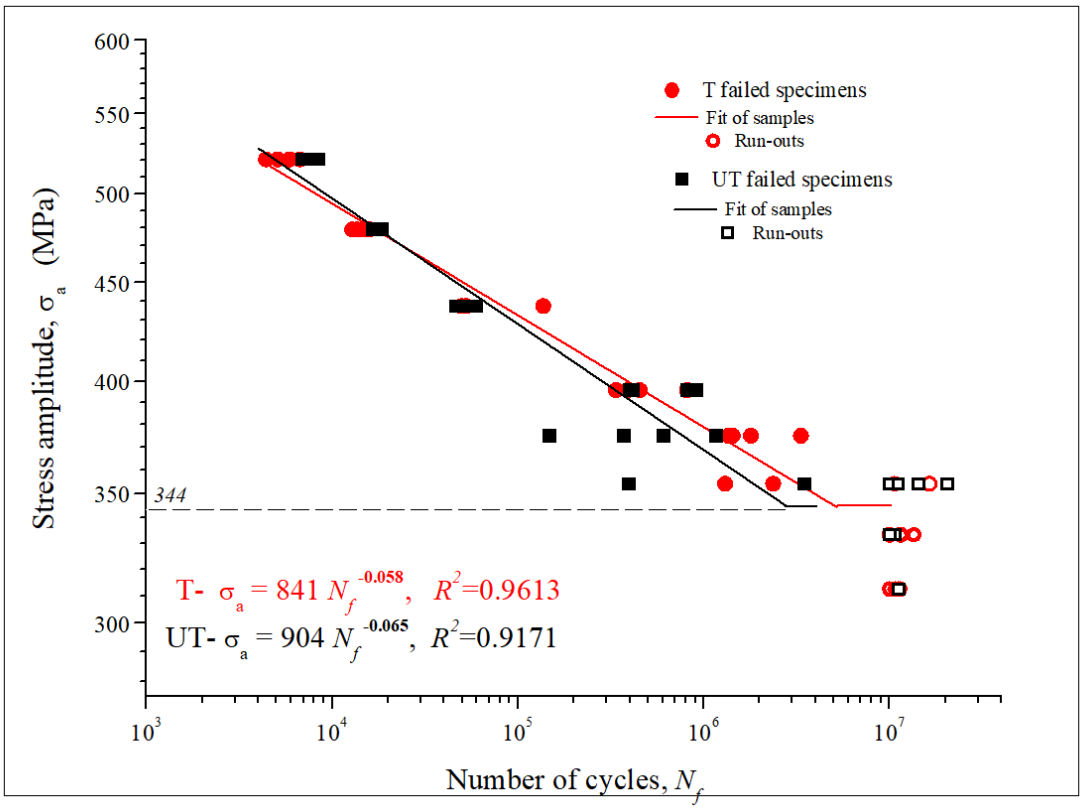

Figure 4.10. Fatigue curves obtained for plasma treated and untreated AISI 1018 steel.

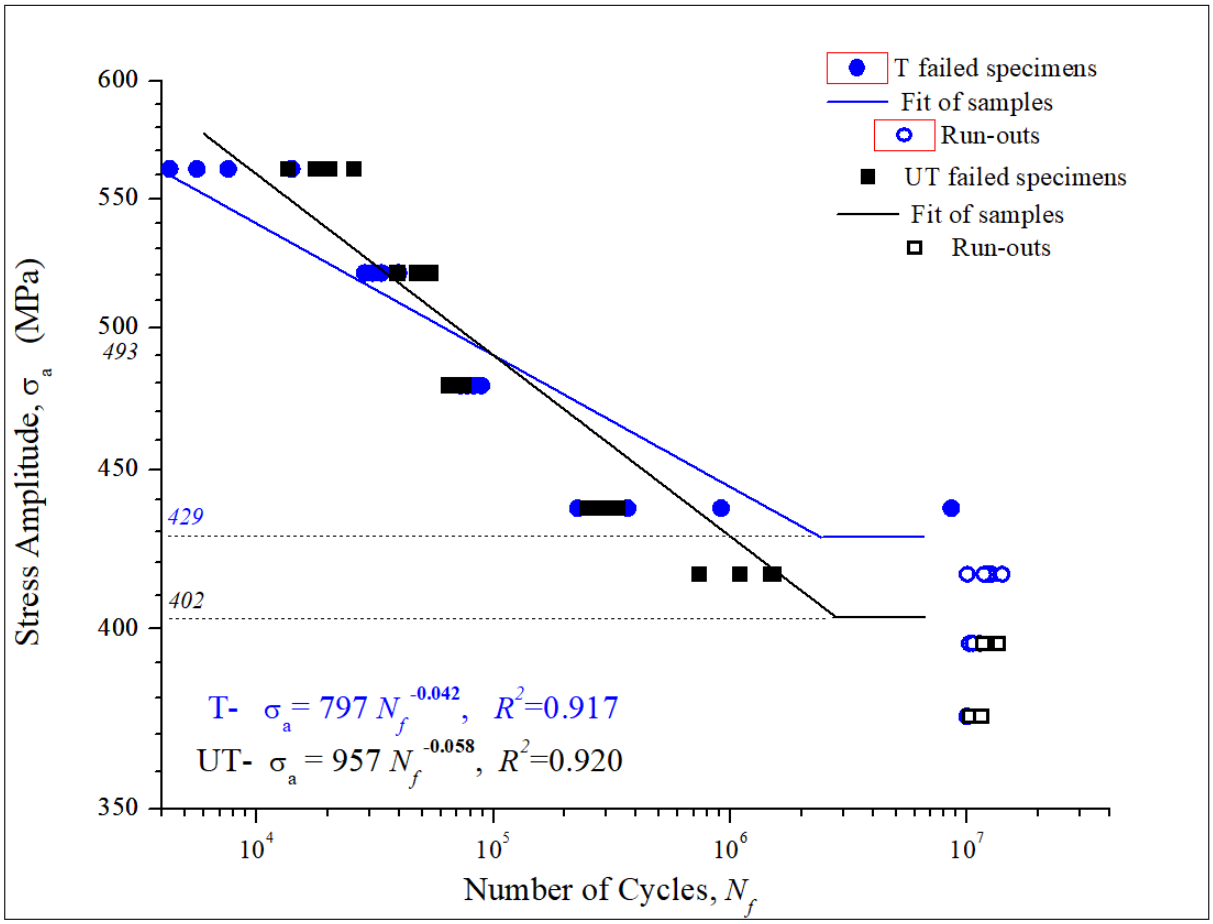

Figure 4.11. Fatigue curves obtained for plasma treated and untreated AISI 1045 steel.

Generally, S-N curves can be expressed by a Basquin-type relationship as shown in equation (4.1) [81].

$$\sigma_a = AN_f^b \tag{4.1}$$

where *A* is the fatigue strength coefficient and *b* the fatigue strength exponent. The values of *A* and *b* are obtained from regression analysis of the S-N data is summarized in Table 4.4. The test run-outs (data from unfailed specimens) were excluded from the regression analysis [82].
The fatigue strength exponent *b* is dependent on many factors and for unnotched parts, it could vary from about -0.05 to -0.12 for most metals [83]. A smaller *b* results in a longer fatigue life. The improvement in fatigue resistance after nitrogen implantation is dependent on the load applied. The effect of the stress amplitude on fatigue resistance is clearly visible on the S-N (Wohler) plots (Figures 4.10 and 4.11).

Table 4.4. Fatigue properties of untreated and plasma treated AISI 1018 and AISI 1045 specimens.

Specimens	**Fatigue strength coefficient, *A* (MPa)**	**Fatigue strength exponent, *b***	**Fatigue strength (MPa)**
AISI 1018(UT)	904	-0.065	344
AISI 1018 (T-2 h)	841	-0.058	344
AISI 1045 (UT)	957	-0.058	402
AISI 1045 (T-2 h)	797	-0.042	429

There are two regions of fatigue behavior for the PIII treated specimen compared to the untreated specimen, namely, the high-cycle fracture domain (HCFD) and the low-cycle fracture domain (LCFD).

In the HCFD ($> 10^5$ cycles), the effect of nitrogen implantation is positive. There is an increase in fatigue life compared to the untreated specimen. The process of fatigue initiation usually starts from a free surface following the intrusion and extrusion process produced by successive slip of two intersecting slip planes [21]. Crack initiation could also arise from an internal inclusion [10], [69], [84], [85]. After PIII treatment mechanism of intrusion and extrusion is impeded by the increased hardness and compressive residual stress of the surface layer. As a result, it takes a longer time for cracks to initiate and it is easier for cracks to start from internal defects.

In contrast, nitrogen implantation decreased fatigue life in the LCFD ($< 10^5$ cycles) [4], [7], [28], [78], [86]. The large stress amplitude applied in the LCFD produces significant cyclic deformations which relaxes the residual stresses produced by the PIII process [9], [84]. Also, fatigue resistance in the LCFD decreases because of a higher sensitivity to overload compared to the untreated specimen. Sensitivity to overload of the PIII treated specimen is higher because the difference in rigidity between the bulk ductile and surface hardened layer is larger [9], [79], [86], [87].

4.7 Fractography

Scanning electron micrography (SEM) was used to investigate the surfaces of fractured specimens of untreated and PIII treated AISI 1018 and AISI 1045 steels. Figure 4.12 shows a typical fracture surface of an untreated AISI 1018 steel specimen which failed after 59300 cycles. Two sites of crack origin were identified, highlighted as A and B. Zooming in on these sites show that cracks initiated from inclusions at the surface. A similar observation is found in PIII treated AISI 1018 specimens (Figure 4.13), as well as PIII treated and untreated AISI 1045 specimens (Figure 4.14).

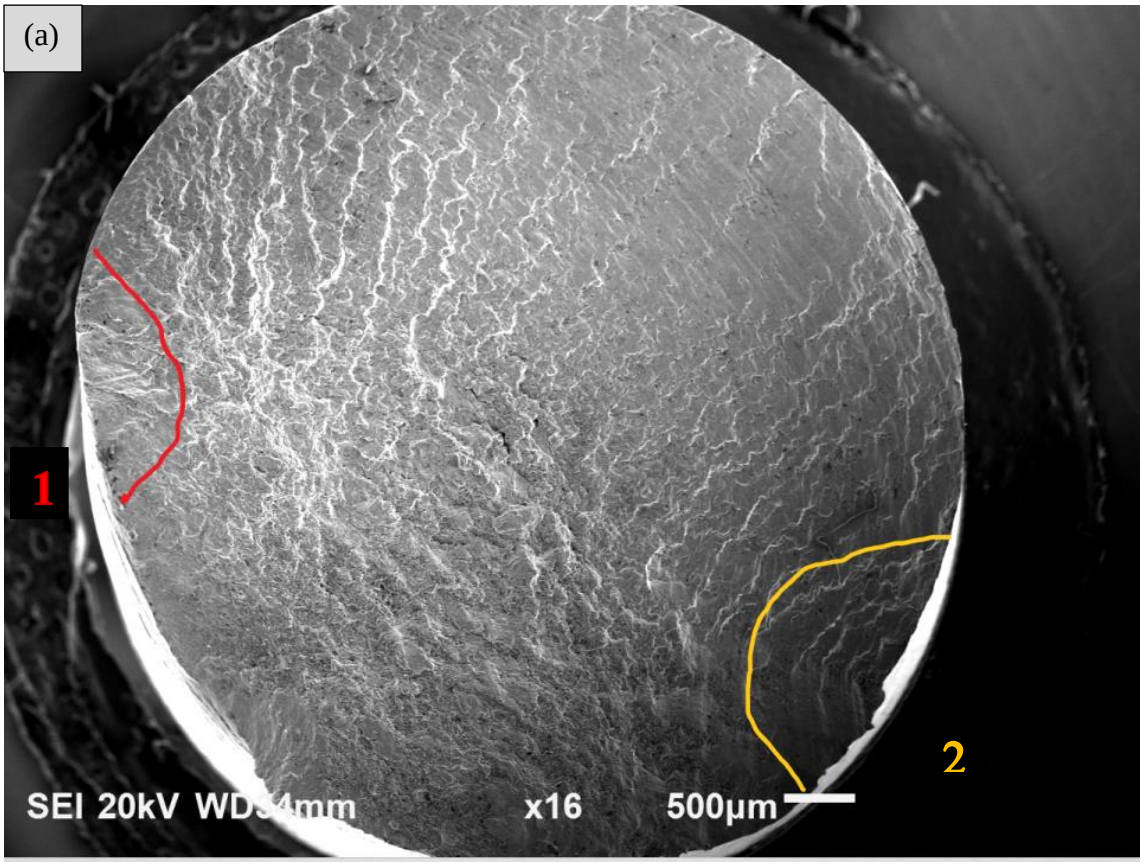

Figure 4.12. Fractographs of: (a) an untreated AISI 1018 specimen showing crack initiation sites 1 and 2, (b) magnified view of site 1, and (c) magnified view of site 2.

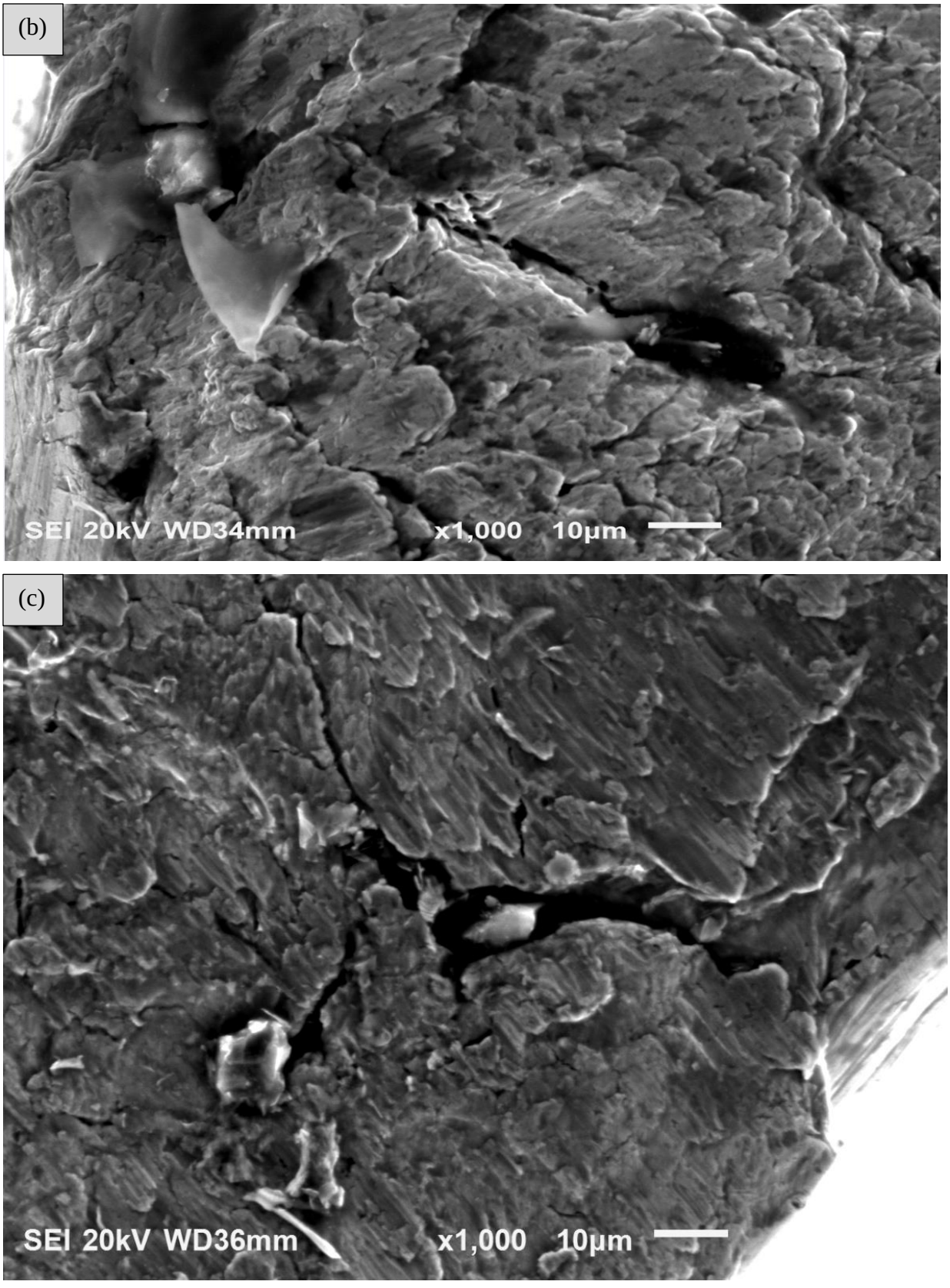

Figure 4.12. Coninued.

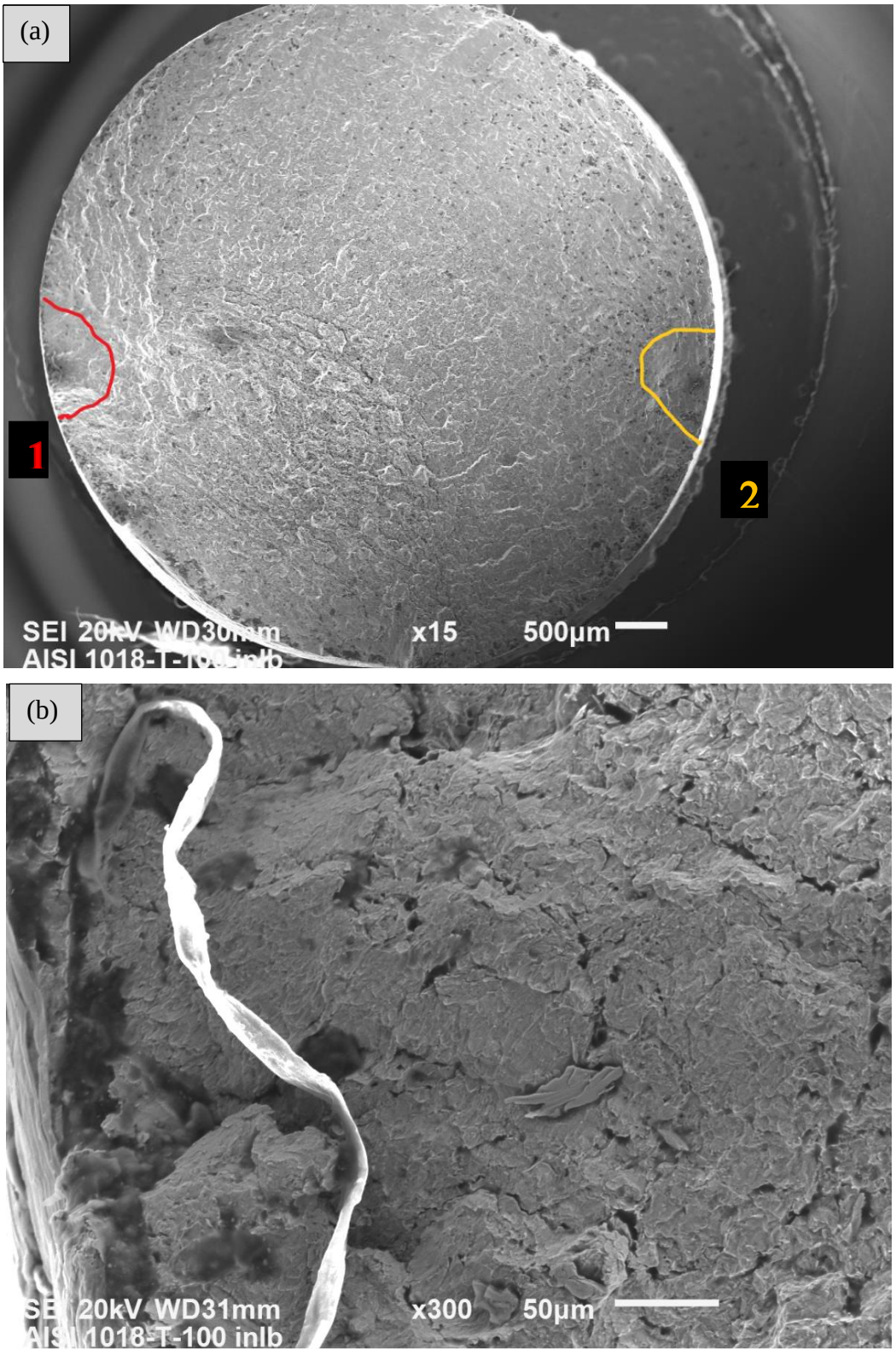

Figure 4.13. Fractographs of: (a) PIII treated AISI 1018 specimen showing crack initiation areas 1 and 2, (b) magnified view of site 1, and (c) magnified view of site 2.

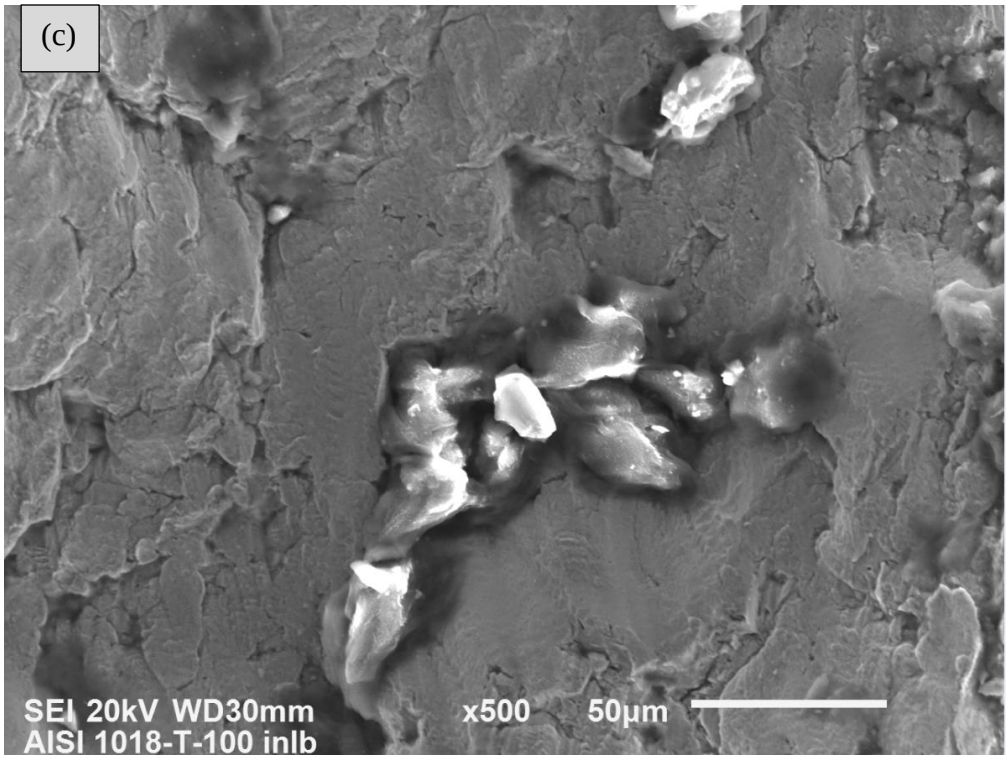

Figure 4.13. continued.

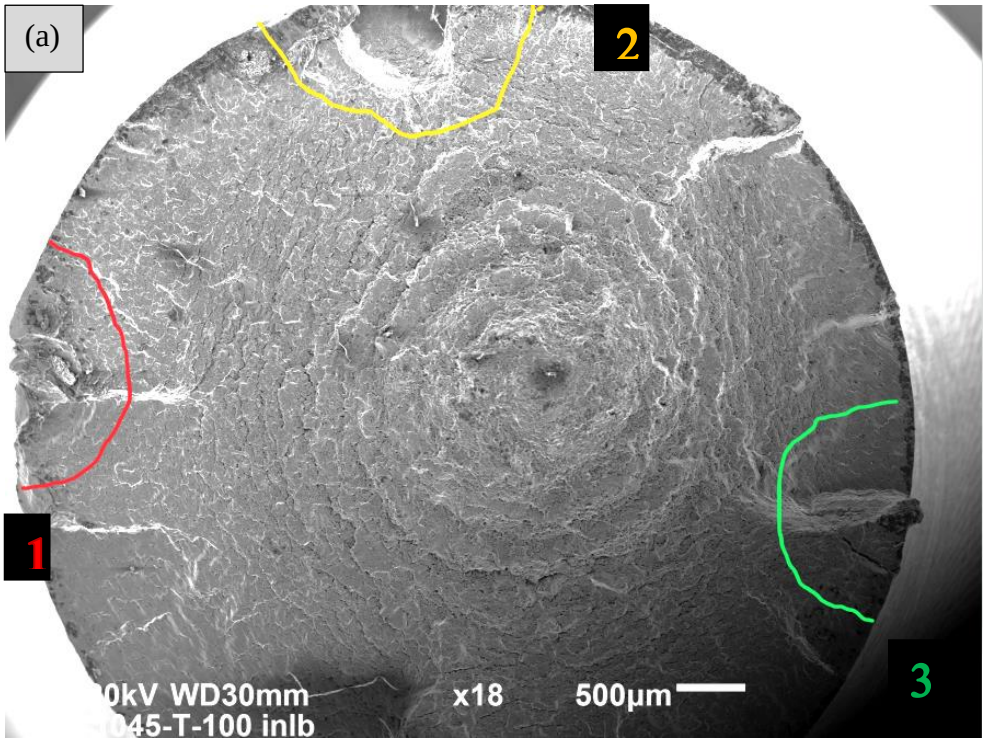

Figure 4.14. (a) Fractograph of PIII treated AISI 1045 specimen showing crack initiation sites 1, 2 and 3, (b) enlarged view of site 1, (c) enlarged view of site 2, and (d) magnified view of site 3.

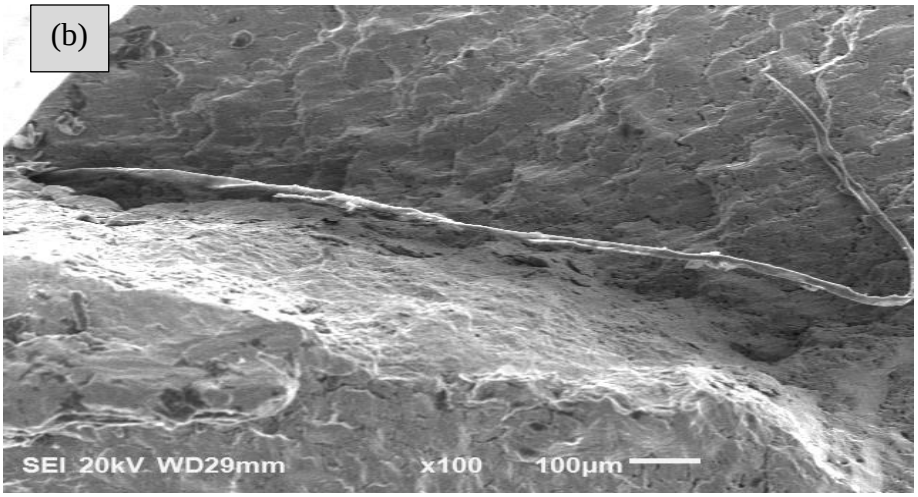

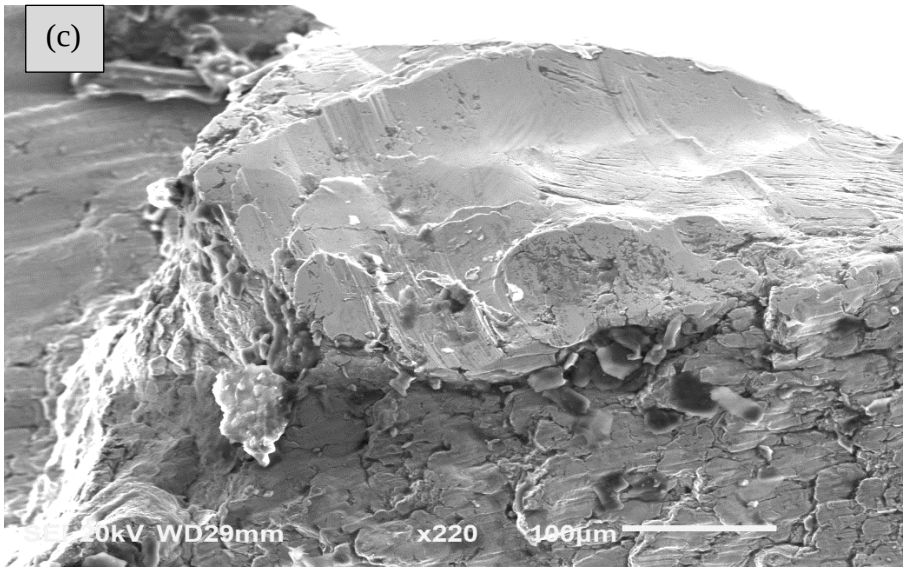

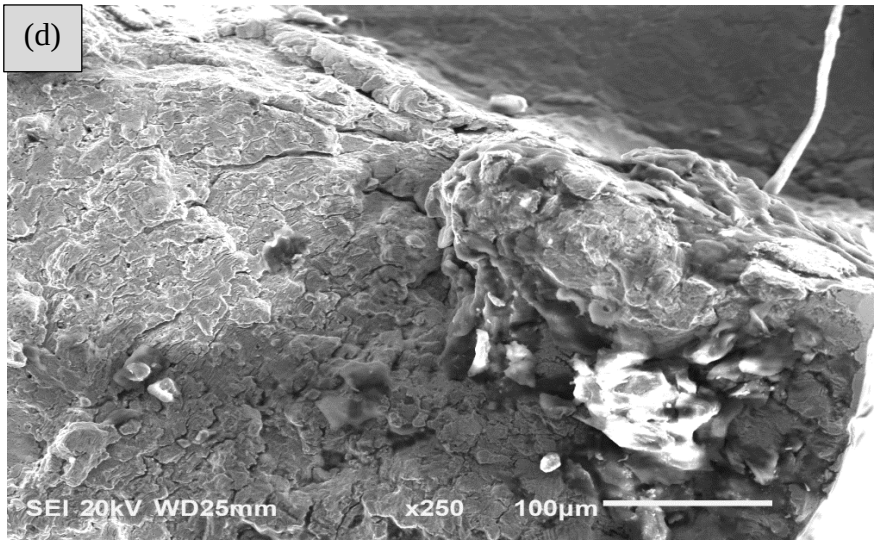

Figure 4.14. continued.

The inclusions found at sites of crack initiation were of two types; cubic particles with a length of about 10 μm and long string-like particles typically know as stringers in steel [23], [88], [89]. Figure 4.15 shows these inclusions. An important feature of non-metallic inclusions is its decohesion with the matrix material, which is most likely a result of a different thermal expansion properties to that of steel [8].

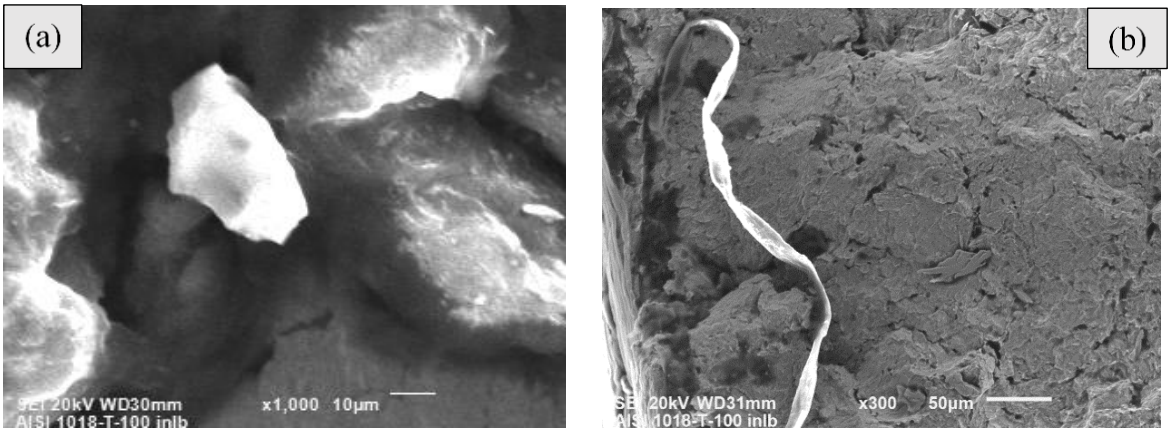

Figure 4.15. Two types of inclusions found at crack initiation sites. (a) cubic particles and (b) stringers.

CHAPTER 5

CONCLUSIONS AND RECOMMENDATIONS

5.1 Conclusions

This study investigated the effect of nitrogen implantation on the hardness and fatigue properties of AISI 1018 and AISI 1045 steel. Based on the analysis of the results obtained in Chapter 4, the following conclusions can be made.

(1) Nitrogen ions got implanted into greater depths from the surface of AISI 1018 compared to AISI 1045. The higher carbon content of AISI 1045 appeared to have shortened the mean free path of implanted nitrogen.

(2) The implantation of nitrogen into both grades of steels increased its surface hardness; however, after 2 h of PIII treatment, there was a saturation and no further increase in hardness was observed.

(3) The implantation of nitrogen ions led to a larger increase in hardness of AISI 1045 compared to AISI 1018. This was a resultant of implanted nitrogen being concentrated in a smaller layer from the surface.

(4) The fatigue limit of AISI 1018 steel remained the same after nitrogen implantation whereas that of AISI 1045 was increased from 402 MPa to 429 MPa.

(5) Two distinct regions characterized the fatigue behavior of both grades of steel after nitrogen ion implantation, namely: the high cycle fracture domain (HCFD) and the low cycle fracture domain (LCFD). In the HCFD, fatigue life of both steels was increased while in the LCFD, there was a decrease in fatigue life. This effect was more pronounced in AISI 1045 steel compared to AISI 1018 steel.

(6) Cracks initiated from the surface of fractured specimen. Inclusions at the surface were found to be the nucleation sites.

5.2 Recommendations

(1) The initial plan of this study also had AISI 1090 steel as a specimen. It could not be sourced nearby, hence, it was removed from the study. It would be great to know if a steel with high carbon content would further limit the depth of penetration of implanted nitrogen ions.

(2) Investigating the effect of PIII treatment time on the depth of implantation might help further explain the decrease in hardness observed at longer treatment time.

(3) The XPS analysis was limited to 4 minutes of sputtering which did not get to the bulk of treated AISI 1018 specimens. It is suggested that further sputtering be done to get the depth at which the concentration of nitrogen is same as the untreated specimen.

(4) After PIII treatment, coloration of the specimens was observed, with this being more for AISI 1045 specimens. An investigation into the cause of this and its possible effect on mechanical properties of the steel is suggested.

REFERENCES

[1] S. Jin, S. Kim, Y. Lee, Y. Kwon, and Y. Kim, “Effect of various heat and surface treatment conditions on the fatigue behavior of SKD11 steel,” *Met. Mater. Int.*, vol. 15, no. 6, pp. 917–923, 2009.

[2] C. Kanchanomai and W. Limtrakarn, “Effect of residual stress on fatigue failure of carbonitrided low-carbon steel,” *J. Mater. Eng. Perform.*, vol. 17, no. 6, pp. 879–887, 2008.

[3] D. Jeddi, H. Sidhom, D. Ghiglione, and H.-P. Lieurade, “Role of the cyclic stability of retained austenite in fatigue performance of carburized 14NiCr11 Steel,” *J. Mater. Eng. Perform.*, vol. 14, no. 1, pp. 37–49, 2005.

[4] M. Torres, “An evaluation of shot peening, residual stress and stress relaxation on the fatigue life of AISI 4340 steel,” *Int. J. Fatigue*, vol. 24, no. 8, pp. 877–886, 2002.

[5] American Society For Testing and Materials, *Handbook of fatigue*. Philadelphia, Pa.: ASTM Special Technical Publication 566, 2014.

[6] J. R. Conrad, J. L. Radtke, R. A. Dodd, F. J. Worzala, and N. C. Tran, “Plasma source ion-implantation technique for surface modification of materials,” *J. Appl. Phys.*, vol. 62, no. 11, pp. 4591–4596, 1987.

[7] K. Hussain, “Influence of gas nitriding on fatigue resistance of maraging steel,” *Int. J. Fatigue*, vol. 21, no. 2, pp. 163–168, 1999.

[8] K. Genel, M. Demirkol, and M. Çapa, “Effect of ion nitriding on fatigue behaviour of AISI 4140 steel,” *Mater. Sci. Eng. A*, vol. 279, no. 1–2, pp. 207–216, 2000.

[9] J. D. Costa, J. M. Ferreira, and A. L. Ramalho, “Fatigue and fretting fatigue of ion-nitrated 34CrNiMo6 steel,” *Theor. Appl. Fract. Mech.*, vol. 35, no. 1, pp. 69–79, 2001.

[10] M. A. Terres and H. Sidhom, “Fatigue life evaluation of 42CrMo4 nitrided steel by local approach: Equivalent strain-life-time,” *Mater. Des.*, vol. 33, no. 1, pp. 444–450, 2012.

[11] M. F. Ashby and D. R. H. Jones, “An introduction to microstructures, processing and design:,” in *Engineering Materials*, Second edition, Elsevier, pp. 190–193, 1998.

[12] S. Jayanti, “Plain carbon steels: classification and limitations | Metallurgy.” [Online]. Available: https://www.engineeringenotes.com/metallurgy/steel/plain-carbon-steels-classification-and-limitations-metallurgy/25621. [Accessed: 11-Oct-2020].

[13] S. Nagendhra, A. S. Rami Reddy, and G. V Preetham Kumar, “Workability study on austempered AISI 1018,” in *IOP Conference Series: Materials Science and Engineering*, 2018, vol. 376, no. 1, p. 2049 - 2050.

[14] D. Gandy, “Carbon steel handbook.” Electric Power Research Institute, Califonia, pp. 172–175, 2007.

[15] AZO Materials, “AISI 1018 mild/low carbon steel,” *AZoM.com*, 2015. [Online]. Available: http://www.yandreou.com/wp-content/uploads/2014/08/AISI-1018-Mild-Low-Carbon-Steel-PDF.pdf. [Accessed: 19-Oct-2020].

[16] MakeItFrom.com, “Hot rolled 1018 carbon steel :: MakeItFrom.com.” [Online]. Available: https://www.makeitfrom.com/material-properties/Hot-Rolled-1018-Carbon-Steel. [Accessed: 11-Sept-2020].

[17] AZO Materials, “AISI 1045 medium carbon Steel,” 2012. [Online]. Available: https://www.azom.com/article.aspx?ArticleID=6130#. [Accessed: 19-Jul-2018].

[18] MakeItFrom.com, “Hot rolled 1045 carbon steel :: MakeItFrom.com.” [Online]. Available: https://www.makeitfrom.com/material-properties/Hot-Rolled-1045-Carbon-Steel. [Accessed: 12-Sept-2020].

[19] J. A. Ewing and M. J. C. W. Humfrey, “The fracture of metals under repeated alternations of stress,” *Proc. R. Soc. London*, vol. 71, no. 467–476, pp. 79–79, 1903.

[20] J. R. Low, “The fracture of metals,” *Prog. Mater. Sci.*, vol. 12, pp. 3–96, 1963.

[21] P. Partridge, “Slip band extrusion in fatigued close packed hexagonal metals,” *Acta. Metall.*, vol. 13, no. 5, pp. 517–525, 1965.

[22] Total Material, “Fatigue of metals: part three” [Online]. Available: https://www.totalmateria.com/page.aspx?ID=CheckArticle&site=kts&NM=282. [Accessed: 12-Oct-2020].

[23] S. Kou, *Welding metallurgy*, John Wiley & Sons, Inc., Hoboken, New Jersey, Second edition, pp. 57-64, 2007.

[24] H. J. Gough, D. G. Sopwith, and J. E. Petavei, “The Behaviour of a Single Crystal of Aluminium under Alternating Torsional Stresses while Immersed in a Slow Stream of Taj Water,” *Proceedings of the Royal Society of London. Series A, Containing Papers of a Mathematical and Physical Character*, vol.135, no.827, pp. 392-411, 1932.

[25] F. Bradshaw and C. Wheeler, “The influence of gaseous environment and fatigue

frequency on the growth of fatigue cracks in some aluminum alloys," *Int. J. Fract. Mech.*, vol. 5, no. 4, pp. 255-268, 1969.

[26] P. E. Irving and C. J. Beevers, "The effect of air and vacuum environments on fatigue crack growth rates in Ti-6Al-4V," *Metall. Trans.*, vol. 5, no. 2, pp. 391–398, 1974.

[27] Curthbertson, "Fatigue limit of medium carbon steel," *Nature*, vol. 131, no. 3300. p. 140-147, 1933.

[28] C. Kanchanomai and W. Limtrakarn, "Effect of residual stress on fatigue failure of carbonitrided low-carbon steel," *J. Mater. Eng. Perform.*, vol. 17, no. 6, pp. 879–887, 2008.

[29] P. De la Cruz, M. Oden, and T. Ericsson, "Influence of plasma nitriding on fatigue strength and fracture of B-Mn steel," *Mater. Sci. Eng.*, vol. 242, pp. 181–194, 1998.

[30] W. WEIBULL, "Fatigue testing machine and equipment," *Fatigue Testing and Analysis of Results*, Elsevier, 1961, pp. 25–65.

[31] H. O. Fuchs, R. I. Stephens, and H. Saunders, "Metal fatigue in engineering (1980)," *J. Eng. Mater. Technol.*, vol. 103, no. 4, pp. 346–346, 1981.

[32] G. A. Ikechukwu, O. O. Clementina, and C. L. Onyebuchi, "Design and characterization of a fatigue testing machine," *Lect. Notes Eng. Comput. Sci.*, vol. I, pp. 23–25, 2013.

[33] ASM, "Parameters for estimating fatigue life," in *Fatigue and Fracture*, ASM International, 2018, pp. 963–979.

[34] T. Isibasi, *Prevention of fatigue and fracture of metals*, 1st edition. Tokyo: Yokendo Ltd, 1967.

[35] Y. Murakami, "Effects of small defects and nonmetallic inclusions on the fatigue strength of metals," *Key Eng. Mater.*, vol. 51–52, pp. 37–42, 1991.

[36] S. Lampman, "Introduction to surface hardening of steels," *ASM Handbook, Vol. 4, Heat Treat.*, vol. 4, pp. 259–267, 1991.

[37] C. B. Yarling, "History of industrial and commercial ion implantation 1906–1978," *J. Vac. Sci. Technol. A Vacuum, Surfaces, Film.*, vol. 18, no. 4, pp. 1746-1750, 2000.

[38] G. Dearnaley, "Adhesive and abrasive wear mechanisms in ion implanted metals," *Nucl. Instruments Methods Phys. Res. Sect. B Beam Interact. with Mater. Atoms*, vol. 7 no.8, pp. 158–165, 1985.

[39] Richard J. Adler and N. M. Albuquerque, "Ion implantation source and device," US patent

no. 4,587,430, 06-May-1986.

[40] M. John R- Conrad, “Method and apparatus for plasma source ion implantation,” US patent no. 4,764,394, 16-Aug-1988.

[41] D. Gupta, “Plasma immersion ion implantation (PIII) process-physics and technology,” *Int. J. Adv. Technol.*, vol. 2, no. 4, pp. 471–490, 2011.

[42] Boris M. Smirnov, *Elementary plasma processes*, Moscow: Mir Publishers, p. 232-40, 1981.

[43] E. Holt and R. E. Haskell, *Foundations of plasma dynamics*, Edition 1, New York: Macmillan, Newyork, 1965.

[44] N. A. Krall, A. W. Trivelpiece, and K. R. Symon, “Principles of plasma physics,” *IEEE Trans. Plasma Sci.*, vol. 2, no. 3, pp. 196–196, 1974.

[45] B. Chapman and J. L. Vossen, “Glow discharge processes: sputtering and plasma etching,” *Phys. Today*, vol. 34, no. 7, p. 62-66, 1981.

[46] M. A. Lieberman and A. J. Lichtenberg, *Discharges and materials processing principles of plasma discharges and materials*, 35th edition, Wiley-Interscience, pp. 757- 760, 1994.

[47] K.-U. Riemann, “The Bohm criterion and sheath formation,” *J. Phys. D Appl.*, vol. 24, pp. 492–518, 1991.

[48] M. A. Lieberman, “Model of plasma immersion ion implantation,” *J. Appl. Phys.*, vol. 66, no. 7, p. 2929- 2934, 1989.

[49] S. Mändl, J. Brutscher, R. Günzel, and W. Möller, “Inherent possibilities and restrictions of plasma immersion ion implantation systems,” *J. Vac. Sci. Technol. B Microelectron. Nanom. Struct.*, vol. 14, no. 4, p. 2701-2705, 1996.

[50] S. Mändl, J. Brutscher, R. Günzel, and W. Möller, “Design considerations for plasma immersion ion implantation systems,” *Nucl. Instruments Methods Phys. Res. Sect. B Beam Interact. with Mater. Atoms*, vol. 112, no. 1–4, pp. 252–254, 1996.

[51] H. Herman, “Surface mechanical properties - effects of ion implantation,” *Nucl. Instruments Methods*, vol. 182–183, no. 2, pp. 887–898, 1981.

[52] A. Tóth, M. Mohai, T. Ujvári, T. Bell, H. Dong, and I. Bertóti, “Surface chemical and nanomechanical aspects of air PIII-treated Ti and Ti-alloy,” *Surface and Coatings Technology*, vol. 186, no. 1-2. pp. 248-254, 2004.

[53] R. Hutchings and W. C. Oliver, “A study of the improved wear performance of nitrogen-

implanted Ti-6Al-4V," *Wear*, vol. 92, no. 1, pp. 143–153, 1983.

[54] A. Çelik, S. Karadeniz, "Improvement of the fatigue strength of AISI 4140 steel by an ion nitriding process," *Surf. Coatings Technol.*, vol. 72, no. 3, pp. 169–173, 1995.

[55] Y. Hashiguchi, T. Ohtsubo, and K. Sugiyama, "Depth profile of nitrogen implanted in cold-rolled steel.," *J. Met. Finish. Soc. Japan*, vol. 39, no. 10, pp. 610–614, 1988.

[56] L. L. G. da Silva, M. Ueda, C. B. Mello, E. N. Codaro, and C. M. Lepienski, "Effects of the high temperature plasma immersion ion implantation (PIII) of nitrogen in AISI H13 steel," *J. Mater. Sci.*, vol. 43, no. 17, pp. 5989–5997, 2008.

[57] K. Obrtlík, Y. Jirásková, J. Man, and J. Polák, "Effect of surface carbonitriding by plasma immersion ion implantation on the fatigue behaviour of 316L austenitic stainless steel," *WIT Trans. Eng. Sci.*, vol. 49, p. 10-12, 2005.

[58] H. Liu, B. Tang, L. Wang, X. Wang, and B. Jiang, "Fatigue life and mechanical behaviors of bearing steel by nitrogen plasma immersion ion implantation," *Surf. Coatings Technol.*, vol. 201, no. 9–11, pp. 5273–5277, 2007.

[59] J. A. Casey, M. Kempkes, M. P. J. Gaudreau, T. J. Hawkey, M. A. Kempkes, and J. M. Mulvaney, "Solid state modulators for PIII applications," J*ournal of Vacuum Science & Technology B: Microelectronics and Nanometer Structures*, vol.17, no. 2, pp. 888-891, 1999.

[60] R. Marcel, "The promise of nitrogen plasma implanted gallium arsenide for band gap engineering," (MSc Thesis), Department of Physics and Engineering Physics, University of Saskatchewan, 2008.

[61] Hong Li, "Measurements of electron energy distribution function and neutral gas temperature in an inductively coupled plasma," (MSc Thesis), Department of Physics and Engineering Physics, University of Saskatchewan, 2006.

[62] M. Tuszewski and J. A. Tobin, "The accuracy of langmuir probe ion density measurements in low-frequency RF discharges," *Plasma Sources Sci. Technol.*, vol. 5, no. 4, pp. 640–647, 1996.

[63] M. Nastasi, J. W. Mayer, and Y. Wang, *Ion beam analysis: Fundamentals and applications*. CRC Press, 2014.

[64] ASTM E384-17, "Standard test method for microindentation hardness of materials," *ASTM International*, West Conshohocken, PA, pp. 1–40, 2017.

[65] ASTM E2546-07, “Standard practice for instrumented indentation testing,” *ASTM International*. West Conshohocken, PA, p. 23-35, 2007.

[66] W. C. Oliver and G. M. Pharr, “An improved technique for determining hardness and elastic modulus using load and displacement sensing indentation experiments,” *J. Mater. Res.*, vol. 7, no. 6, pp. 1564–1583, 1992.

[67] T. Wright and T. F. Page, “Nanoindentation and microindentation studies of hard carbon on 304 stainless steel,” *Surf. Coatings Technol.*, vol. 54–55, pp. 557–562, 1992.

[68] M. C. Kim, “Surface modification for hydrophilic property of stainless steel treated by atmospheric-pressure plasma jet,” *Surf. Coatings Technol.*, vol. 171, pp. 312–316, 2003.

[69] S. Y. Sirin, K. Sirin, and E. Kaluc, “Effect of the ion nitriding surface hardening process on fatigue behavior of AISI 4340 steel,” *Mater. Charact.*, vol. 59, no. 4, pp. 351–358, 2008.

[70] S. Tang, O. J. Kwon, N. Lu, and H. S. Choi, “Surface characteristics of AISI 304L stainless steel after an atmospheric pressure plasma treatment,” *Surf. Coatings Technol.*, vol. 195, no. 2–3, pp. 298–306, 2004.

[71] M. Suzuki, A. Kishida, Y. Ikada, and H. Iwata, “Graft copolymerization of acrylamide onto a polyethylene surface pretreated with a glow discharge,” *Macromolecules*, vol. 19, no. 7, pp. 1804–1808, 1986.

[72] M. Takeda, T. Onishi, S. Nakakubo, and S. Fujimoto, “Physical properties of iron-oxide scales on Si-containing steels at high temperature,” *Mater. Trans.*, vol. 50, no. 9, pp. 2242–2246, 2009.

[73] H. L. Ju, “The study on magnetron sputtering rate of metal targets,” *Advanced Materials Research*, 2014, vol. 926–930, pp. 371–374.

[74] J. D. Kamminga, T. H. De Keijser, R. Delhez, and E. J. Mittemeijer, “A model for stress in thin layers induced by misfitting particles: An origin for growth stress,” *Thin Solid Films*, vol. 317, no. 1–2, pp. 169–172, 1998.

[75] J. D. Kamminga, T. H. De Keijser, E. J. Mittemeijer, and R. Delhez, “New methods for diffraction stress measurement: A critical evaluation of new and existing methods,” *J. Appl. Crystallogr.*, vol. 33, no. 4, pp. 1059–1066, 2000.

[76] E. A. Ochoa., “The effect of noble gas bombarding on nitrogen diffusion in steel,” *Mater. Chem. Phys.*, vol. 143, no. 1, pp. 116–123, 2013.

[77] B.-Y. Jeong and M.-H. Kim, “Effects of the process parameters on the layer formation behavior of plasma nitrided steels,” *Surf. Coatings Technol.*, vol. 141, no. 2–3, pp. 182–186, 2001.

[78] A. Çelik, I. Efeoğlu, and G. Sakar, “Microstructure and structural behavior of ion-nitrided AISI 8620 steel,” *Mater. Charact.*, vol. 46, no. 1, pp. 39–44, 2001.

[79] T. Morita, H. Takahashi, M. Shimizu, and K. Kawasaki, “Factors controlling the fatigue strength of nitrided titanium,” *Fatigue Fract. Eng. Mater. Struct.*, vol. 20, no. 1, pp. 85–92, 1997.

[80] N. Ishikawa, T. Shiraga, K. Sato, M. Ishiguro, H. Kabasawa, and Y. Kuwahara, “Effects of nitriding temperature on gas nitriding property of steels for nitriding,” *J. Iron Steel Inst. Japan*, vol. 82, no. 2, pp. 164–169, 1996.

[81] N. Dowling and S. Thangjitham, “An overview and discussion of basic methodology for fatigue,” in *Fatigue and Fracture Mechanics: 31st Volume*, 100 Barr Harbor Drive, PO Box C700, West Conshohocken, PA 19428-2959: ASTM International, 2008, pp. 33–34.

[82] H. Chen, G. Y. Grondin, and R. G. Driver, “Characterization of fatigue properties of ASTM A709 high performance steel,” *J. Constr. Steel Res.*, vol. 63, no. 6, pp. 838–848, 2007.

[83] J. Wan, “Cyclic deformation and fatigue behaviour of ion-nitrided steel,” *Int. J. Fatigue*, vol. 17, no. 1, pp. 15–24, 1995.

[84] F. Ashrafizadeh, “Influence of plasma and gas nitriding on fatigue resistance of plain carbon (Ck45) steel,” *Surf. Coatings Technol.*, vol. 174–175, pp. 1196–1200, 2003.

[85] U. N. Puntambekar, G. S. Grewal, P. B. Joshi, and P. Sampathkumaran, “Effect of plasma nitriding treatment on fatigue life of En-24 steel,” *Int. J. Innov. Res. Sci. Eng. Technol.*, vol. 2, no. 8, pp. 4069–4079, 2013.

[86] M. A. Terres and H. Sidhom, “Influence de la nitruration gazeuse sur la tenue en fatigue flexion des composants nitrurés en acier 42CrMo4,” *Matériaux Tech.*, vol. 98, no. 2, pp. 171–184, 2010.

[87] N. Limodin and Y. Verreman, “Fatigue strength improvement of a 4140 steel by gas nitriding: Influence of notch severity,” *Mater. Sci. Eng. A*, vol. 435–436, pp. 460–467, 2006.

[88] S. Shen, “The effects of heat input on tensile and fatique properties of submerged arc

weled ASTM A709 grade 50 steel (M.Sc Thesis)," Mechanical Engineering Department, University of Saskatchewan, 2011.

[89] B. Boardman, "Fatigue resistance of steels," *Prop. Sel. Irons, Steels, High Perform. Alloy.*, vol. 1, pp. 673–688, 1990.

APPENDIX A

COPYRIGHT PERMISSIONS

Chapter 2, Figures 2.1

Order Number: 1058196
Order Date: 25 Aug 2020

Payment Information

Emmanuel Awoyele
eoa338@usask.ca
Payment method: Invoice

Billing Address:
Emmanuel Awoyele
University of Saskatchewan
1217 15th street,
1217 15th street,
Saskatoon, SK S7N0R6
Canada

+1 (306) 715-4354
eoa338@usask.ca

Customer Location:
Emmanuel Awoyele
University of Saskatchewan
1217 15th street,
1217 15th street,
Saskatoon, SK S7N0R6
Canada

Order Details

1. Atlas of fatigue curves

Billing Status: Open

Order license ID	1058196-1
Order detail status	Completed
ISBN-13	9780871702142
Type of use	Republish in a thesis/dissertation
Publisher	AMERICAN SOCIETY FOR METALS,
Portion	Chart/graph/table/figure

0.00 CAD
Republication Permission

LICENSED CONTENT

Publication Title	Atlas of fatigue curves	**Country**	United States of America
Author/Editor	BOYER, HOWARD E.,AMERICAN SOCIETY FOR METALS.	**Rightsholder**	ASM International
		Publication Type	Book
Date	12/31/1984		

REUSE CONTENT DETAILS

Title, description or numeric reference of the portion(s)	Figure 1-2; S-N curves typical for medium strength steels	**Title of the article/chapter the portion is from**	N/A
Editor of portion(s)	N/A	**Author of portion(s)**	BOYER, HOWARD E.; AMERICAN SOCIETY FOR METALS.
Volume of serial or monograph	N/A		
Page or page range of portion	pg 28	**Issue, if republishing an article from a serial**	N/A
		Publication date of portion	1984-12-31

PUBLISHER SPECIAL TERMS AND CONDITIONS

Please cite the ASM source as a reference.

CCC Republication Terms and Conditions

1. Description of Service; Defined Terms. This Republication License enables the User to obtain licenses for republication of one or more copyrighted works as described in detail on the relevant Order Confirmation (the "Work(s)"). Copyright Clearance Center, Inc. ("CCC") grants licenses through the Service on behalf of the rightsholder identified on the Order Confirmation (the "Rightsholder"). "Republication", as used herein, generally means the inclusion of a Work, in whole or in part, in a new work or works, also as described on the Order Confirmation. "User", as used herein, means the person or entity making such republication.

2. The terms set forth in the relevant Order Confirmation, and any terms set by the Rightsholder with respect to a particular Work, govern the terms of use of Works in connection with the Service. By using the Service, the person transacting for a republication license on behalf of the User represents and warrants that he/she/it (a) has been duly authorized by the User to accept, and hereby does accept, all such terms and conditions on behalf of User, and (b) shall inform User of all such terms and conditions. In the event such person is a "freelancer" or other third party independent of User and CCC, such party shall be deemed jointly a "User" for purposes of these terms and conditions. In any event, User shall be deemed to have accepted and agreed to all such terms and conditions if User republishes the Work in any fashion.

3. Scope of License; Limitations and Obligations.

    3.1. All Works and all rights therein, including copyright rights, remain the sole and exclusive property of the Rightsholder. The license created by the exchange of an Order Confirmation (and/or any invoice) and payment by User of the full amount set forth on that document includes only those rights expressly set forth in the Order Confirmation and in these terms and conditions, and conveys no other rights in the Work(s) to User. All rights not expressly granted are hereby reserved.

    3.2. General Payment Terms: You may pay by credit card or through an account with us payable at the end of the month. If you and we agree that you may establish a standing account with CCC, then the following terms apply: Remit Payment to: Copyright Clearance Center, 29118 Network Place, Chicago, IL 60673-1291. Payments Due: Invoices are payable upon their delivery to you (or upon our notice to you that they are available to you for downloading). After 30 days, outstanding amounts will be subject to a service charge of 1-1/2% per month or, if less, the maximum rate allowed by applicable law. Unless otherwise specifically set forth in the Order Confirmation or in a separate written agreement signed by CCC, invoices are due and payable on "net 30" terms. While User may exercise the rights licensed immediately upon issuance of

the Order Confirmation, the license is automatically revoked and is null and void, as if it had never been issued, if complete payment for the license is not received on a timely basis either from User directly or through a payment agent, such as a credit card company.

3.3. Unless otherwise provided in the Order Confirmation, any grant of rights to User (i) is "one-time" (including the editions and product family specified in the license), (ii) is non-exclusive and non-transferable and (iii) is subject to any and all limitations and restrictions (such as, but not limited to, limitations on duration of use or circulation) included in the Order Confirmation or invoice and/or in these terms and conditions. Upon completion of the licensed use, User shall either secure a new permission for further use of the Work(s) or immediately cease any new use of the Work(s) and shall render inaccessible (such as by deleting or by removing or severing links or other locators) any further copies of the Work (except for copies printed on paper in accordance with this license and still in User's stock at the end of such period).

3.4. In the event that the material for which a republication license is sought includes third party materials (such as photographs, illustrations, graphs, inserts and similar materials) which are identified in such material as having been used by permission, User is responsible for identifying, and seeking separate licenses (under this Service or otherwise) for, any of such third party materials; without a separate license, such third party materials may not be used.

3.5. Use of proper copyright notice for a Work is required as a condition of any license granted under the Service. Unless otherwise provided in the Order Confirmation, a proper copyright notice will read substantially as follows: "Republished with permission of [Rightsholder's name], from [Work's title, author, volume, edition number and year of copyright]; permission conveyed through Copyright Clearance Center, Inc. " Such notice must be provided in a reasonably legible font size and must be placed either immediately adjacent to the Work as used (for example, as part of a by-line or footnote but not as a separate electronic link) or in the place where substantially all other credits or notices for the new work containing the republished Work are located. Failure to include the required notice results in loss to the Rightsholder and CCC, and the User shall be liable to pay liquidated damages for each such failure equal to twice the use fee specified in the Order Confirmation, in addition to the use fee itself and any other fees and charges specified.

3.6. User may only make alterations to the Work if and as expressly set forth in the Order Confirmation. No Work may be used in any way that is defamatory, violates the rights of third parties (including such third parties' rights of copyright, privacy, publicity, or other tangible or intangible property), or is otherwise illegal, sexually explicit or obscene. In addition, User may not conjoin a Work with any other material that may result in damage to the reputation of the Rightsholder. User agrees to inform CCC if it becomes aware of any infringement of any rights in a Work and to cooperate with any reasonable request of CCC or the Rightsholder in connection therewith.

4. Indemnity. User hereby indemnifies and agrees to defend the Rightsholder and CCC, and their respective employees and directors, against all claims, liability, damages, costs and expenses, including legal fees and expenses, arising out of any use of a Work beyond the scope of the rights granted herein, or any use of a Work which has been altered in any unauthorized way by User, including claims of defamation or infringement of rights of copyright, publicity, privacy or other tangible or intangible property.

5. Limitation of Liability. UNDER NO CIRCUMSTANCES WILL CCC OR THE RIGHTSHOLDER BE LIABLE FOR ANY DIRECT, INDIRECT, CONSEQUENTIAL OR INCIDENTAL DAMAGES (INCLUDING WITHOUT LIMITATION DAMAGES FOR LOSS OF BUSINESS PROFITS OR INFORMATION, OR FOR BUSINESS INTERRUPTION) ARISING OUT OF THE USE OR INABILITY TO USE A WORK, EVEN IF ONE OF THEM HAS BEEN ADVISED OF THE POSSIBILITY OF SUCH DAMAGES. In any event, the total liability of the Rightsholder and CCC (including their respective employees and directors) shall not exceed the total amount actually paid by User for this license. User assumes full liability for the actions and omissions of its principals, employees, agents, affiliates, successors and assigns.

6. Limited Warranties. THE WORK(S) AND RIGHT(S) ARE PROVIDED "AS IS". CCC HAS THE RIGHT TO GRANT TO USER THE RIGHTS GRANTED IN THE ORDER CONFIRMATION DOCUMENT. CCC AND THE RIGHTSHOLDER DISCLAIM ALL

OTHER WARRANTIES RELATING TO THE WORK(S) AND RIGHT(S), EITHER EXPRESS OR IMPLIED, INCLUDING WITHOUT LIMITATION IMPLIED WARRANTIES OF MERCHANTABILITY OR FITNESS FOR A PARTICULAR PURPOSE. ADDITIONAL RIGHTS MAY BE REQUIRED TO USE ILLUSTRATIONS, GRAPHS, PHOTOGRAPHS, ABSTRACTS, INSERTS OR OTHER PORTIONS OF THE WORK (AS OPPOSED TO THE ENTIRE WORK) IN A MANNER CONTEMPLATED BY USER; USER UNDERSTANDS AND AGREES THAT NEITHER CCC NOR THE RIGHTSHOLDER MAY HAVE SUCH ADDITIONAL RIGHTS TO GRANT.

7. Effect of Breach. Any failure by User to pay any amount when due, or any use by User of a Work beyond the scope of the license set forth in the Order Confirmation and/or these terms and conditions, shall be a material breach of the license created by the Order Confirmation and these terms and conditions. Any breach not cured within 30 days of written notice thereof shall result in immediate termination of such license without further notice. Any unauthorized (but licensable) use of a Work that is terminated immediately upon notice thereof may be liquidated by payment of the Rightsholder's ordinary license price therefor; any unauthorized (and unlicensable) use that is not terminated immediately for any reason (including, for example, because materials containing the Work cannot reasonably be recalled) will be subject to all remedies available at law or in equity, but in no event to a payment of less than three times the Rightsholder's ordinary license price for the most closely analogous licensable use plus Rightsholder's and/or CCC's costs and expenses incurred in collecting such payment.

8. Miscellaneous.

    8.1. User acknowledges that CCC may, from time to time, make changes or additions to the Service or to these terms and conditions, and CCC reserves the right to send notice to the User by electronic mail or otherwise for the purposes of notifying User of such changes or additions; provided that any such changes or additions shall not apply to permissions already secured and paid for.

    8.2. Use of User-related information collected through the Service is governed by CCC's privacy policy, available online here:https://marketplace.copyright.com/rs-ui-web/mp/privacy-policy

    8.3. The licensing transaction described in the Order Confirmation is personal to User. Therefore, User may not assign or transfer to any other person (whether a natural person or an organization of any kind) the license created by the Order Confirmation and these terms and conditions or any rights granted hereunder; provided, however, that User may assign such license in its entirety on written notice to CCC in the event of a transfer of all or substantially all of User's rights in the new material which includes the Work(s) licensed under this Service.

    8.4. No amendment or waiver of any terms is binding unless set forth in writing and signed by the parties. The Rightsholder and CCC hereby object to any terms contained in any writing prepared by the User or its principals, employees, agents or affiliates and purporting to govern or otherwise relate to the licensing transaction described in the Order Confirmation, which terms are in any way inconsistent with any terms set forth in the Order Confirmation and/or in these terms and conditions or CCC's standard operating procedures, whether such writing is prepared prior to, simultaneously with or subsequent to the Order Confirmation, and whether such writing appears on a copy of the Order Confirmation or in a separate instrument.

    8.5. The licensing transaction described in the Order Confirmation document shall be governed by and construed under the law of the State of New York, USA, without regard to the principles thereof of conflicts of law. Any case, controversy, suit, action, or proceeding arising out of, in connection with, or related to such licensing transaction shall be brought, at CCC's sole discretion, in any federal or state court located in the County of New York, State of New York, USA, or in any federal or state court whose geographical jurisdiction covers the location of the Rightsholder set forth in the Order Confirmation. The parties expressly submit to the personal jurisdiction and venue of each such federal or state court.If you have any comments or questions about the Service or Copyright Clearance Center, please contact us at 978-750-8400 or send an e-mail to support@copyright.com.

Chapter 2, Figures 2.2 -2.5

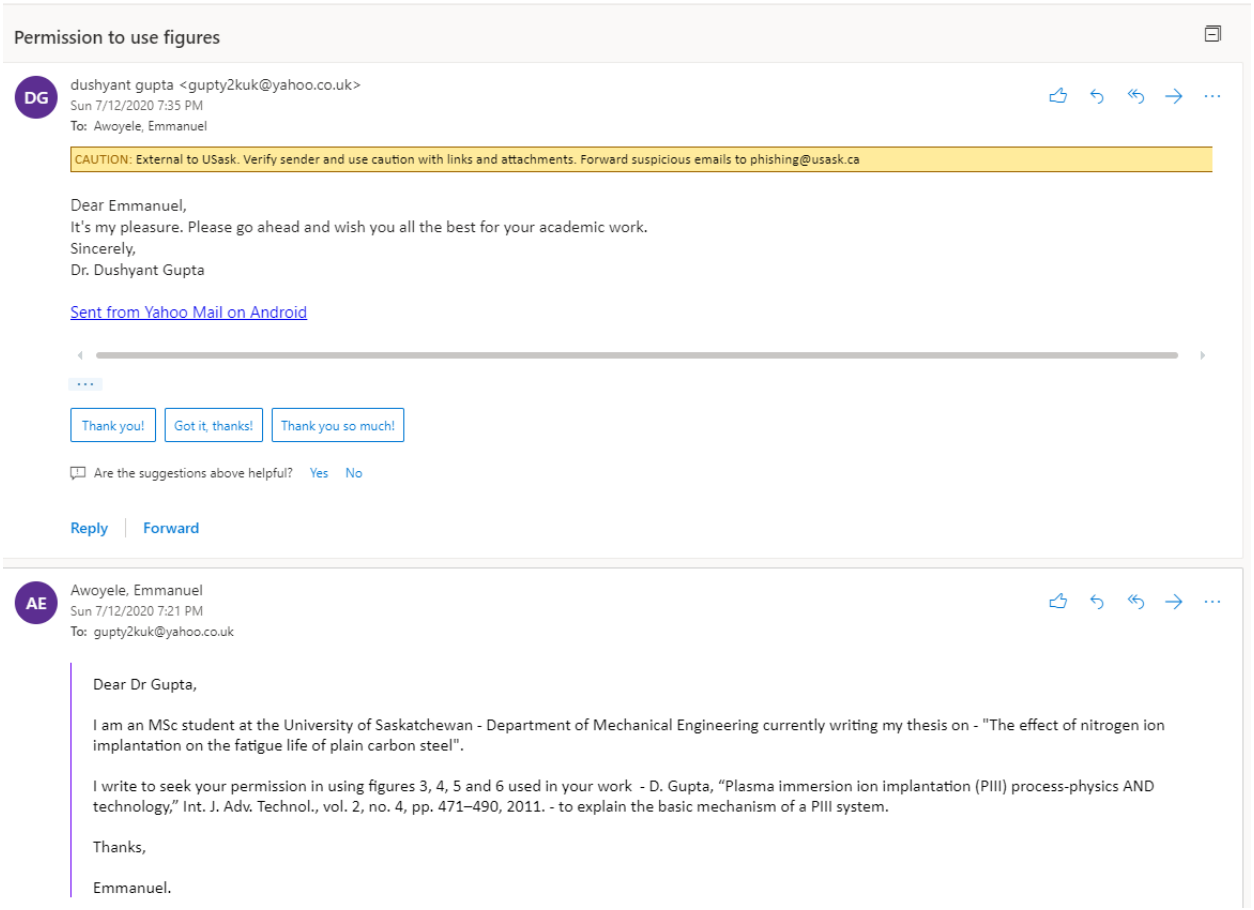

Permission to use figures

DG

dushyant gupta <gupty2kuk@yahoo.co.uk>
Sun 7/12/2020 7:35 PM
To: Awoyele, Emmanuel

CAUTION: External to USask. Verify sender and use caution with links and attachments. Forward suspicious emails to phishing@usask.ca

Dear Emmanuel,
It's my pleasure. Please go ahead and wish you all the best for your academic work.
Sincerely,
Dr. Dushyant Gupta

Sent from Yahoo Mail on Android

Thank you! | Got it, thanks! | Thank you so much!

Are the suggestions above helpful? Yes No

Reply | Forward

AE

Awoyele, Emmanuel
Sun 7/12/2020 7:21 PM
To: gupty2kuk@yahoo.co.uk

Dear Dr Gupta,

I am an MSc student at the University of Saskatchewan - Department of Mechanical Engineering currently writing my thesis on - "The effect of nitrogen ion implantation on the fatigue life of plain carbon steel".

I write to seek your permission in using figures 3, 4, 5 and 6 used in your work - D. Gupta, "Plasma immersion ion implantation (PIII) process-physics AND technology," Int. J. Adv. Technol., vol. 2, no. 4, pp. 471–490, 2011. - to explain the basic mechanism of a PIII system.

Thanks,

Emmanuel.

APPENDIX B

PIII TREATMENT PROCESS

Steps taken to start the PIII treatment process:

- Turn on water flow
- Open the Nitrogen bottle
- Open the mass flow valve
- Turn on Nitrogen gas on the relay board
- Set N_2 to 11% setpoint
- Set pressure to 15 mTorr
- Turn on the RF power switch
- Click on remote
- Turn on RF
- Set power to 100 w, 200 w and 250 w in steps – Adjust reflected power to less than 5%
- Turn on the pulse generator
- Turn on the transformer
- Set the output voltage to -5kV
- Check around to be sure everything is okay

steps were taken to end the PIII treatment process:

- Turn off the transformer
- Turn off the pulse generator
- Set RF to zero
- Switch off RF matching
- Set N_2 to zero
- Switch off N_2 on the relay board
- Turn off the turbo pump
- Close all valves
- After the turbo pump indicates it is safe to vent, open the vent valve

- Carefully open the chamber

The vacuum process followed these steps:

- Mount samples
- Close the chamber
- Check for alignment of the upper and lower chamber
- Turn on the air vent
- Shut off the fore-line block valve (Turn off its electrical relay)
- Make sure all other valves are closed
- Open the auxiliary valve
- Give about 20 minutes for pressure to drop to about 3mTorr
- Close fore-line valve
- Switch on the turbo pump control

Push the start button and wait for pressure to drop to high vacuum range.

APPENDIX C

SHEATH CALCULATIONS BASED ON CONRAD PATENT 4,764,394

[40]

NOTES: MKS units!			
epsilon0	8.85E-12	**F/m**	**permittivity of free space**
e	1.60E-19	C	
n_e	6.00E+09	cm^-3	NOTE SI convert!!!
Te	16.00	**eV**	
Phi_0	5.00E+03	**Volts**	VALUE OF APPLIED HIGH VOLTAGE PULSE
L_Debye	0.0384	**Cm**	
cyl. target r0	1.2700	**Cm**	
normalized r0	33.0886		
Conrad's X	0.2854	**ordinate (i.e. X-axis) for Conrad's graph FIG. 7**	
Conrad's f=f(X)	1.8000	**READ FROM CONRAD GRAPH FIG. C1**	
Conrad rs0	2.2860	**Cm**	**CONRAD'S INITIAL MATRIX SHEATH**
ion mass m_i	28.0000	**Amu**	
Cs = ion acoustic speed	0.7404	**cm/miscrosecond**	**NOTE UNITS!!**
D	4.5000	**Cm**	**MAX ALLOWABLE SHEATH SIZE**
tmax	2.9904	**microseconds**	
Fluence per pulse	8.8049E+10	**ions/cm^2**	
r_sheath	9.60E-01	**metre**	

			prf (Hz)	1000	
Voltage (kV)	**r_sheath (cm)**	**matrix fluence per pulse**	**number of pulses for 1e17 cm^-2**		**time (hours) for 1e17**
0	0.00	0.00E+00	--------	-----	
5	95.95	5.76E+11	173694	0.0	
10	135.70	8.14E+11	122820	0.0	
15	166.20	9.97E+11	100282	0.0	
20	191.91	1.15E+12	86847	0.0	
25	214.56	1.29E+12	77678	0.0	
30	235.04	1.41E+12	70910	0.0	
35	253.87	1.52E+12	65650	0.0	
40	271.40	1.63E+12	61410	0.0	
45	287.86	1.73E+12	57898	0.0	
50	303.43	1.82E+12	54927	0.0	

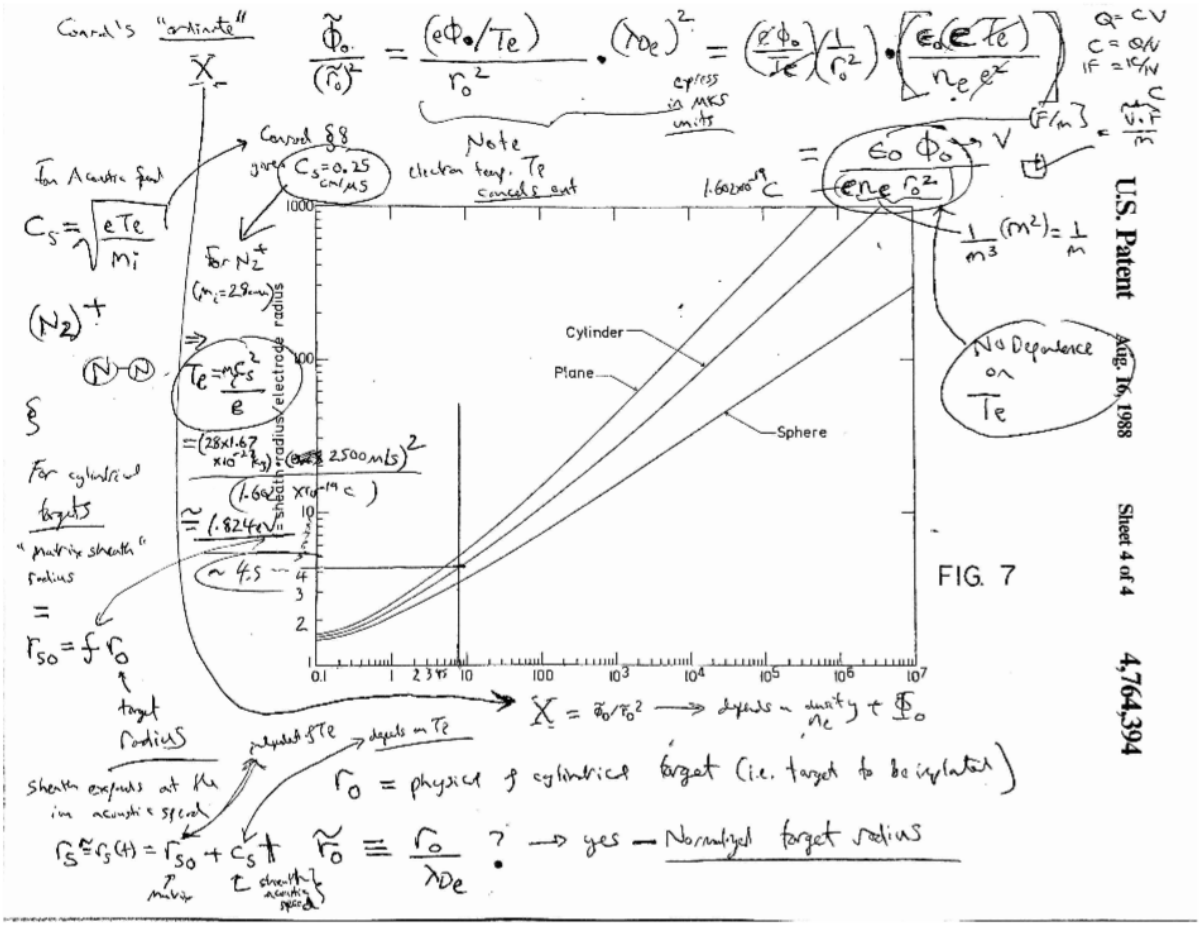

Figure C.1. Graph used to calculate the initial ion matrix sheath for plane, cylindrical and spherical electrodes [40].